Charles University in Prague
Faculty of Mathematics and Physics

Dynamic Stress Field of Kinematic Earthquake Source Models

Ph.D. Thesis

by Jan Burjánek

Prague, June 2007

Acknowledgements

First of all, I want to thank Prof. RNDr. Jiří Zahradník, DrSc., the supervisor of the thesis, for priceless advice and valuable comments that helped me solve many problems. I am indebted to Dr. František Gallovič for his slip velocity generators, to Prof. Michel Bouchon for the help with the DW method and to Dr. Luis Dalguer for many helpful discussions. I would like to thank also to Prof. Paul Spudich and Dr. Martin Mai for their constructive comments and helpful reviews on a paper submitted to *Geophys. J. Int.*, which comprises a substantial part of Chapter 3. Further, I would like to thank Prof. Kojiro Irikura for inviting me to D.P.R.I., where I got first in touch with earthquake source dynamics and exactly got the impulse to start this work. I am grateful to Káťa for her patience and support during my Ph.D. studies. Finally, I thank to colleagues from the department of geophysics for nice and stimulative atmosphere at the workplace and especially to Doc. RNDr. Ctirad Matyska, DrSc., the head of the department, for his support.

The research was financially supported by Czech Republic Grant Agency (GAČR) grants 205/03/1047, 205/07/0502, the Charles University grants (GAUK) 279/2006/B-GEO/MFF,235/2003/B-GEO/MFF, the research project of the Czech Ministry of Education MSM 0021620800, the EU projects EVG1-CT-1999-00001 PRESAP, 3HAZ-CORINTH - GOCE-4043, and the Marie Curie training network SPICE in the 6th Framework Program of the European Commission (MRTN- CT-2003-504267).

Missprints corrected 6.9.2007.

Contents

Chapter 1

Introduction

An important practical goal of present seismology is to reduce loses due to earthquakes by estimating the probable ground motions for future earthquakes at given site. A natural way of the solution is to extrapolate the information on past earthquakes. One approach is based on straight extrapolation of ground motions due to previous earthquakes. However, such approach is not reliable at present time because recurrence times of strong earthquakes are very long - up to several thousands of years and first quantitative ground motion observations are scarcely one hundred years old. Moreover, seismic observations are not (even nowadays) dense enough to make a coherent picture of damaging ground motions for a area of even several square kilometers close to the causative fault. Another approach is based on 'deciphering' observed ground motion due to earthquakes employing both the physical theories and mathematical models which could fill the gaps in recent observations. The latter approach is very promising and under rapid development. This thesis belongs to the latter class and is focused on the modelling of an earthquake source. In the following paragraphs we describe the state of art briefly, and outline the objectives and goals of the thesis.

It has been recognized soon that the observed Earth surface shaking contain the information on both seismic wave propagation through the Earth's interior and the source of these waves - earthquake source. However, as it is pointed in the book by Kostrov & Das (1988), it was paid much less attention to the earthquake source than to seismic wave propagation effects. The main reason was simple - at first, one has to know the seis-

mic waves response of Earth's structure to make the conclusions about earthquake source which is usually buried several kilometers under the ground. Another and may be a less apparent reason is that studies concerning seismic wave propagation are based on theory of elasticity which was formed already in the nineteenth century. For example, Kostrov & Das (1988) mention in this context Wiechert-Herglotz formula, a quite sophisticated tool for the retrieval of seismic wave velocity depth dependence, obtained already in 1907. On the other hand, there was at the very beginning of the twentieth a lack of the physical theories which would be capable to even describe the phenomena of an earthquake source. The idea that the cause of an earthquake is a failure of Earth's material along the fault due to accumulated elastic strain was formulated in the famous work of Reid (1910) on 1906 San Francisco earthquake, but it was rather just a qualitative description.

The useful mathematical framework for the description of displacement jumps in elastic solids was introduced in the works of Volterra (1907) and Somigliana (1914, 1915). The physical concept of the fracture mechanics of solids was founded as late as by Griffith (1921). However, these mathematical-physical concepts waited nearly another forty years for their geophysical application. Steketee (1958) was one of the first who recognized the possibility of application of the Volterra-Somigliana dislocations in geophysics. The *dislocation model* was afterwards accepted by seismological community as an useful earthquake source model, because it was generally consistent with the point source double-couple model (Vvedenskaya, 1956) satisfying the properties of observed polarities of the first seismic waves arrivals. The dislocation model represents a definition of space-time slip (tangential displacement jump) distribution along the fault. This slip distribution is not constrained by the dislocation model itself, in other words, for example, it does not have to reflect the properties of the material surrounding the fault, slip could appear on the fault instantaneously etc. It is clear that this is not the case of the earthquake source - the true slip distribution always reflects somehow the stress state along the fault. Nevertheless, the dislocation model has been widely applied in the seismology to both the forward and inverse problems. Let us mention for example line source model of Haskell (1964), which explains some features of the far-field seismograms successfully, although it is very crude

approximation, which leads to the infinite average static stress change over the fault.

The fracture mechanics concept (*crack model*) of Griffith (1921) was quite different. Griffith studied the energy balance on the fracture edge and introduced the formal criterion for the fracture extension. Such approach was very general but not practical. To model the displacement jump along the fault, one had to assume physical law governing the fracturing, initial stress and elastodynamic response of the medium surrounding the fault. Despite the fact that neither initial stress nor governing constitutive relations were known for the faults, a formal solution represented also a tough mathematical problem itself with very few known analytical solutions. Nonetheless, fracture mechanics represents a solid framework for the earthquake source physics.

The dislocation and crack models are not far from each other. A crack model results exactly in a specific dislocation model. It was already pointed by Steketee (1958) that the Griffith crack could be also considered as a type of the Somigliana dislocation. This is analogous to the two descriptions of the motion of a material point. If we know the trajectory of the point, we speak about material-point kinematics. On the other hand, if we know the force acting on this point, the laws governing its motion (e.g., Newton laws) and the trajectory is to be determined, we speak about the material-point dynamics. Hence, the term *kinematic fault model* is usually used for the dislocation model and the term *dynamic*[1] *fault model* for the crack model.

Since they were introduced to seismology, both the kinematic and dynamic earthquake source models have developed considerably (reviews by, e.g., Kostrov & Das, 1988; Madariaga & Olsen, 2002; Das, 2003). However, only kinematic models found the direct use in interpreting seismic data for a long time, because dynamic models were based mainly on the sophisticated numerical solutions. Analytic dynamic source models are known only for the fractures which are semi-infinite (e.g., Kostrov, 1966), expand self-similarly forever (e.g., Kostrov, 1964; Burridge & Willis, 1969; Nielsen & Madariaga, 2003) or for steady

[1]It is worthy to note that the term 'dynamic' has also another meaning: 'dynamic' as the opposite of 'static'. Hereafter we will use the terms 'dynamic model' as the opposite of 'kinematic model', 'earthquake dynamics' as the opposite of 'earthquake kinematics' and on the contrary in the rest of cases we will use 'dynamic' as the opposite of 'static', e.g., 'dynamic stress change' as the opposite of 'static stress change'.

state fracture pulses (Broberg, 1978; Freund, 1979; Rice *et al.*, 2005), and these are hardly applicable for real cases.

Kinematic models were applied for both forward and inverse problems. The forward kinematic problem concern calculation of ground motion due to prescribed space-time slip distribution along the fault, these find mainly use in strong ground motion simulation studies or in modelling of other earthquake induced phenomena (tsunami, landslides, etc.). Various slip distribution have been proposed from simple uniform slip models Haskell (1964) to stochastic k-squared models (Andrews, 1980; Herrero & Bernard, 1994; Mai & Beroza, 2002; Gallovič & Brokešová, 2007). The inverse kinematic problem, usually called kinematic source inversion or slip inversion, is formulated as a retrieval of space-time slip distribution along the fault (Spudich, 1980), fitting the observed records of both the static (GPS, InSAR) and dynamic displacements (seismograph records) on the Earth surface. The well-recorded 1979 Imperial Valley, California, earthquake was an impulse for developing kinematic source inversions (Olson & Apsel, 1982; Hartzell & Heaton, 1983). Since that time kinematic source inversion have been performed for a significant set of earthquakes and a number of the empirical scaling relations for kinematic source parameters have appeared (Somerville *et al.*, 1999; Mai & Beroza, 2002).

As a computer power increased a couple of dynamic models of recent earthquakes were also developed in 90' (e.g., Quin (1990) for the M6.5 1979 Imperial Valley earthquake and Olsen *et al.* (1997) for the M7.2 1992 Landers earthquake). These models were constructed by trial-error method from the results of kinematic source inversions. Until the work of Quin (1990), the kinematic and dynamic source models were treated more or less separately[2]. Quin recognized, that some features of the kinematic source model of real earthquake could be utilized for the boundary conditions in the forward dynamic modelling. The work of Quin was followed by group of Japanese scientists who extended Quin's trial and error approach with several iterative schemes (Mikumo, 1994; and references therein). The common point of these first dynamic inversions was that they all utilized forward

[2]The one of the exceptions was the paper by Madariaga (1978), who studied the dynamic (transient) stress field due kinematic Haskell's source model.

dynamic source modelling for the retrieval of frictional parameters along the fault for a priori given friction law.

Remark: Let us make a note on the term 'friction', which will be used frequently further in the text. It has been recognized that the most earthquakes occur on pre-existing faults and thus these earthquakes are rather stick-slip phenomenon than the fracturing of the rock. However, the process of transition from the 'stick phase' to 'slip phase' and the slippage itself can be described in the framework of the fracture mechanics. That is why the term 'friction law' is often mentioned instead of 'law governing the fracture'. The sides of the fault are pressed together at least by the hydrostatic pressure and thus the fault faces 'separated' during the fracture process still interact via friction during the slippage. This remains true even in the case of tensile fractures, because the fracture contact is usually filled with some material, e.g., fluids. The terms 'fault constitutive relation' or 'fault rheology' are more general as they should also describe the 'stick phase', e.g, healing of the fault. In this thesis we use terms 'fault rheology', 'fault constitutive relation', 'law governing the fracture', and 'friction law' as synonyms.

An alternative approach of the dynamic source model parameters inversion from the kinematic source model was presented by Chen & Aki (1996). They assumed neither any friction law nor forward dynamic modelling, they just solved the elastodynamic equation for the stress perturbation due to the space-time slip distribution of the kinematic model. Let us clarify the latter approach writing down the basic equations, and show the difference from the forward dynamic model. Consider the equation of motion:

$$\rho \frac{\partial^2 u_n}{\partial t^2} = \rho f_n + \frac{\partial \sigma_{mn}}{\partial x_m}, \tag{1.1}$$

where $\sigma_{mn}(\boldsymbol{x}, t)$ is the stress tensor, $u_n(\boldsymbol{x}, t)$ is the displacement vector, $f_n(\boldsymbol{x}, t)$ is the body force per unit mass vector, $\rho(\boldsymbol{x})$ is the density, x_m and t are the space-time coordinates respectively. Consider also Hooke's law in the following form:

$$\sigma_{mn} = \sigma^0_{mn} + c_{mnpq} \frac{\partial u_p}{\partial x_q}, \tag{1.2}$$

where $\sigma^0_{mn}(\boldsymbol{x})$ is the initial stress tensor and $c_{mnpq}(\boldsymbol{x})$ is the elastic stiffness tensor. So that we do not assume stress-free state as a reference state, but the prestressed state as

an initial state. We made an assumption of the small initial stress components compared with elastic moduli for validity of equation (1.2). We assume that the medium is in the equilibrium at the initial state:

$$\frac{\partial \sigma^0_{mn}}{\partial x_m} + \rho f^G_n = 0, \tag{1.3}$$

and that the gravitation force $f^G_n(\boldsymbol{x})$ the only body force at the initial state does not change with the time due to the rupture, i.e. the initial stress σ^0_{mn} also does not depend on time within the time frame of the rupture process. Introducing a notation for the incremental stress (or stress perturbation)

$$\tau_{mn} = \sigma_{mn} - \sigma^0_{mn} = c_{mnpq}\frac{\partial u_p}{\partial x_q}, \tag{1.4}$$

equation (1.1) can be rewritten using (1.3) as

$$\rho\frac{\partial^2 u_n}{\partial t^2} = \frac{\partial \tau_{mn}}{\partial x_m}. \tag{1.5}$$

assuming that there are no other body forces then gravitational (i.e., $f_n = f^G_n$). Now let us discuss boundary conditions along the fault surface. By the fault we mean two adjacent internal surfaces Σ^- and Σ^+. These two surfaces - the fault faces - can be understood as sides of a single fault surface Σ characterized by its normal vector $\boldsymbol{\nu}$. The other boundary and initial conditions are not of the interest now (let us assume an unbounded medium with the smoothly varying properties and zero initial conditions for both the displacement and velocity). Further, let us distinguish the kinematic and dynamic model which differ by their fault boundary conditions. For the kinematic model we prescribe boundary conditions

$$\begin{aligned} &\tau^+_{mn}\nu_m - \tau^-_{mn}\nu_m = 0 \\ &u^+_n - u^-_n = \Delta u_n\left(\boldsymbol{\xi}, t\right), \end{aligned} \tag{1.6}$$

along the fractured fault surface $\Sigma^*(t)$, which is changing with time (as rupture grows over the entire fault Σ), where u^+ (u^-) are displacements on the positive (negative) side of the fault, $\Delta u_n\left(\boldsymbol{\xi}, t\right)$ is the displacement jump (dislocation), τ^+_{mn} (τ^-_{mn}) are the stress perturbations on the positive (negative) side of the fault and $\boldsymbol{\xi}$ denotes the position along

the fractured fault $\Sigma^*(t)$. Hence, one could obtain both the displacement and stress in the whole volume by solving the system of equations (1.4),(1.5) with the boundary condition (1.6). It is clear that the problem is linear.

For the dynamic model we prescribe boundary conditions

$$\begin{aligned} &\tau^+_{mn}\nu_m - \tau^-_{mn}\nu_m = 0 \\ &\tau_{mn}\nu_m = -\sigma^0_{mn}\nu_m + \Upsilon_n\left(\sigma^\nu, \Delta\boldsymbol{u}, \Delta\dot{\boldsymbol{u}}, \theta, \ldots, \boldsymbol{\xi}\right), \end{aligned} \tag{1.7}$$

along the fractured fault surface $\Sigma^*(t)$, which is changing with time (as rupture grows over the entire fault Σ) where the function Υ_n represents the law controlling the fracture. In the earthquake dynamics the term *friction law* (or *fault constitutive relation*) is usually used. Υ_n generally depends on a large number of parameters (see Bizzarri & Cocco, 2005; for general discussion), we show just the most important ones - the normal stress along the fault ($\sigma^\nu = \sigma_{mn}\nu_m\nu_n$), the displacement jump $\Delta\boldsymbol{u}$, the displacement jump rate $\Delta\dot{\boldsymbol{u}}$, the fault state variable θ and the position along the fractured fault $\boldsymbol{\xi}$. A lot of authors present a much broader set of dependencies, however, it is known very little about the true fault friction laws, so in practice, the huge set of the proposed dependencies shrinks usually to these mentioned above. Hence, one could obtain both the displacement (including the displacement jump along the fault) and stress in the whole volume by solving the system of equations (1.4), (1.5) with the boundary condition (1.7) along $\Sigma^*(t)$. The time dependence of $\Sigma^*(t)$, i.e., the rupture propagation, is part of the solution which is determined by some fracture criterion (e.g, Griffith criterion, Kostrov & Das, 1988). It has to be determined simultaneously with the solution of the both equations (1.4) and (1.5), thus the problem is non-linear and hard to solve. The term 'spontaneous rupture' is usually used in the connection with these dynamic models. Sometimes, instead of spontaneous, the rupture front propagation is assumed a priori to make the problem easier (e.g., Madariaga, 1976).

The clear difference between the two approaches (kinematic vs. dynamic model) can be recognized from the boundary condition (1.7) which depends on the solution of (1.4), (1.5) itself (e.g., the displacement jump is present in the argument of friction law in (1.7)). Another, less apparent, but a serious difference is the time dependence of $\Sigma^*(t)$. In the

kinematic model, the time dependence of the fractured area is immaterial, as we can prescribe some ultimate fault area (e.g., $\Sigma^*(t) \to \infty$) and control the rupture directly by the prescription of the displacement jump (zero displacement jump is prescribed at the unfractured part of the fault).

Now let us assume some specific kinematic source model of an earthquake, i.e., some specific $\Delta\boldsymbol{u}'(\boldsymbol{\xi}, t)$. The boundary conditions (1.6), prescribed for the kinematic model, postulate the traction continuity across the fault, but neither the magnitude nor the direction of the traction are constrained a priori at all. However, one can obtain the stress perturbation[3] $\tau_{mn}^{(\Delta u')}(\boldsymbol{\xi}, t)$ along the fault due to the slip distribution $\Delta\boldsymbol{u}'(\boldsymbol{\xi}, t)$ by solving the system of equations (1.4), (1.5) with the boundary condition (1.6). Now the question arises: 'What can the stress perturbation $\tau_{mn}^{(\Delta u')}$ tell us about the possible friction on the fault?' To provide an answer, let us check the fault boundary conditions for the dynamic model. The relation between the stress perturbation and friction can be read from the equation (1.7):

$$\tilde{\Upsilon}_n\left(\sigma^{\nu\prime}, \Delta\boldsymbol{u}', \Delta\dot{\boldsymbol{u}}', \theta', \ldots, \boldsymbol{\xi}\right) = \tau_{mn}^{(\Delta u')}\tilde{\nu}_m + \sigma_{mn}^{0\prime}\tilde{\nu_m}, \tag{1.8}$$

where $\tilde{\Upsilon}$ is the unknown friction law. The dash symbol denotes the properties connected with the particular earthquake, whereas the tilde symbol denotes the properties connected with the particular fault (friction law and fault geometry). Hence, e.g., initial stress $\sigma_{mn}^{0\prime}$ is the reference state just before the earthquake. Thus, if we know the initial stress $\sigma_{mn}^{0\prime}(\boldsymbol{\xi})$, we can determine resulting friction at the fault for the earthquake. Generally, performing such procedure for several earthquakes acting on the same fault would lead to the estimation of the possible friction laws holding at that particular fault. It is useful to substitute for the time dependency in the stress perturbation $\tau_{mn}^{(\Delta u')}(\boldsymbol{\xi}, t)$ as the friction law do not usually depend explicitly on time, but rather on the other quantities suggested in the argument of the friction law $\tilde{\Upsilon}_n\left(\sigma^{\nu\prime}, \Delta\boldsymbol{u}', \Delta\dot{\boldsymbol{u}}', \theta', \ldots, \boldsymbol{\xi}\right)$. In other words, it is reasonable to study, e.g., $\tau_{mn}^{(\Delta u')}\left[\sigma^{\nu\prime}(\boldsymbol{\xi}, t), \Delta\boldsymbol{u}'(\boldsymbol{\xi}, t), \Delta\dot{\boldsymbol{u}}(\boldsymbol{\xi}, t), \boldsymbol{\xi}\right]$.

An estimation of the fault constitutive relations $\boldsymbol{\Upsilon}$ outlined above is much more straight-

[3] Let us just note that the term 'dynamic stress field' is used in the literature for the stress perturbation $\tau_{mn}^{(\Delta u')}(\boldsymbol{\xi}, t)$ to emphasize its time dependence, as the analysis of static stress fields are much common.

forward and easier to solve than the approach of Mikumo (1994), who employs forward dynamic modelling. Moreover, one does not have to assume a friction law a priori, as in the dynamic modelling. In practice, the estimation of the fault friction parameters strongly depends on the 'quality' of the utilized kinematic models, i.e., on the space-time resolution of the slip, accompanied with serious difficulties mentioned above. A very serious problem is also represented by the initial stress present in (1.8), which is generally heterogeneous but not known in the crust. The homogenous initial stress is usually assumed. Nevertheless such an assumption can clearly lead to biased friction estimations. However, the problem of the initial stress is common to the forward dynamic problem, too. A number of authors applied the methodology described above for the friction estimation along existing faults (Chen & Aki, 1996; Bouchon 1997; Ide & Takeo 1997; Day *et al.*, 1998; Dalguer *et al.*, 2002; and Tinti *et al.*, 2005b) for several kinematic source models of real earthquakes. Authors of these studies did not study quantitatively the effects of space-time filtering which is applied during the kinematic inversion, although it can affect the results considerably. Also uncertainties of the space-time slip distributions were not take into account. A partial step forward was done in the papers by Piatanesi *et al.* (2004) and Tinti *et al.* (2005a), where the authors study the influence of slip velocity function on the friction parameters estimation.

Nevertheless, opposed to studies based on slip inversions of real earthquakes, one can also investigate the stress implications of the theoretical slip distributions. There is a broad class of theoretical kinematic models, which are used mainly for the near fault ground motion modelling. The most widely applied has been the Haskell fault model (Haskell, 1964; Haskell, 1969) and more recently the k-squared source model (e.g., Andrews, 1981; Herrero & Bernard, 1994; Bernard *et al.*, 1996; Hisada, 2000; Gallovič & Brokešová, 2007). The dynamic stress field of the Haskell model was studied by Madariaga (1978), who found strong contradictions to earthquake source physics (see Chapter 2 in this thesis). The static stress field of k-squared model was analyzed by Andrews (1980), however, k-squared model has undergone some development since that time (e.g., k-squared models with asperities, Gallovič & Brokešová, 2004a). The dynamic stress field of k-squared models has not been

studied yet. Thus it has been nearly impossible to confront the k-squared model with the earthquake dynamics, e.g., it has not been assured yet whether the k-squared model is consistent with earthquake source physics.

Based on the previous analysis, the main goal of this thesis is formulated as to fill the existing gap between k-squared models recently developed for the strong ground motion predictions and recent findings in the dynamic source model studies. To this goal, we develop a method of dynamic stress calculations, apply the method to the k-squared model and perform the quantitative analysis of the resulting stress field. Such computation and analysis of the dynamic stress field due to k-squared model should clarify the physical basis of this model. Particularly, we want to understand if the k-squared model is consistent with some friction laws of the earthquake dynamics. Moreover, k-squared source model has a lot free parameters, which are to be tuned a priori. A parametric study concerning the dynamic stress field analysis can help in constraining some of these parameters, so it is included in this work, too. Thus the study can be useful for future strong ground motion simulations. The space-time filtering effects on the dynamic stress field can be also demonstrated for the case of k-squared model, as it includes short-wavelength and short-period variations which are smeared out in the results of kinematic inversions. Thus it is possible to discuss these effects quantitatively.

To perform the study outlined above, we have to adopt some method of dynamic stress field calculation. Particularly, the method which is capable of solving the system of equations (1.4), (1.5) with the boundary condition (1.6) including the solution at the boundary itself. We decided to adopt the boundary element method, calculating Green's functions by the discrete wavenumber method of Bouchon (1997). The method of calculation, numerical tests and some basic applications are presented in Chapter 2. The mathematical basis of the discrete wavenumber method is presented with complete derivation in the Appendix A. The dynamic stress field calculations and analysis of the k-squared model are presented in Chapter 3.

Chapter 2

Method of Calculation of Dynamic Stress

The objective of the thesis is the study of dynamic stress history on a fault induced by prescribed space-time slip distribution. In this chapter we formulate the mathematical problem exactly and describe the solution we follow. The test of the method against known analytic solution for a static circular crack is presented. The basic characteristics of dynamic stress field along the fault during an earthquake are illustrated on the Haskell fault model. An application for the dynamic stress field induced by simple circular crack is also presented to better understand the dynamic stress radiation pattern along the fault. Generally, we refer to Aki & Richards (1980) for basic definitions and theorems concerning the seismic source representation and continuum mechanics.

2.1 Formulation of the problem and solution

We assume an infinite body with the smoothly varying properties including two adjacent internal surfaces Σ^- and Σ^+ which represent the faces of a buried fault. Σ^- and Σ^+ can be understood as sides of a single fault surface Σ. Further, we assume a kinematic model which prescribes a displacement discontinuity along the fault surface - relative movement of the fault faces. The stress is continuous across the fault surface. The displacement discontinuity - dislocation can be viewed as a boundary condition for the system of equation

of motion and stress-strain relation. Hence, for a linear perfectly elastic solid we write

$$\rho \frac{\partial^2 u_n}{\partial t^2} = f_n + \frac{\partial \tau_{mn}}{\partial x_m} \tag{2.1}$$

$$\tau_{mn} = c_{mnpq} \frac{\partial u_p}{\partial x_q}, \tag{2.2}$$

with the boundary conditions

$$\begin{aligned} \left[\tau_{mn}\left(\boldsymbol{\xi},\tau\right)\nu_m\left(\boldsymbol{\xi},\tau\right)\right]\big|_{\Sigma^+} - \left[\tau_{mn}\left(\boldsymbol{\xi},\tau\right)\nu_m\left(\boldsymbol{\xi},\tau\right)\right]\big|_{\Sigma^-} &= \mathbf{0} \\ u_k\left(\boldsymbol{\xi},\tau\right)\big|_{\Sigma^+} - u_k\left(\boldsymbol{\xi},\tau\right)\big|_{\Sigma^-} &= \Delta u_k\left(\boldsymbol{\xi},\tau\right), \quad \boldsymbol{\xi} \in \Sigma, \end{aligned} \tag{2.3}$$

where t denotes the time, $\boldsymbol{x}$ denotes the position within the volume, $u_n = u_n(\boldsymbol{x},t)$ are the displacement, $f_n = f_n(\boldsymbol{x},t)$ are the body force, $\tau_{mn} = \tau_{mn}(\boldsymbol{x},t)$ are the stress tensor, $c_{ijpq} = c_{ijpq}(\boldsymbol{x})$ are the elastic stiffness tensor components respectively, $\rho = \rho(\boldsymbol{x})$ is the density and $\Delta u_k\left(\boldsymbol{\xi},\tau\right)$ are the dislocation components at time τ and position $\boldsymbol{\xi}$ along the fault surface Σ characterized by its normal vector $\boldsymbol{\nu}$. One has to solve the system of partial differential equations (2.1-2.2) with the boundary condition (2.3) to get the both displacement and stress fields in the volume and also the stress field on the fault surface. Our goal is the determination of the dynamic stress field just at the fault surface due to the prescribed slip history.

A broad spectrum of both analytic and numerical methods is available for the solution of such problem. For example, Madariaga (1978) applied analytic Cagniard-De Hoop method for the dynamic stress evaluation due to the Haskell kinematic fault model in a homogeneous space. However, we want to evaluate stress fields for slip functions given numerically, hence we need a semi-analytical or fully numerical method. Let us assume a homogeneous unbounded isotropic medium for which the elastodynamic Green functions are known analytically. Hence a boundary element method (BEM) is applicable. A solution for a more general medium will be discussed briefly later. The boundary integrals, known also as representations theorems, are published for several elastodynamic problems (e.g., Aki & Richards, 1980; Kostrov & Das 1988). Aki & Richards (1980) gives for a

displacement

$$u_n(\boldsymbol{x},t) = \int_{-\infty}^{\infty}\int_{\Sigma} c_{ijpq}\nu_j(\boldsymbol{\xi})\,\Delta u_i(\boldsymbol{\xi},\tau)\,\frac{\partial}{\partial\xi_q}G_{np}(\boldsymbol{x}-\boldsymbol{\xi},\mathbf{0},t-\tau,0)\,d\Sigma\,dt \tag{2.4}$$

where $\nu_j(\boldsymbol{\xi})$ are the surface Σ normal components and $G_{np}(\boldsymbol{x},\boldsymbol{\xi},t,\tau)$ are the elastodynamic Green functions - the nth component of the displacement at position $\boldsymbol{x}$ and time t due to an impulse point force applied in the p-direction at position $\boldsymbol{\xi}$ and time τ. A solution for a stress can be simply obtained applying (2.2) on (2.4) and interchanging the order of the differentiations with respect to $\boldsymbol{x}$ and integrations, so that

$$\tau_{mn}(\boldsymbol{x},t) = \int_{-\infty}^{\infty}\int_{\Sigma} c_{ijpq}\nu_j(\boldsymbol{\xi})\,\Delta u_i(\boldsymbol{\xi},\tau)\,\frac{\partial}{\partial\xi_q}H_{mnp}(\boldsymbol{x}-\boldsymbol{\xi},\mathbf{0},t-\tau,0)\,d\Sigma\,dt \tag{2.5}$$

with

$$H_{mnp}(\boldsymbol{x},\boldsymbol{\xi},t,\tau) = c_{mnkl}\frac{\partial}{\partial x_l}G_{kp}(\boldsymbol{x},\boldsymbol{\xi},t,\tau)\,. \tag{2.6}$$

Problems arise solving boundary integral (2.5) due to the hypersingular terms present in the *stress Green functions* (2.6), so their direct discretization is difficult (see, e.g., discussion by Kostrov & Das, 1988). One possibility is the extraction and separate integration of the strong singularities (Bonnet & Bui, 1993; Fukuyama & Madariaga, 1998) or the spectral representation of the boundary integral (Geubelle & Rice, 1995; Bouchon, 1997).

Following the method presented by Bouchon (1997), we developed a parallelized code for dynamic stress change calculations along a planar fault in a homogeneous unbounded isotropic medium. The method is based on the discrete wavenumber expansion of the stress Green function. The discrete wavenumber (DW) method was introduced to elastodynamics by Bouchon & Aki (1977) and has been used extensively in seismology for a variety of problems, including tests of the accuracy of other numerical methods (for a review, see Bouchon, 2003). The popularity of the DW method is based on its great accuracy and simplicity. The fundamental of the DW method is based on the work of Lamb (1904), who recognized that the elastodynamic Green function can be expressed as a superposition of the harmonic plane waves, i.e., as a single and double Fourier integral for 2D and

3D problems respectively[1]. The idea of the discrete wavenumber method is the direct evaluation of these Fourier integrals by discrete Fourier series. Thus the space-time and spectral periodicities are introduced into the problem. The space-time periodicity can be quite tricky, because one deals with an infinite response of infinity of sources aliased to a single interval of interest. One has to pay also attention to the discretization of the space-time slip distribution in both space and time applying the sampling theorem, to prevent from the alias effect. This requires a sufficient smoothness of the space-time slip distribution. The complete derivation and description of the discrete wavenumber method for stress calculations in the homogeneous unbounded isotropic medium on a planar fault can be found in Appendix A.

Now, let us briefly discuss the case of inhomogeneous medium. The stress calculations by the DW method can be extended to layered medium, applying the propagator matrices. However the efficiency of such calculation is questionable. Note, that the most applications of the DW method have been carried out for the ground motion calculations in the layered medium with the DW formulation presented by Bouchon (1981) and the matrix method of Kennet & Kerry (1979). In this formulation, the Green function is expressed as a superposition of the harmonic cylindrical waves. Particularly, the Green function for 3D problem is expanded in 1D series of Bessel functions. It can be shown (e.g., Aki & Richards, 1980) that the reflection and transmition coefficients are the same for both the plane and cylindrical (with the axes of symmetry perpendicular to the interface) waves. Hence, the advantage of later DW formulation is clear - the evaluation of 1D series of Bessel functions is much more effective than evaluation of 2D Fourier series. However, this effective formulation cannot be used for our purposes, as it is singular just at the source (for $\boldsymbol{x} = \boldsymbol{\xi}$). For even more general medium it would be necessary to apply a finite difference or finite element method to solve the system of equations (2.1-2.2) with boundary condition (2.3), as it was done, e.g., by Ide & Takeo (1997) or Day et al. (1998). Note that the asymptotic methods (e.g., the ray method) cannot be applied for this kind of problem, as we seek the

[1]The term Weyl integral is sometimes used for such representation of fundamental wave equation solution.

solution of equation of motion just at and very close to the source and near field terms dominate in the solution.

2.2 Test and demonstration of the method

In the following section we demonstrate the DW method, which is thoroughly described in Appendix A, on the well known cases - static circular crack and Haskell fault model. We also present the dynamic stress field along fault due to simple circular crack, where the stress radiation pattern is demonstrated for the first time. In all cases a fault plane in a homogeneous unbounded isotropic medium is assumed.

2.2.1 Static circular crack

The accuracy of the static DW solution can be demonstrated on the well known static circular crack problem. Keilis-Borok (1959) found the analytic formula for the static slip distribution due to an uniform stress drop within a circle in homogeneous elastic space. We use his result as our input slip distribution and we will compare the resulting static stress change distributions with the analytic ones. Analytic formulas for the static stress change outside the crack are presented, e.g., in Andrews (1974). For circular crack of radius $R = 1$ and static stress drop $\Delta\sigma = 1$ placed in unbounded homogeneous isotropic space ($\mu = \lambda = \rho = 1$) we have following relations

$$\Delta \boldsymbol{u}\left(r,\varphi,0\right) = \begin{cases} \left(\frac{24}{7\pi}\sqrt{1-r^2},0,0\right) & r \le 1 \\ \mathbf{0} & r > 1 \end{cases} \tag{2.7}$$

$$\tau_{xz}\left(r,\varphi,0\right) = \begin{cases} -1 & r \le 1 \\ \frac{2}{\pi}\left(-\arctan\frac{1}{\sqrt{r^2-1}} + \frac{1}{\sqrt{r^2-1}} + \frac{1}{7}\frac{\cos 2\varphi}{r^2\sqrt{r^2-1}}\right) & r > 1 \end{cases} \tag{2.8}$$

$$\tau_{yz}\left(r,\varphi,0\right) = \begin{cases} 0 & r \le 1 \\ -\frac{2}{7\pi}\frac{\sin 2\varphi}{r^2\sqrt{r^2-1}} & r > 1 \end{cases} \tag{2.9}$$

$$\tau_{zz}\left(r,\varphi,0\right) = 0 \tag{2.10}$$

in cylindrical coordinates (r,φ,z) with the origin in the center of the crack and φ measured from the x-axes in the clockwise direction. A comparisons of the DW solutions against

a)

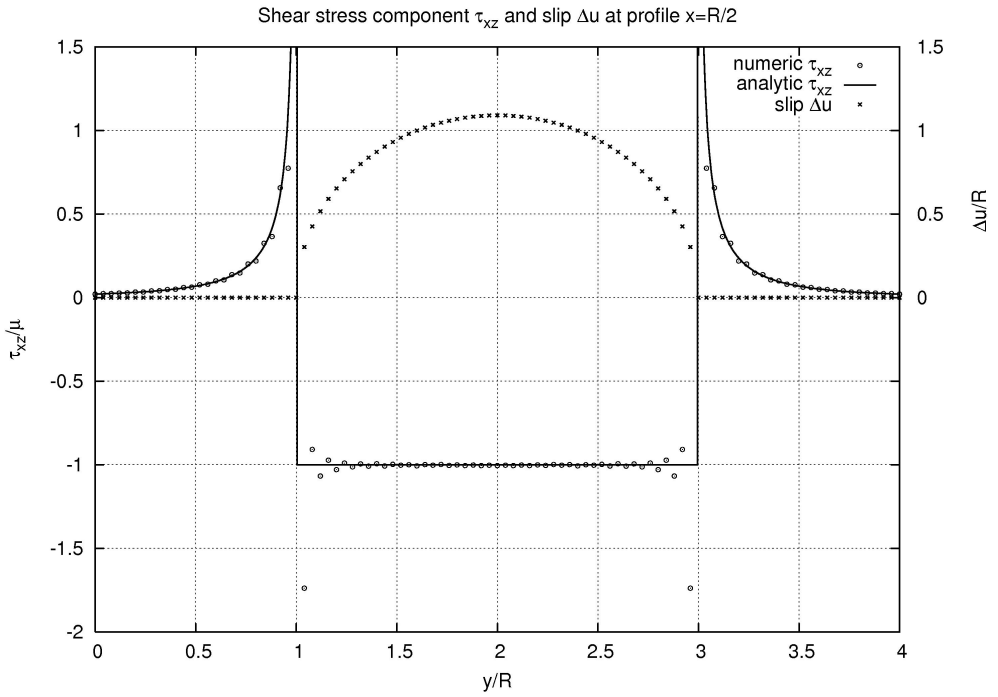

b)

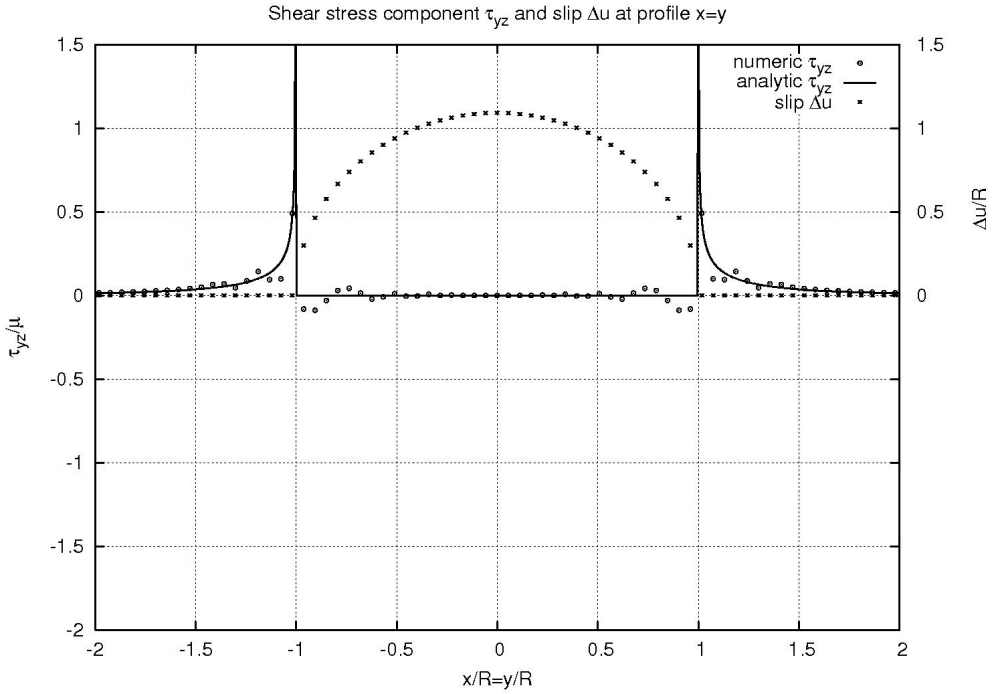

Figure 2.1: A comparison of the DW (circles with dots) and analytic (solid line) solutions for a static stress change due to the slip generated by equation (2.7): a) τ_{xz} for $x = 0$ cross section and b) τ_{yz} for $x = y$ cross section. The discretized slip distribution which enters DW calculation is plotted for the given cross sections by crosses.

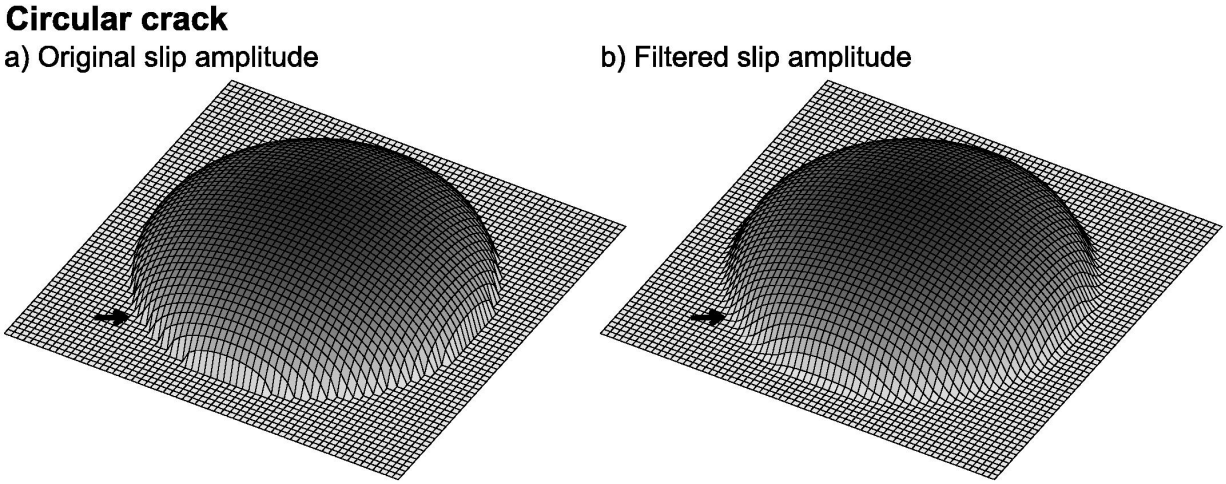

Figure 2.2: a) original and b) filtered slip amplitude in x-direction for the discretization used. The arrow marks the region most affected by the filtration.

the analytical ones are shown in Fig. 2.1. The τ_{xz} component for $x = 0$ cross section is shown in Fig. 2.1a and τ_{yz} for $x = y$ cross section is shown in Fig. 2.1b. The discrete representation of the slip distribution which enters DW calculation is also plotted in these figures. Note the sharp termination of the slip at the border of the crack. It causes a stress discontinuity at the crack border and consequently the oscillation in the DW solution. It is well-known Gibbs' phenomenon which comes from the truncation of the Fourier series of discontinuous functions. Increasing the number of terms in the Fourier series just shifts the oscillation closer to the discontinuity, but does not affect its amplitude. Thus, it results in heavy calculations with just modest improvement. A more effective way of the regularization is straightforward, although not enough discussed in literature. We remove the high wavenumber contribution from DW solution with a smooth low-pass filter. This is equivalent to the application of the low-pass filter on the input slip model, as the equation (2.5) can be written also in form of spatial convolution (equation A.82 from Appendix A, after extending the integration over the fault to the whole plane $z = 0$). Particularly, we applied the double cosine window

$$\frac{1}{4}\left[\cos\left(\frac{k_x}{k_x^{max}}\pi\right)+1\right]\left[\cos\left(\frac{k_y}{k_y^{max}}\pi\right)+1\right]. \tag{2.11}$$

a)

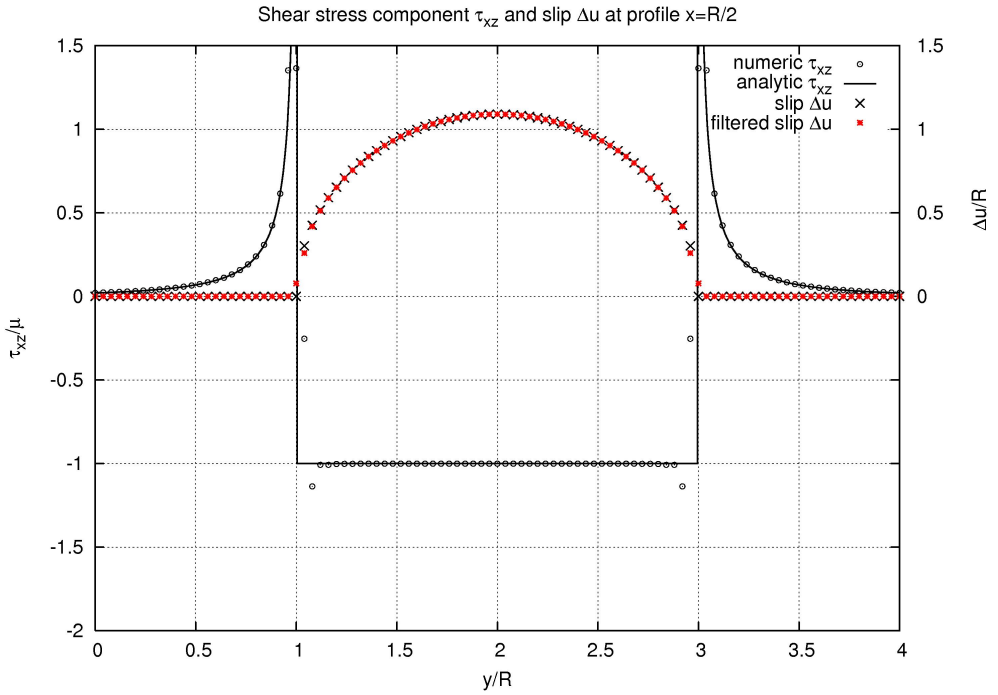

b)

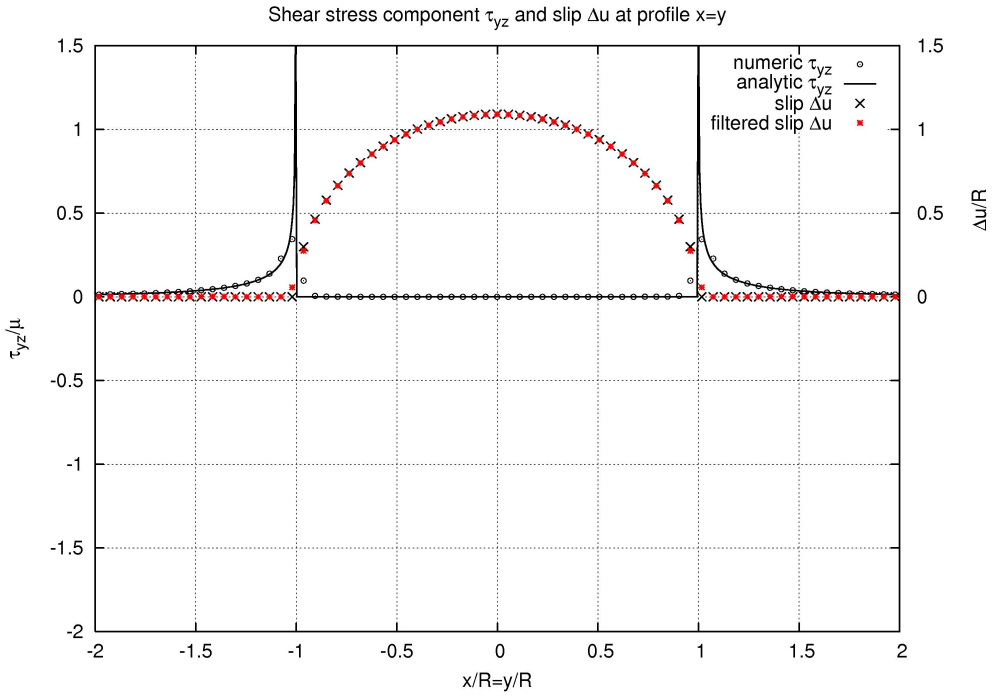

Figure 2.3: A comparison of the DW (circles with dots) solution for a static stress change due to the filtered slip distribution shown in Fig. 2.2a and analytic solution (solid line) for the original unfiltered slip distribution shown in Fig. 2.2b: a) τ_{xz} for $x = 0$ cross section and b) τ_{yz} for $x = y$ cross section. The filtered slip distribution which enters DW calculation is plotted for the given cross sections by red symbols. The original slip distribution is plotted for the given cross sections by black crosses.

The results of low-pass filtering of the slip distribution are shown in Fig. 2.2. One can see that high wavenumber contribution come just from the borders of the crack. Resulting stress change τ_{xz} for $x = 0$ cross section is shown in Fig. 2.3a and τ_{yz} for $x = y$ cross section is shown in Fig. 2.3b. The utilization of the low-pass filter improved the match with the analytical solution considerably. The oscillations were damped and the amplitude of the Gibbs' overshoot was also reduced. On the other hand, the filter did not affect the slip distribution much (in fact it affected just a few points in the proximity of the crack's circumference, see red symbols in both Fig. 2.3a and Fig. 2.3b). We remark, that none of numerical methods can fit the singular solution and one has to be very cautious of them. In the discrete wavenumber method, one easily prevent singularities to distort the solution by using the filter like (2.11), which is very easy to apply in this method.

2.2.2 Haskell fault model

A rectangular dislocation, usually called Haskell model, is the kinematic earthquake source model introduced by Ben-Menahem (1961) and studied in detail by Haskell (1964, 1969). It can be described by the relation for slip amplitude

$$|\Delta \boldsymbol{u}\left(\boldsymbol{\xi},\tau\right)| = \begin{cases} 0 & \tau < \frac{\xi_1}{v_r} \\ D\frac{\tau - \frac{\xi_1}{v_r}}{\tau_n} & \frac{\xi_1}{v_r} \leq \tau \leq \frac{\xi_1}{v_r} + \tau_n \\ D & \frac{\xi_1}{v_r} + \tau_n < \tau \end{cases} \tag{2.12}$$

with $\xi_1 \in \langle 0, L\rangle$ and $\xi_2 \in \langle 0, W\rangle$, where v_r is the rupture velocity, τ_n is the rise time, D is the static slip value and W, L are the width and length of the fault respectively. The direction of the slip is arbitrary, but constant over the fault. Several restriction to (2.12) are sometimes assumed, e.g. the instantaneous slip ($t_n \to 0$) approximation, or line source ($W \to 0$) approximation. Such models are usually used to demonstrate the influence of finite source on the far-field radiation (directivity, apparent source time function duration). Madariaga (1978) applied the Cagniard-De Hoop method for the evaluation of the both near-field displacement and stress field of the Haskell model with the instantaneous slip. He found strong contradictions with earthquake source physics. The most severe one was,

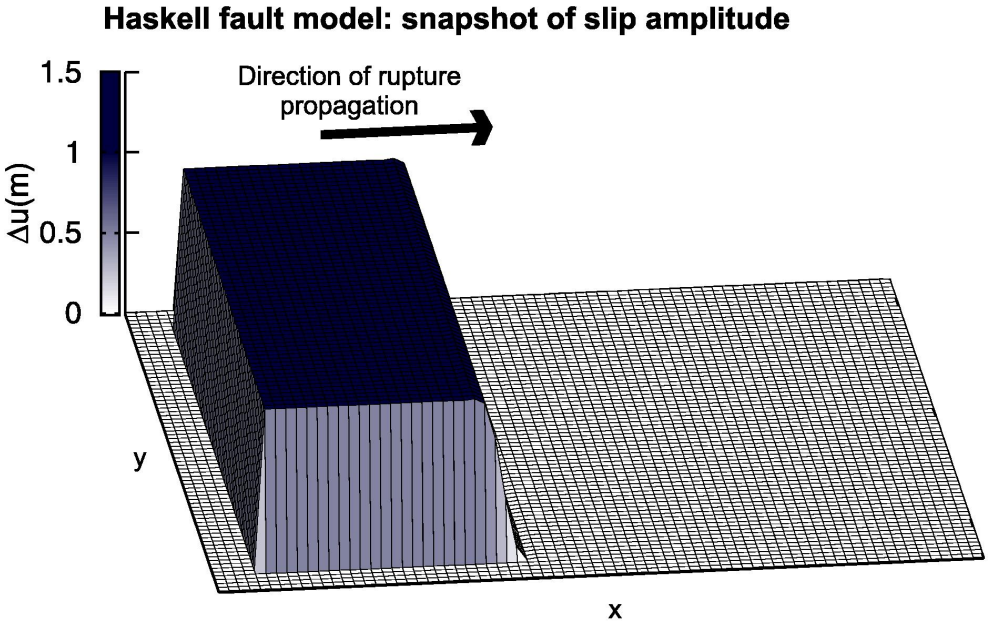

Figure 2.4: Haskell fault modell.

that the average static stress drop[2] was infinite due to strong singularities at the edges of the dislocation. Bouchon (1997) compared his results obtained by his DW method for the Haskell model with Madariaga's (1978) solution and made a conclusion that the DW method was robust solving such singular model, i.e., singularities did not distort qualitatively the solution. Additionally, we remak that both spatial and time singularities are expanded into finite Fourier series in the discrete wavenumber method and thus these singularities are represented accurately up to a certain wavenumber and frequency. In other words, such Fourier series expansions represent a 'natural' way of the regularization.

We also present the dynamic stress field of the Haskell fault model, as basic features of the transient stress can be simply described for this model. We set $v_P = 6$ km/s, $v_S = 3.46$ km/s, $\rho = 2800$ kg/m^3, $L = 10.0625$ km, $W = 5.0625$ km, $D = 1$ m, $v_r = 0.9\, v_S = 3.11$ km/s. The calculations were carried out with the following DW configuration (for details, we refer to sections A.3-A.5 of Appendix A): spatial periods $L_x = L_y = 100.0625$ km, time period $T = 16$ s, spatial steps $\Delta x = \Delta y = 62.5$ m, time step $\Delta t =$

[2]Average static stress change over the total area of the dislocation.

0.03125 s, artificial attenuation $\omega^I = \pi/T$. We assume an instantaneous slip, to get result comparable with that of Madariaga (1978). As we use discrete Fourier series for slip time function representation, we encounter Gibbs' phenomenon in time domain. Thus we remove high-frequency contribution from the slip function applying the cosine window (see later relation (2.13)) with $f_{max} = 10$ Hz, making the rise time non-zero effectively. A snapshot of the slip at some time $0 < \tau_0 < L/v_r$ is shown in Fig. 2.4 (ξ_1 and ξ_2 are parallel to x and y respectively). The rupture starts from the line ($\xi_1 = 0$) of the length W. The direction of slip is chosen either parallel or perpendicular to the rupture front. The case of the rupture front parallel slip mirrors an *inplane mode* fracture, while the case of the rupture front perpendicular slip mirrors an *antiplane mode* fracture.

A time history of the slip-parallel component of the shear stress at a point on the fault for the 'inplane' mode is plotted in Fig. 2.5. One can recognize wave group associated with the rupture onset - starting phase and wave group associated with the rupture termination - stopping phase. Neither Madariaga (1978), nor Bouchon (1997) showed or mentioned the stopping phase in their results, as they stopped their calculation too early. Starting phase consists of P-wave onset, S-wave onset and the rupture arrival. S-waves present square root singularity pointing to negative stress. Note the negative stress values between S-wave and rupture front arrivals. This correspond to the range of formal 'velocities' close to v_S, which resemble 'prohibited' band for rupture velocity of in-plane cracks[3]. The Rayleigh velocity is approximately 0.92 v_S for homogeneous medium. After passage of the rupture front, stress become close to the static solution (approximately the times from 2 s to 4 s). The stopping phase consists of P-wave and S-wave arrivals coming from the terminating edge ($\xi_1 = L$) of the fault. These onsets have reversal polarity with respect to starting phase.

A time history of the slip-parallel component of the shear stress at a point on the fault for the 'antiplane' mode is plotted in Fig. 2.6. One can recognize again starting phase and also very weak stopping phase. The P-wave onset is very weak, what is understandable, as P-waves are not present in the pure *antiplane mode* at all. Hence, generally, 'antiplane'

[3]For example, Andrews (1976b) showed for 2D in-plane crack model and the slip weakening friction that rupture does not propagate with rupture velocities between Rayleigh and S-wave velocities.

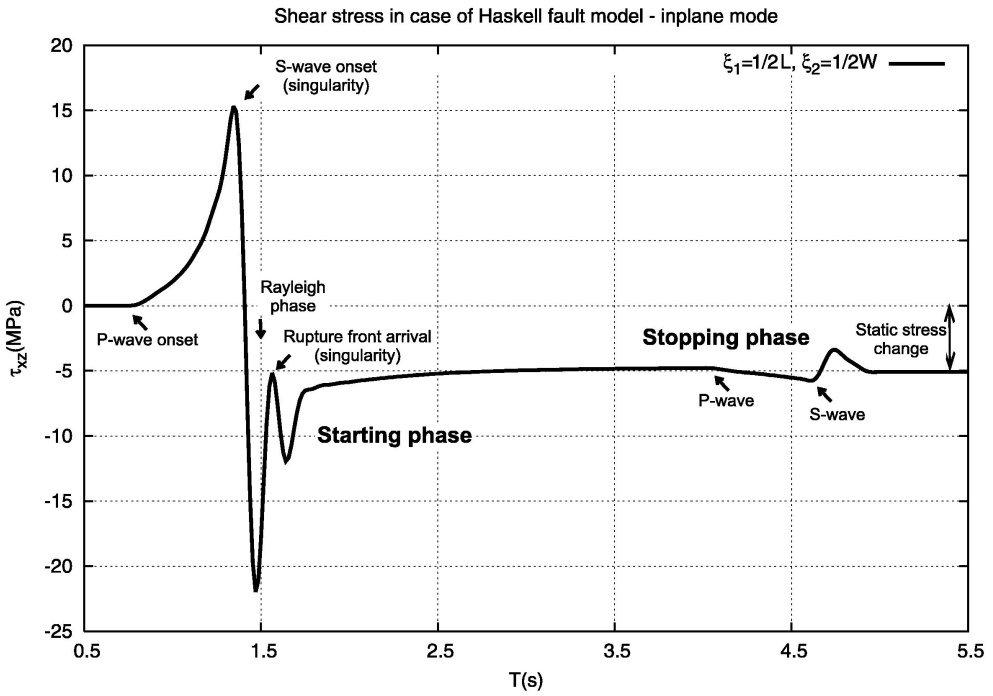

Figure 2.5: Stress time history at the point $\xi_1 = 1/2L$, $\xi_2 = 1/2W$ on the fault for the 'inplane' mode rupture. Distinct phases are annotated.

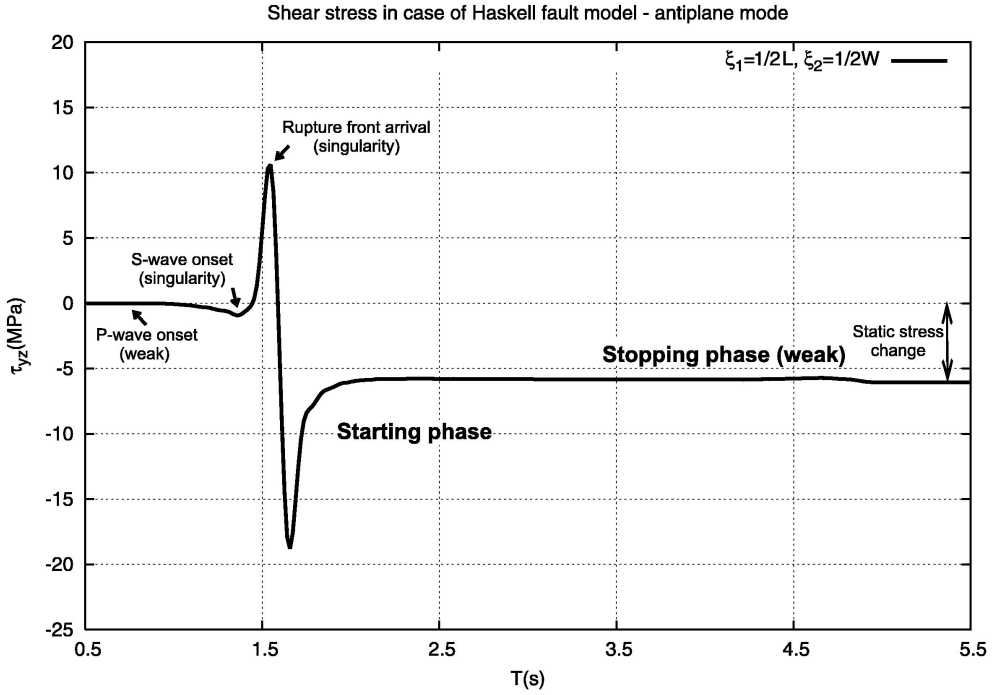

Figure 2.6: Stress time history at the point $\xi_1 = 1/2L$, $\xi_2 = 1/2W$ on the fault for the 'antiplane' mode rupture. Distinct phases are annotated.

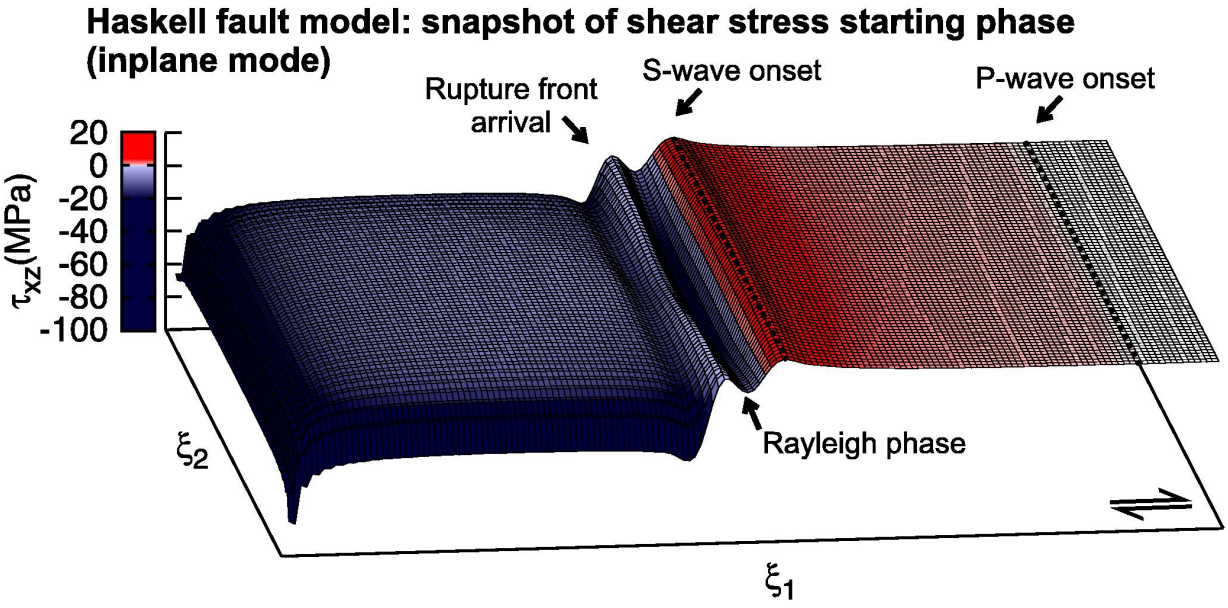

Figure 2.7: A snapshot of starting phase for the 'inplane' mode rupture.

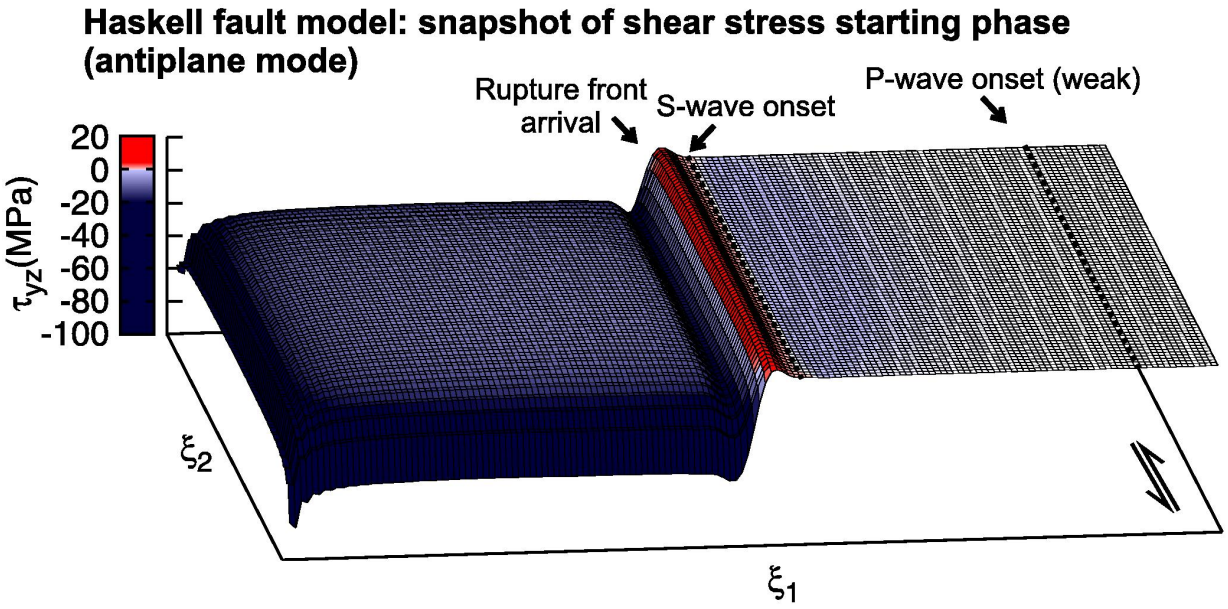

Figure 2.8: A snapshot of starting phase for the 'antiplane' mode rupture.

mode ruptures result in simpler stress time histories.

A snapshot of starting phase at some time $0 < \tau_0 < L/v_r$ is shown in Fig. 2.7 for the 'inplane' mode and in Fig. 2.8 for the 'antiplane' mode. One can see large stress drop (stopping phase does not influence the static solution much, see Fig. 2.5, Fig. 2.6) close to the edge of the dislocation.

2.2.3 Dynamic stress field due to a finite circular crack

Infinitely expanding circular cracks were of the main concern in the 60' and 70', as they presented the simplest 3D solutions for dynamic source models. Kostrov (1964) found analytic self-similar[4] circular crack solution in the isotropic homogeneous space, Burridge & Willis (1969) found analytic self-similar elliptical crack solution in the anisotropic media. These solutions describe cracks starting in a point and expanding self-similarly forever. Dynamic motions due to elliptical crack were further studied in detail by Richards (1976). Although these models are of high theoretical importance, they are hardly applicable for real cases. Analytic solutions for finite sources would be much better applicable, but they are more complicated due to the diffracted waves coming from the crack edges and none of them has been found yet. Madariaga (1976) presented numerical dynamic simulations of finite circular cracks with prescribed rupture velocities. Although, he also presented far-field displacement due to these cracks, near field dynamic stress changes remained unresolved.

Here, we calculate the dynamic stress field due to a circular crack on a planar fault, not yet published (as far as we know). By crack we mean the fault area which undergoes the slip. In this case we are rather interested in the dynamic stress field outside the crack itself, to demonstrate the stress radiation pattern along the fault plane. Our formulation of the problem is different from Madariaga (1976). We prescribe the space-time slip distribution and seek for the space-time stress change distribution, while Madariaga prescribed space-time stress distribution and sought for the space-time slip distribution. We prescribe

[4] In this case, self-similarity means that the slip velocity is a homogeneous function of zero degree, i.e., $\Delta\dot{u}(t, \boldsymbol{\xi}) = \Delta\dot{u}(\boldsymbol{\xi}/t)$.

the space-time slip as follows: the static slip distribution is same as for static circular crack with the constant stress drop using the relation (2.7), the slip is assumed to appear instantaneously, however we remove high frequencies with the cosine window

$$\frac{1}{2}\left[\cos\left(\frac{f}{f_{max}}\pi\right)+1\right] \tag{2.13}$$

which results in the constant finite rise time over the crack. Madariaga did not solve a spontaneous rupture problem, the rupture velocity was prescribed as a constant (either finite or infinite) in his calculations and the final static stress change was the same as in our calculations, thus the only difference is in the slip time functions. Generally, Madariaga's calculations result in non-uniform rise times - the rise time was decreasing with the distance from the crack's center.

Further, we set $v_P = 6.2$ km/s, $v_S = 3.55$ km/s, $\rho = 2800$ kg/m^3, $R = 0.1$ km. The slip was adjusted by changing the constant of proportionality in (2.7) to get the static stress drop of 10 MPa. Such choice was not arbitrary. The values of seismic velocities and density correspond to the seismogenic zone of Western Bohemia (WB) and the source parameters correspond to a WB M2.8 swarm earthquake, as the purpose of these calculations was also to recover possible dynamic stress triggering mechanism controlling the WB seismic swarms. The calculations were carried out up to $f_{max} = 20$ Hz with the following DW configuration (for details, we refer to sections A.3-A.5 of Appendix A): spatial periods $L_x = L_y = 25$ km, time period $T = 3$ s, spatial steps $\Delta x = \Delta y = 8$ m, time step $\Delta t = 3/128$ s, artificial attenuation $\omega^I = \pi/T$, and fault dimensions $L = W = 2.5$ km. An utilization of the cosine window (2.13), f_{max}=20 Hz, static stress drop of 10 MPa and final slip distribution (2.7) results in the maximum slip velocity function of 0.5 m/s at the center of the crack, which is reasonable (e.g., Kanamori, 1994). The slip time functions at several radial positions from the crack's center are shown in Fig. 2.9. The snapshots of both the slip-parallel and slip-perpendicular components of the dynamic stress change over the fault plane are plotted in Fig. 2.10 and Fig. 2.11 respectively. The slip direction is parallel to the horizontal axis. The circular crack can be easily recognized in both figures. Very large stress changes are induced close to the crack and are not resolved by the color

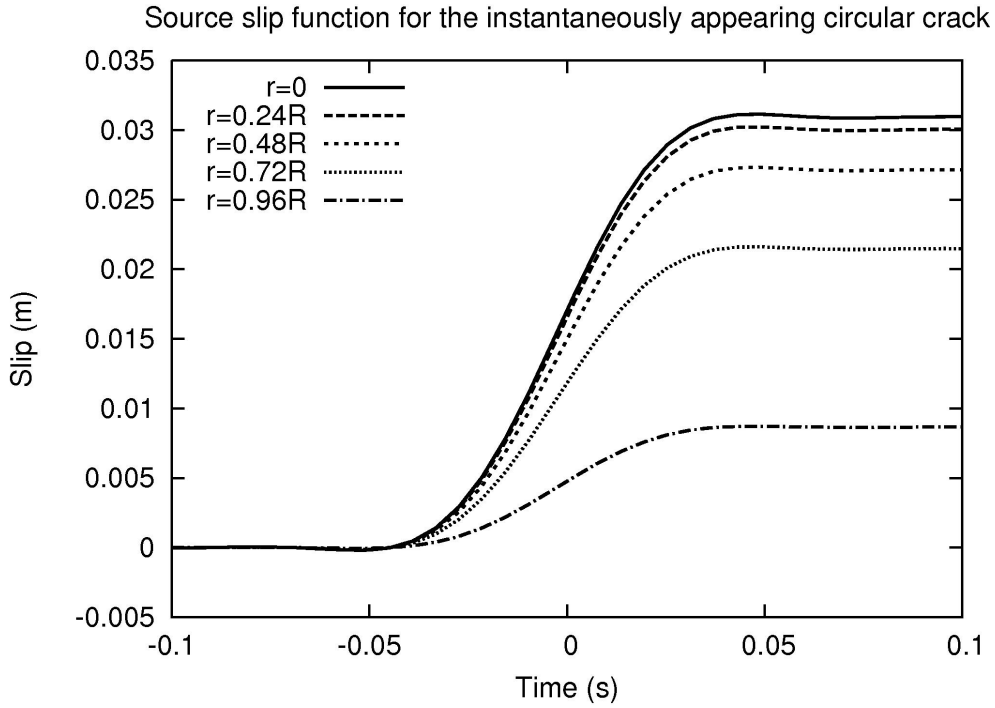

Figure 2.9: Slip functions for several radial distances from the crack's center.

scale. A black color denotes very low values (<-0.05 MPa) and a white color denotes very large values (<0.05 Mpa). The time displayed above each snapshot is measured from zero in the Fig. 2.9.

Let us comment the slip-parallel component of the dynamic stress change (Fig. 2.10). The first snapshot is taken approximately 0.01 s after the slip finished on the crack. One can see the near-field P-wave build up, and how P-waves propagate away from the crack. Moving to 0.2031 s snapshot, one can recognize the near field P-wave (positive onset in the slip direction) followed by the S-wave (overshoot to the negative values and then to the positive values again). Since 0.2500 s snapshot the P-wave has become relatively weak and the transient solution has become controlled by the S-wave. The static solution dominates up to distance of about $5R$ from the center. Maximal slip-parallel stress changes lie on the horizontal crack axis which is parallel to the slip vector. On the other hand, minimal slip-parallel stress changes lie on the vertical crack axis which is perpendicular to the slip vector.

The slip-perpendicular component of the dynamic stress change (Fig. 2.11) has generally a lower magnitude. The stress radiation pattern follows the static stress change distribution. One can again recognize the near field P-wave followed by the S-wave. The static solution dominates up to distance of about R from the center.

The dynamic stress field due to a finite circular crack along a planar fault outside the crack itself has not been published yet. It represents an illustrative solution, reflecting a typical elastodynamic response of the fault walls, throwing some light on the forward dynamic modelling. For example one can read from the results that rupture would rather follow along the slip-parallel direction, as the dynamic stress changes have generally lower magnitude along the slip-perpendicular direction. Further, dynamic stress changes may also induce seismicity (e.g., review by Steacy *et al.*, 2005; and references therein). In particular, these results have been already applied in the study concerning dynamic stress triggering of earthquakes during Western Bohemia seismic swarms published by Fischer & Horálek (2005).

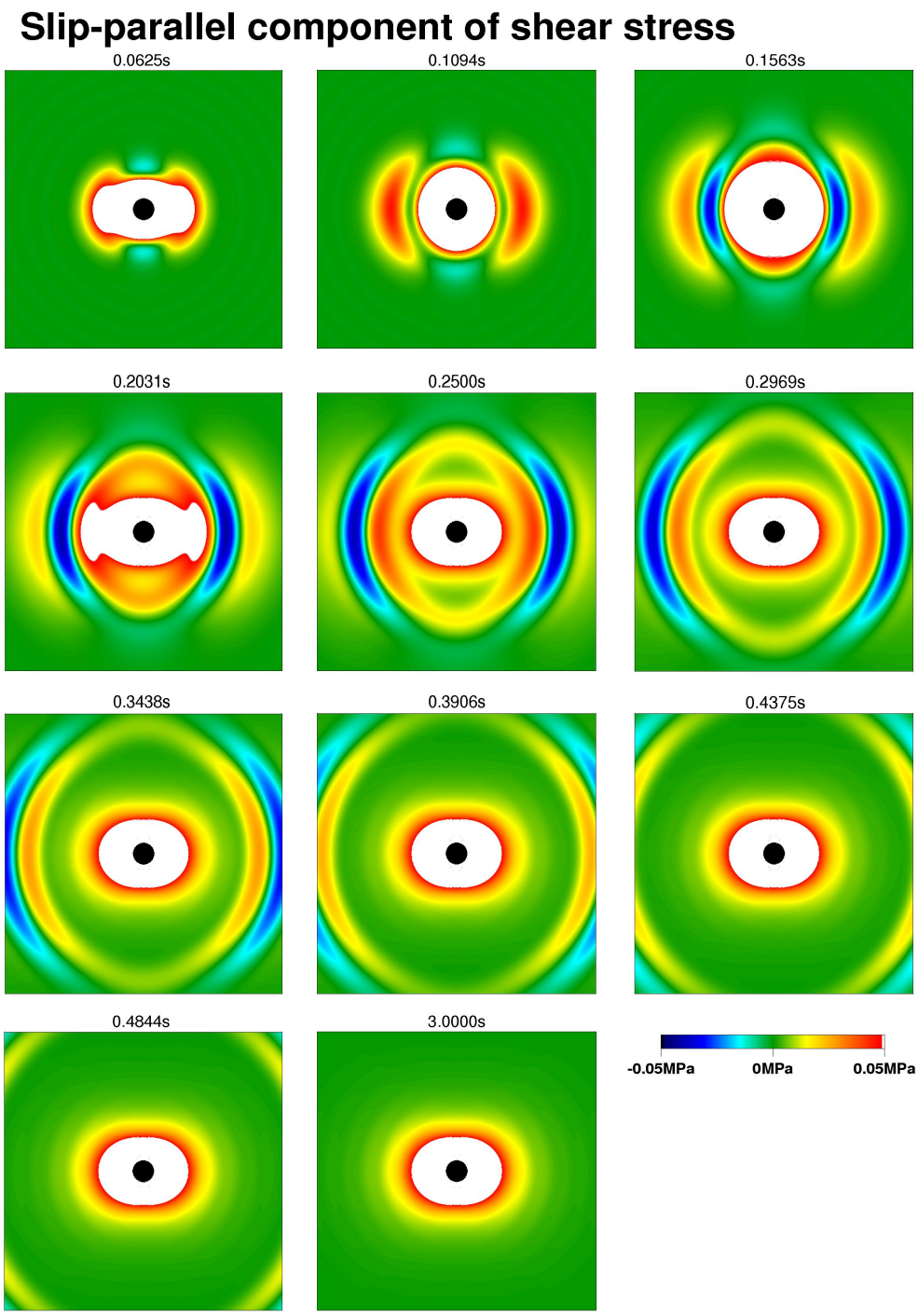

Figure 2.10: Snapshots of the slip-parallel component of the dynamic shear stress change. The values <-0.05 MPa are plotted in black, the values >0.05 MPa are plotted in white. The time measured from zero in the Fig. 2.9 is displayed above each snapshot. Fault plane has dimension of 2.5 km $\times$ 2.5 km.

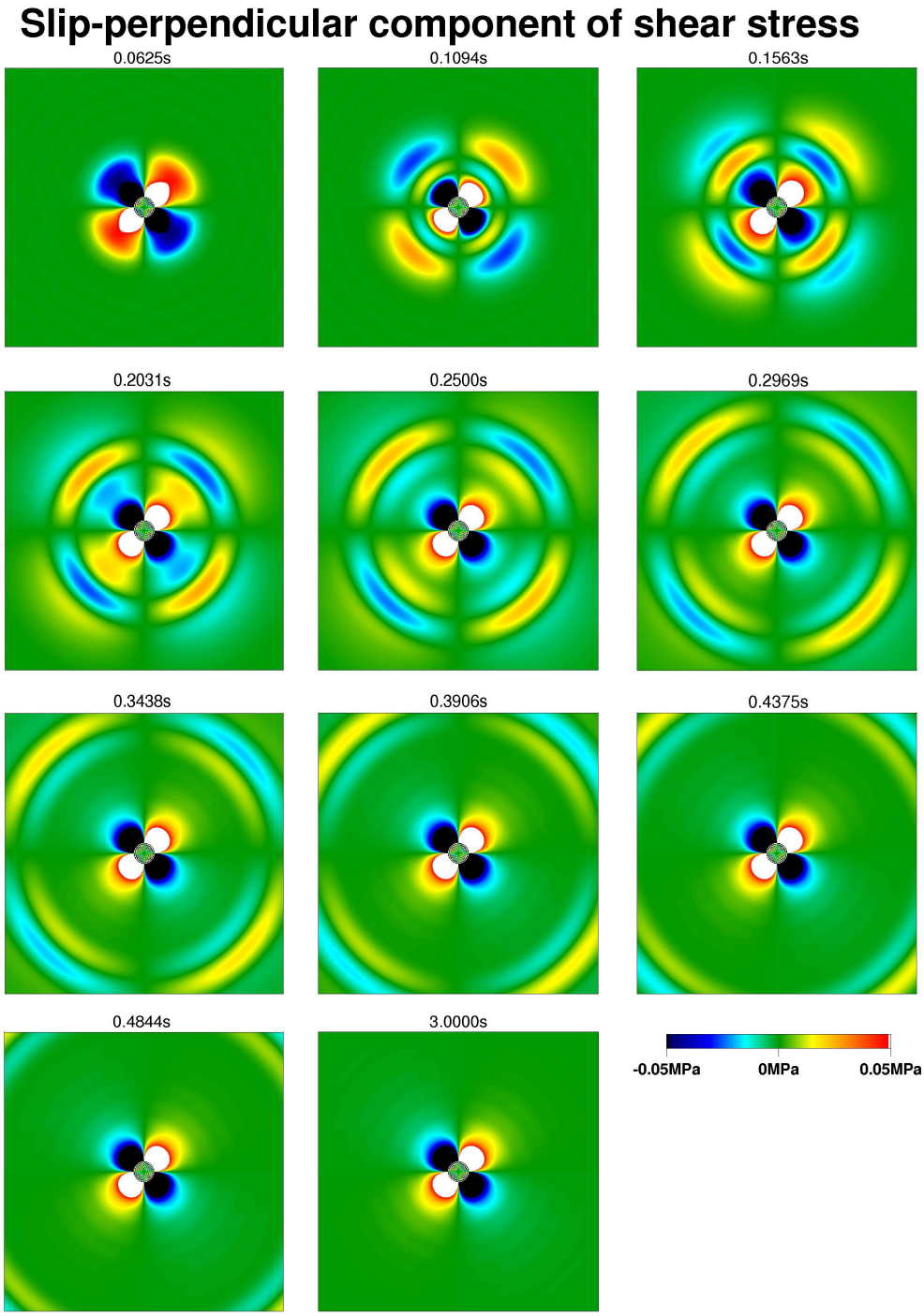

Figure 2.11: Same as in the Fig. 2.10 but just for slip-perpendicular component.

Chapter 3

Dynamic Stress Field of the k-squared Model

In this chapter we describe the k-squared slip model, and present the analysis of the dynamic stress field due to k-squared model with k-dependent rise time. This chapter represents the main results of the thesis.

3.1 Introduction to stochastic source models

Realistic and accurate estimation of strong ground motion in a broad frequency range for future large earthquakes is one of the major topics of present seismology. A realistic earthquake source model should form an integral part of every study concerning strong ground motions in the proximity of an active fault.

It has been recognized soon in seismology, that a stochastic heterogeneity plays an important role in the earthquake source process. This was supported both by a rather complicated, let us say stochastic, high-frequency ground motion due to earthquakes and by a complex seismicity pattern even within a single fault. Both phenomena have been found to embody some specific statistical characteristics, e.g., a power law for frequency-size earthquake distribution, scaling of radiated energy with magnitude, etc. Hence, several stochastic source models were introduced to explain these phenomena. Haskell (1966) presented a kinematic stochastic source model for calculating the stochastic ground motion. Hanks (1979) made a step further, linking the properties of ground motions with the

frequency-size earthquake distribution through stress fluctuations along the fault. Andrews (1980) then introduced an earthquake source model based on the stochastic self-similar static slip and stress distributions, which was primarily designed as a model of the seismicity. Further, Andrews (1981) proceeded with a kinematic stochastic model of the fault motion applicable to the ground motion simulation. A new insight was brought up by Boatwright (1982), who introduced so-called composite source models, where the ground motion due to earthquake was modeled as a series of subevents of various sizes. This concept was further developed by Frankel (1991), who derived theoretical relations connecting the ground motion spectral falloff, fractal dimension of the subevent size distribution and b-value. Although the works by Andrews (1980, 1981) were full of fresh ideas, they were not followed by the thorough studies concerning the influence of the prescribed heterogeneity on the radiated wavefield. Herrero & Bernard (1994) took the stochastic slip distribution of Andrews (1980, 1981) and showed analytically the properties of corresponding radiated wavefield. Particularly, they found that for the slip amplitudes having the spectral falloff proportional to k^{-2} and the instantaneous slip, the radiated wavefield obeys the widely accepted ω-squared model (Aki, 1967). Herrero & Bernard (1994) established the term 'k-squared model' for such stochastic models. Bernard *et al.* (1996) relaxed the unphysical assumption of the instantaneous slip and introduced a slip function with the so called k-dependent rise time, what led to more realistic slip time evolution preserving ω-squared model. Since then, k-squared model was applied in a number of strong ground motion modelling studies (e.g., Zollo *et al.*, 1997; Hartzell *et al.*, 1999; Berge-Thierry *et al.*, 2001; Emolo & Zollo, 2001; Gallovič & Brokešová, 2004b) and further generalized in the following works: Hisada (2000, 2001), Gallovič & Brokešová (2004a), Liu *et al.* (2006).

Concurrently, great effort has been put into the dynamic modeling of earthquake sources; an overview can be found in Madariaga & Olsen (2002). A number of dynamic models of recent earthquakes were also developed (e.g., Quin, 1990; Olsen *et al.*, 1997), since a number of good quality kinematic earthquake source inversions have been obtained and computer power increased. Several attempts have been made to apply these new findings in forward modeling of rupture propagation in stochastic stress fields, to provide

physical scenarios for possible future earthquakes (Oglesby & Day, 2002; Guatteri *et al.*, 2003). Such studies are very valuable since they introduce more physics into the problem, but there are still many open questions concerning possible strength and stress distributions which are generally unknown. Problems are also connected with the computation itself, which is still very time consuming and thus not very convenient for seismic hazard assessment. Another approach is represented by the so-called pseudo-dynamic model of Guatteri *et al.* (2004), who constrain the parameters of the theoretical kinematic model by relations obtained from forward dynamic simulations.

In the present study we follow an alternative way. We investigate the stress field generated by theoretical k-squared kinematic models. Previously, Madariaga (1978) studied the dynamic stress field of Haskell's fault model and found strong contradictions with earthquake source physics (e.g., an infinite average static stress drop). Analogous studies on earthquake source dynamics using kinematic source inversions were presented by Chen & Aki (1996), Bouchon (1997), Ide & Takeo (1997), Day *et al.* (1998), Dalguer *et al.* (2002), Piatanesi *et al.* (2004) and Tinti *et al.* (2005b). These studies led to estimates of fault friction parameters. In this study we calculate the dynamic stress field caused by a slip history prescribed by the k-squared kinematic model. The combination of these stress changes and prescribed slip time series implies a constitutive relation at every point along the fault, and we ask whether these constitutive relations are 'reasonable'. Specifically, we confront these constitutive relations with the slip weakening friction law. We analyze the strength excess, breakdown stress drop, and critical slip weakening distance D_c distributions. A new parameter, the stress delay T_x, is introduced to map the fault points where the peak stress precedes the rupture onset - points where implied constitutive relations violate the slip weakening friction law. We choose the following criteria for the 'reasonable' constitutive relation: 1) minimal areas of stress delay T_x (less than 5% of the fault area), 2) minimal areas of negative strength excess (less than 5% of the fault area). Additionally we require a small ratio of D_c to total slip. If a kinematic source model fails to fulfill these criteria, we suggest its rejection. The choice of 5% is arbitrary.

Another point of this chapter is the analysis of effects of space-time filtering on resulting

dynamic stress field, which is important for the correct interpretation of band-limited slip inversions of real earthquakes.

3.2 k-squared slip model with asperities

Let us introduce the k-squared model with asperities, which is the subject of our further study. The basis of all kinematic k-squared models is a stochastic final slip distribution, which is defined as follows: the amplitude spectrum of the static slip distribution is flat up to a certain characteristic corner wavenumber, then falling off as the inverse power of two, thus matching the condition of self-similarity (Andrews, 1980; Herrero & Bernard, 1994). The corner wavenumber represents the fault roughness. Attempts were made to estimate this wavenumber and spectral falloff from the static slip distributions obtained by kinematic source inversions (Somerville *et al.*, 1999; Mai & Beroza, 2002). However, such results may be biased by the smoothing procedures common to most slip inversions and hence one has to be very careful in taking them into account.

In the paper of Somerville *et al.* (1999), an attempt was made to investigate the heterogeneity of static slip distribution directly in the space domain, defining asperities as regions covering some minimum predefined areas, where the average slip exceeds the prescribed limit. The asperities[1] should represent the behavior of slip models at low wavenumbers. Since the asperities seem to be the dominant regions of the earthquake source in seismic wave generation (Miyake *et al.*, 2003), synthetic slip models for strong ground motion prediction should mimick asperities. The total area of asperities and the area of the greatest asperity exhibit clear seismic moment dependence and thus can be estimated for future earthquakes of a given magnitude. The position of asperities within the fault is difficult to predict, although attempts were made to link the center of the largest asperity with the

[1]We are aware of too many different asperity definitions in seismology. The term asperity was originally introduced in physics of friction for regions of direct material contacts (e.g., Scholz, 2002). To our knowledge it appeared in seismological literature in late 70'. It was used to annotate high-stress drop areas of the fault (e.g, Kanamori & Stewart, 1978; Madariaga, 1979). Since that time it has been used in seismology to call various characteristic fault heterogeneities, including high slip areas (Somerville *et al.*, 1999).

position of hypocenter (Somerville *et al.*, 1999; Mai *et al.*, 2005). Alternatively, attempts have been made to verify the hypothesis of permanent asperities (Irikura, private communication, 2003), who proposes that the asperity always takes the same place on a particular fault.

There are several ways of generating a stochastic k-squared static slip distribution. Most common is the method of filtering noise (Andrews, 1980; Herrero & Bernard, 1994; Somerville *et al.*, 1999; Mai & Beroza, 2002; Gallovič & Brokešová, 2004a). The random phase generator is usually based on either a uniform or Gaussian probability distribution. Such synthetic slip models do not generally provide a direct control of the asperities. Lavallée & Archuleta (2003) applied Lévy probability density function to pronounce asperities. Another way is to assume the asperities in the space domain and add high wavenumber noise with given properties (Gallovič & Brokešová, 2004a). Hence one has a direct control of asperities - one can prescribe the size, the seismic moment and the position of the asperities. It is especially useful in cases when the smooth slip distribution is known (i.e., the properties of asperities). Then the broadband source model can be easily created by adding the high wavenumber stochastic component. Particularly, the 2D Fourier spectrum of the slip distribution reads

$$U\left(k_x,k_y\right)=\frac{\Delta\bar{u}LW}{\sqrt{1+\left[\left(\frac{k_xL}{K_c}\right)^2+\left(\frac{k_yW}{K_c}\right)^2\right]^2}}e^{i\Phi(k_x,k_y)} \tag{3.1}$$

where k_x, k_y are horizontal wavenumbers (in the fault plane), $\Delta\bar{u}$ is the average slip, L is the length and W is the width of the fault, K_c is a dimensionless constant - the relative corner wavenumber, Φ is the random phase function of k_x, k_y. Note that the amplitude spectrum has the form of a low-pass Butterworth filter with the cut-off wavenumber controlled by K_c. By changing K_c we can then demonstrate the effect of spatial filtering of the final slip distribution. The K_c is chosen same for the both k_x and k_y wavenumber directions. However, this may be refined in the future, as fault heterogeneities (e.g., fault geometry) seem to vary differently in the slip-parallel and slip-perpendicular directions (Scholz, 2002; and references therein).

Another approach is represented by superposing slip patches with an average slip proportional to the size of the patch, such that the overall slip provides k-squared falloff at high wavenumbers (Frankel 1991; Zeng *et al.*, 1994; Gallovič & Brokešová, 2007). The position of these patches is random, except for the largest ones, which can be employed to build up an asperity.

We have used both types of k-squared slip generators: the one described in Gallovič & Brokešová (2004a) and the one described in Gallovič & Brokešová (2007). We assume scalar seismic moment $M_0 = 7.8 \times 10^{17}$ Nm released along a rectangular fault, size 11×8 km located in an infinite, homogeneous, isotropic, elastic space characterized by P-wave velocity $v_p = 6$ km/s, S-wave velocity $v_s = 3.46$ km/s and density $\rho = 2800$ kg/m^3. We also assume a rectangular asperity in one corner of the fault with an average asperity slip contrast of 2 following Somerville *et al.* (1999). The direction of the slip vector is constant (parallel to the fault length over the whole fault) to make the analysis easier. Eight different slip distributions are shown in Fig. 3.1A, which all include an asperity with the same properties - rectangular quadrant of the fault with its average slip two times larger than the average slip along the whole fault. One slip distribution was generated by the patch method (vii. slip distribution) with the largest subevent of the asperity size. The other seven were generated by filtering white noise.

The three slip distributions (i., iii., v.) differ only in their relative corner wavenumber K_c (i. - $K_c = 1$, iii. - $K_c = 0.75$, v. - $K_c = 0.5$). All the three were created by filtering white noise ($K_c = \infty$). One can see the effect of K_c - the higher K_c, the rougher the slip distribution. We can interpret alternatively the two slip distributions ($K_c = 0.75$, $K_c = 0.5$) as the low-pass filtered versions of the $K_c = 1$ slip distributions. Thereby we demonstrate the effect of spatial filtering, which is naturally present in kinematic slip inversions. The three slip distributions (ii., iv., vi.) differ from (i., iii., v.) only by the different random seed respectively. The viii. slip distribution is created with the asperity in the center of the fault and with $K_c = 0.5$.

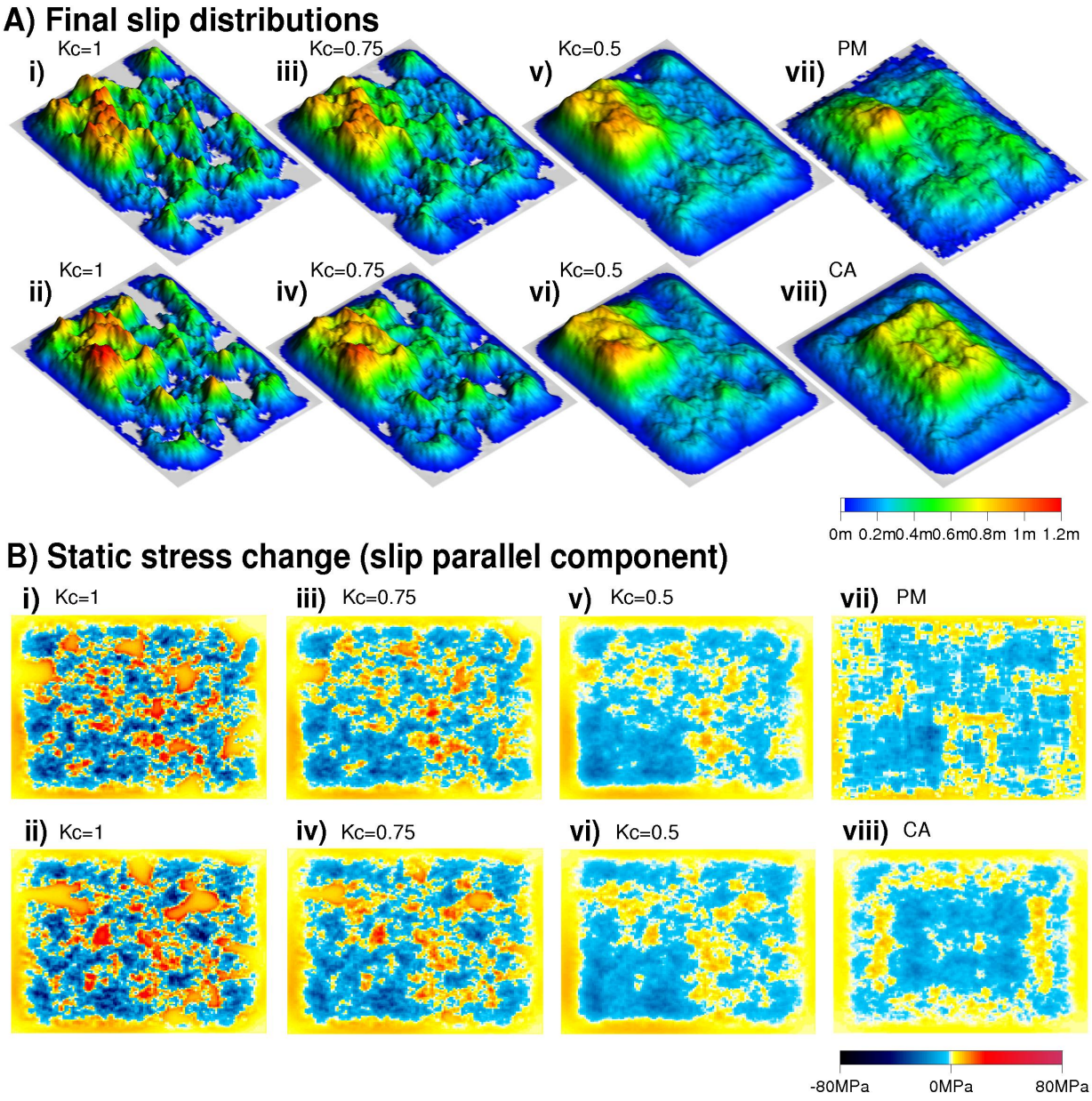

Figure 3.1: Final slip distributions (A) and corresponding slip-parallel static shear stress changes (B). The i-ii. slip distributions were generated with $K_c = 1.00$ for two different random seeds, iii-iv. for $K_c = 0.75$ and two different random seeds, v-vi. for $K_c = 0.50$ and two different random seeds, vii. slip distribution was created by the patch method and viii. slip distribution for $K_c = 0.50$ and asperity placed in the center of the fault

3.3 Static stress field

Firstly we analyze the static stress change along the fault due to the slip distributions described in the previous section. A static stress change due to the self-similar rupture model with the k-squared slip distribution was already studied by Andrews (1980). We extend the study to the k-squared model with an asperity and also for different slip roughnesses. As the fault is planar, the normal stress change along the fault is zero. This could be easily viewed as the normal stress change is a odd function along the fault normal with respect to the fault (e.g., equations A.79-A.80 in the Appendix A) and the stress is continuous across the fault. We thus calculated just the shear traction change expressed in slip-parallel and slip-perpendicular components. The slip-parallel component dominates over the slip-perpendicular component along most of the fault. However, in some sections of the fault both components are comparable. Thus the shear traction change there can become even perpendicular to the slip vector. Nevertheless, the magnitudes of these shear stress changes are low compared to the rest of the fault (up to 10% of the peak shear stress changes). An example of the shear traction change along the fault is shown in Fig. 3.2 for v. slip distribution from Fig. 3.1A. Quantitatively, the shear traction deviates by less than $\pm 45°$, $\pm 15°$, $\pm 10°$ from the slip-parallel direction over 94%, 75%, 61% of the fault area, respectively for the all slip distributions shown in Fig. 3.1A. Let us make a short remark about the relationship between the traction and slip vector along the fault. Generally, initial stress (prestress) has to be accounted in the discussions concerning direction of the slip and the shear stress change along the fault during and after earthquake. A usual assumption in the earthquake dynamics is that the slip rate and the total traction are antiparallel along the fault (e.g., Spudich, 1992). Since the total traction is a sum of prestress (time independent in a time scale of earthquake rupture) and shear stress change perturbation (generally time dependent) due to a slip, the slip rate vector may rotate with time along the fault. Thus the absolute level of prestress plays an important role. If the absolute level of prestress is high, the direction of total traction along the fault will follow prestress and fault will slip in the direction just opposite to the prestress. On the contrary,

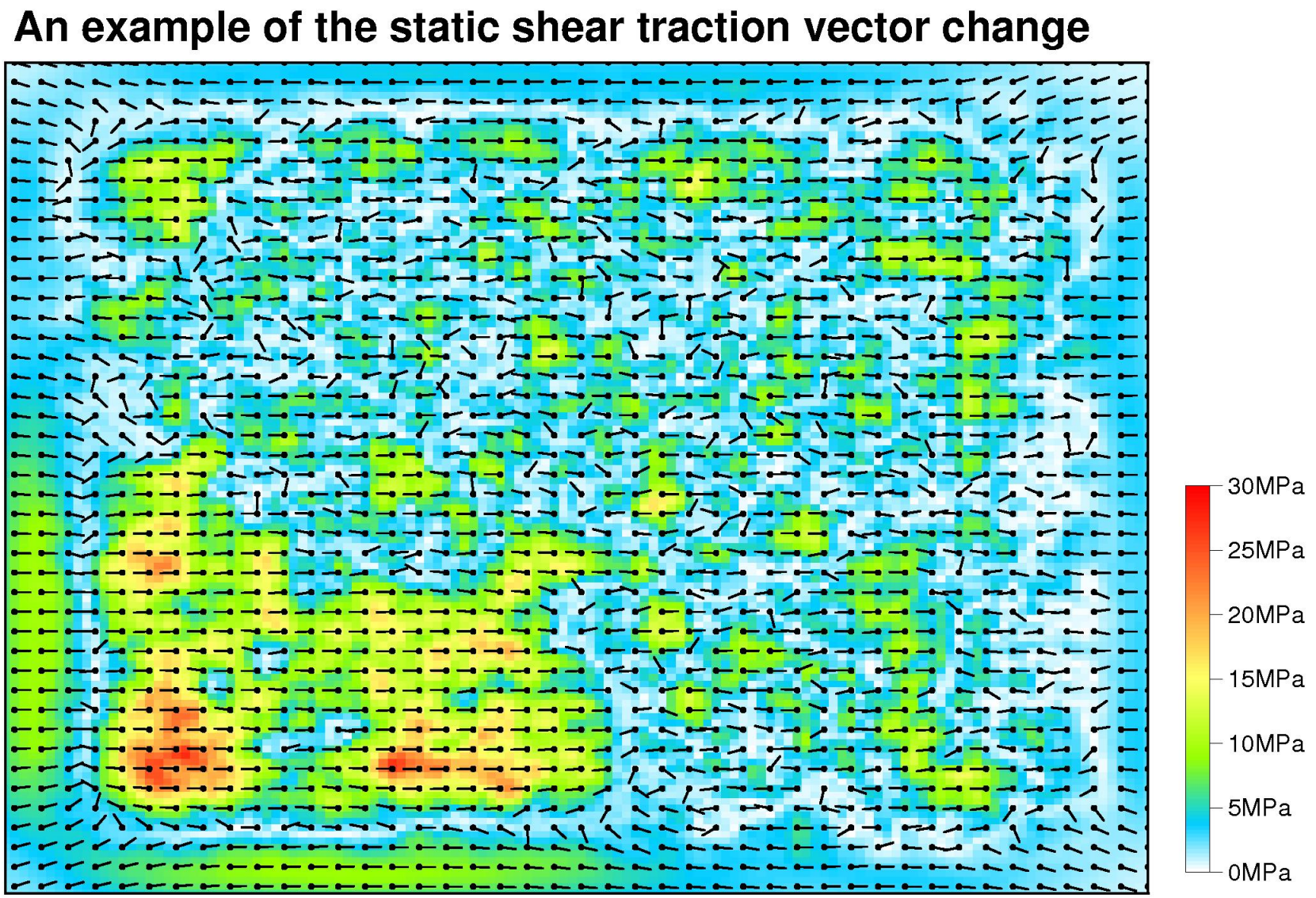

Figure 3.2: An example of the shear traction vector change along the fault for v. slip distribution from Fig. 3.1A. A normalized direction of the traction change is showed by point with a dash. Every third shear traction direction is showed. The traction change magnitude is depicted by a color in the background.

Static Stress Changes								
	$K_c = 1$		$K_c = 0.75$		$K_c = 0.5$		PM	CA
$\Delta\sigma_{min}$ (MPa)	-75	-78	-41	-40	-27	-26	-28	-21
$\Delta\sigma_{max}$ (MPa)	55	57	33	28	17	14	11	11
$\langle\Delta\sigma\rangle$ (MPa)	-1.6	-1.6	-1.6	-1.6	-1.6	-1.6	-1.6	-1.5
$\langle\Delta\sigma^+\rangle$ (MPa)	16.2	16.5	8.8	8.9	5.8	5.8	4.7	4.8
$A^{\Delta\sigma^+}/A^{fault}$ (%)	45	45	49	51	55	54	60	52

Table 3.1: Some basic parameters of the static stress field due to the k-squared slip distributions of Fig. 3.1. $\Delta\sigma_{min}$ and $\Delta\sigma_{max}$ are ranges of the stress changes along the fault, $\langle\Delta\sigma\rangle$ is the average stress change over the fault, $\langle\Delta\sigma^+\rangle$ is the average positive stress drop and $A^{\Delta\sigma^+}/A^{fault}$ is the ratio of the positive stress drop area to the whole fault area.

if the initial prestress is low, the direction of total traction along the fault will rotate with time making also the rake time dependent along the fault. It was shown by Spudich (1992) and Guatteri & Spudich (1998) that estimates of absolute stress levels could be made from time dependent rake rotations. However, prestress is usually supposed to be much higher then stress changes due to earthquakes, thus only slip and traction changes in the prestress direction are assumed.

Rake changes neither with the position along the fault nor with the time in the kinematic model presented here. Hereafter, we work just with the slip-parallel stress change component, assuming an absolute stress level much greater than the stress change. We distinguish the stress drop (or positive stress drop) and negative stress drop if the stress change points along or in the opposite direction of the slip vector, respectively. The results are depicted in Fig. 3.1B. One can see the areas of both the positive (blue) and negative (yellow to red) stress drops. As the vii. slip distribution is smoother, the resulting static stress change appears to be simpler, and almost all the areas of stress drop are connected. On the other hand, the static stress change due to the i. slip distribution is very complex and areas of stress drop create isolated islands. Some characteristics of the static stress change are summarized in Table 1. The average stress change is nearly the same for all K_c slip distributions, but the spatial variability of the static stress change and the area of the negative stress drop increase with increasing K_c. The characteristics of the static stress changes do not change much (up to few percent) with the different stochastic realization.

The vii. slip model will be broadly discussed in further text, as it might correspond to smooth results of kinematic source inversion of real earthquakes. We point out that the limited spatial resolution of the kinematic source inversions can drastically affect the retrieved static stress change. Not enough attention has so far been paid to this important issue.

3.4 Dynamic stress field

If we want to study the dynamic stress field we have to prescribe the slip time history. We have employed Dirac's delta function and slip velocity functions with the so-called k-dependent rise time as, together with the k-squared slip distribution (Herrero & Bernard, 1994; Bernard *et al.*, 1996), they generate the widely accepted ω-squared model. Gallovic & Brokesova (2004a) generalized the concept of the k-dependent rise time for the general slip velocity function (SVF), so that the spectrum of the slip velocity function $\Delta\dot{u}$ can be expressed as:

$$\Delta\dot{u}\left(\boldsymbol{\xi},\omega\right)=\exp\frac{i\omega\left\|\boldsymbol{\xi}-\boldsymbol{\xi}_{hyp}\right\|}{v_r}\int\int_{-\infty}^{+\infty}U\left(\boldsymbol{k}\right)\widehat{X}\left[\frac{\omega}{2\pi}\tau\left(\boldsymbol{k}\right)\right]\exp\left[2\pi i\left(\boldsymbol{k}\cdot\boldsymbol{\xi}\right)\right]d\boldsymbol{k}, \tag{3.2}$$

with

$$\tau(\boldsymbol{k})=\frac{\tau_{max}}{\sqrt{1+\frac{\tau_{max}^2 v_r^2}{a^2}\left\|\boldsymbol{k}\right\|^2}}, \tag{3.3}$$

where ω is the angular frequency, $\boldsymbol{\xi}$ is the position along the fault, $\boldsymbol{\xi}_{hyp}$ is the position of the nucleation point, v_r is the rupture velocity, $\boldsymbol{k}$ is the horizontal wave vector (in the fault plane), $U(\boldsymbol{k})$ is the 2D Fourier spectrum of the static slip distribution, $\widehat{X}$ is the spectrum of the slip velocity function of 1 s duration, $\tau(\boldsymbol{k})$ is the k-dependent rise time, τ_{max} is the maximum rise time, and a is the non-dimensional coefficient described in Bernard *et al.* (1996), where the authors suggested a=0.5. The rupture velocity v_r has to be constant. We have performed the calculation for three SVFs with k-dependent rise time - boxcar, Brune's function and the Kostrov-like function proposed by Hisada (2000) (we have thus denoted it Hisada's function) with maximum rise time $\tau_{max}=1$ s. We have taken $v_r=2.6$ km/s $(=0.75v_s)$. The slip is thus propagating in a pulse of width $L_0=2.6$ km in case of the SVF

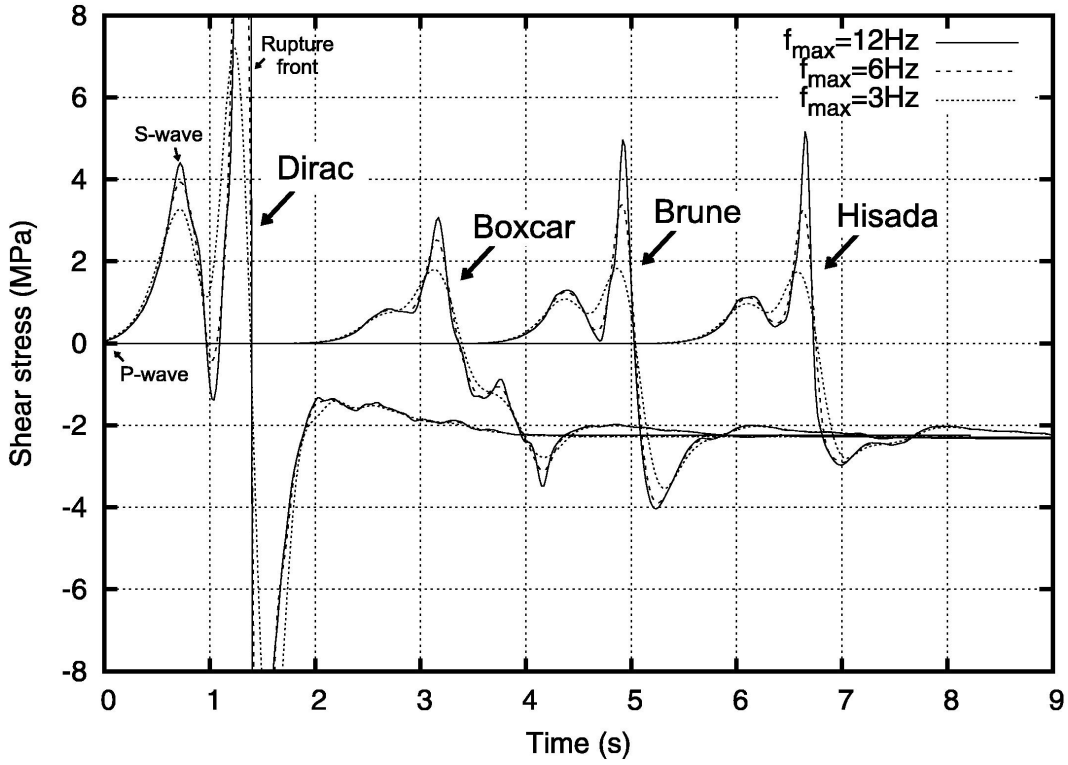

Figure 3.3: Stress time histories for different shapes of slip velocity functions (Dirac's, boxcar, Brune's, Hisada's) at a point of the fault. The slip functions were generated for the slip distribution denoted as PM in Figure 3.1. To demonstrate the effect of filtering we applied the low-pass filter changing cutoff frequency f_{max} gradually ($3Hz$, $6Hz$, $12Hz$). The origin of the time axis is arbitrary and the plots are additionally shifted for clarity by the same amount according to the slip velocity function. The plot is clipped in the case of Dirac's slip velocity function.

with k-dependent rise time. The nucleation point was chosen in the middle of the fault left border - just at the corner of the asperity (indicated later by an asterisk in Fig. 3.5). The calculations were carried out with the following DW configuration (for details, we refer to sections A.3-A.5 of Appendix A): spatial periods $L_x = 1201\Delta x$, $L_y = 1201\Delta y$, time period $T = 10.24$ s, spatial steps $\Delta x = 11/128$ km, $\Delta y = 8/128$ km, time step $\Delta t = 0.02$ s, and artificial attenuation $\omega^I = \pi/T$.

An example of the stress time histories at a point along the fault for four different SVFs is shown in Fig. 3.3. One can recognize the onset due to P-waves, and the peaks associated with the S-wave and rupture front arrivals, respectively, for all types of SVFs.

The static part of the stress histories is independent of SVF. There is a clear singularity associated with the rupture front arrival in case of Dirac's SVF. Brune's SVF is similar to Hisada's SVF, thus the stress time histories are also very similar. We also show the effect of frequency filtering, the stress time histories being plotted for three different cutoff frequencies. As we are working with step-like functions, we use a filter whose Fourier amplitude spectrum falls off very slowly to overcome the spurious overshoots in the signal, i.e. a cosine window $0.5[\cos(0.5\,\omega/f_{max}) + 1]$. The filter is acausal. Note the strong effect of the frequency filtering on the peak stress associated with the rupture onset.

For further quantitative analysis of the dynamic stress field we determine several dynamic source characteristics - strength excess (SE), dynamic stress drop (DS), breakdown stress drop (BS) and stress delay T_x. The definition of these quantities for the representative set of stress time histories is shown in Fig. 3.4. The strength excess (SE) is the value of the stress level (with respect to initial stress) at the very onset of the rupture (e.g., Bouchon, 1997). The dynamic stress drop (DS) is defined as the minimal stress level (with respect to initial stress) after rupture arrival (e.g, Dalguer *et. al*, 2002). The breakdown stress drop (BS) is the sum of the strength excess and the dynamic stress drop. We define BS=0 for points, where it was not possible to read DS, and points where the rupture onset is followed by an immediate stress increase (see Fig. 3.4c). Finally, we define a new quantity, stress delay T_x, as the delay between the rupture front and the peak stress arrivals. If the rupture front arrival coincides with the peak stress arrival, then $T_x = 0$. However, we have found some points along the fault where the peak stress precedes the rupture front arrival ($T_x < 0$). Taking into account simple friction (e.g., the slip weakening law), the fault would start slipping earlier at these points - immediately after the peak stress arrival, which does not agree with the prescribed rupture velocity. Hence, points $T_x < 0$ are very probably inconsistent with source dynamics. Although this opinion is oversimplified and more sophisticated constitutive laws (e.g., the rate and state friction) allow a broader class of stress time histories (even with non-zero T_x), we do not expect the k-squared model to imply such complex friction laws, as it is just a schematic kinematic model.

The spatial distributions of the dynamic parameters for Hisada's SVF are depicted in

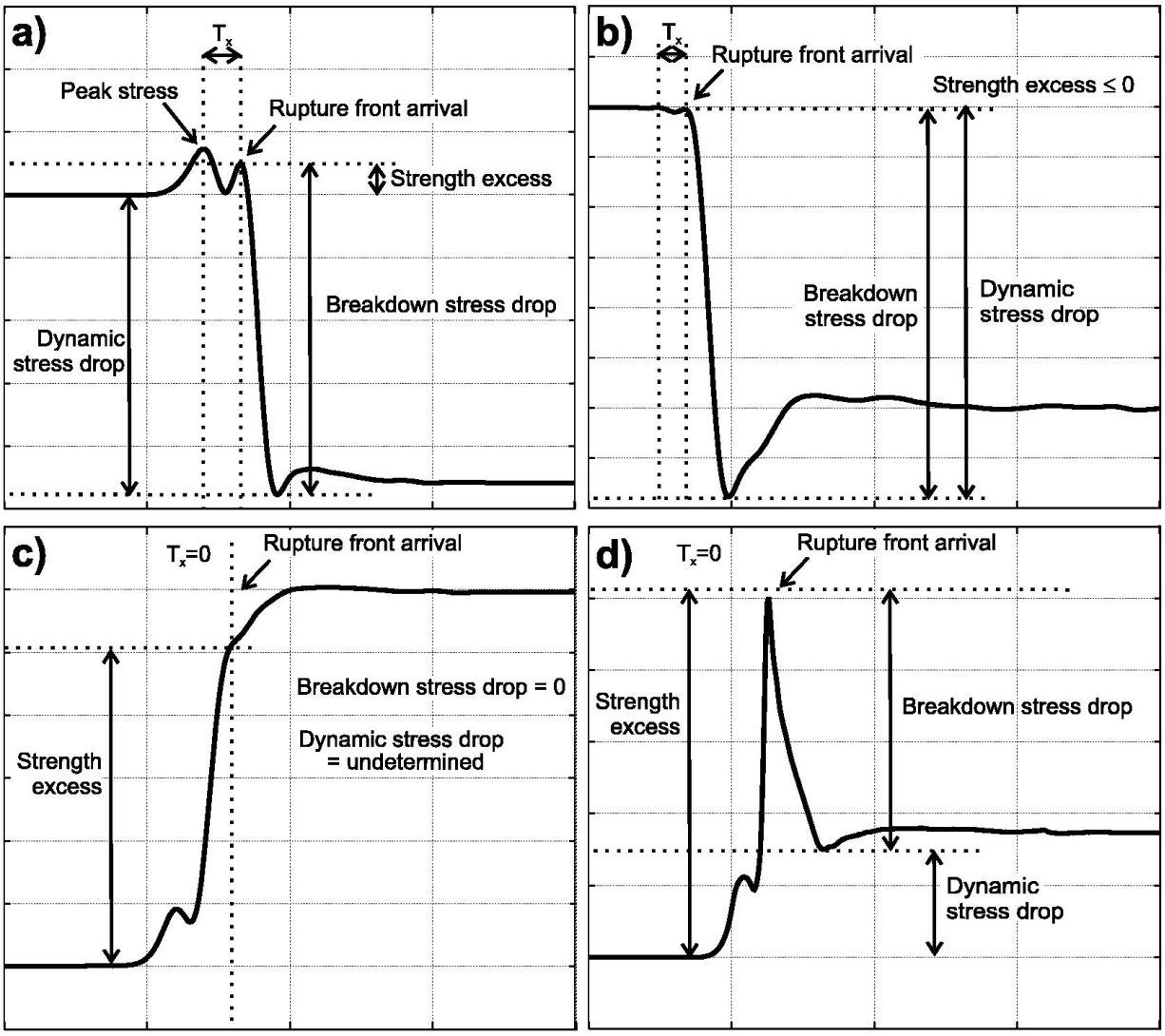

Figure 3.4: Four representative stress change time histories. Reading of the strength excess, dynamic stress drop, breakdown stress drop and definition of stress delay T_x is pointed out for each time history. Cases a) and b) represent time histories with peak stress preceding rupture front onset. Case b) represents the time history with negative strength excess. Case c) represents the time history with immediate stress increase just after the rupture onset - with zero breakdown stress drop. Case d) represents the time history with negative static stress drop but with positive breakdown stress drop.

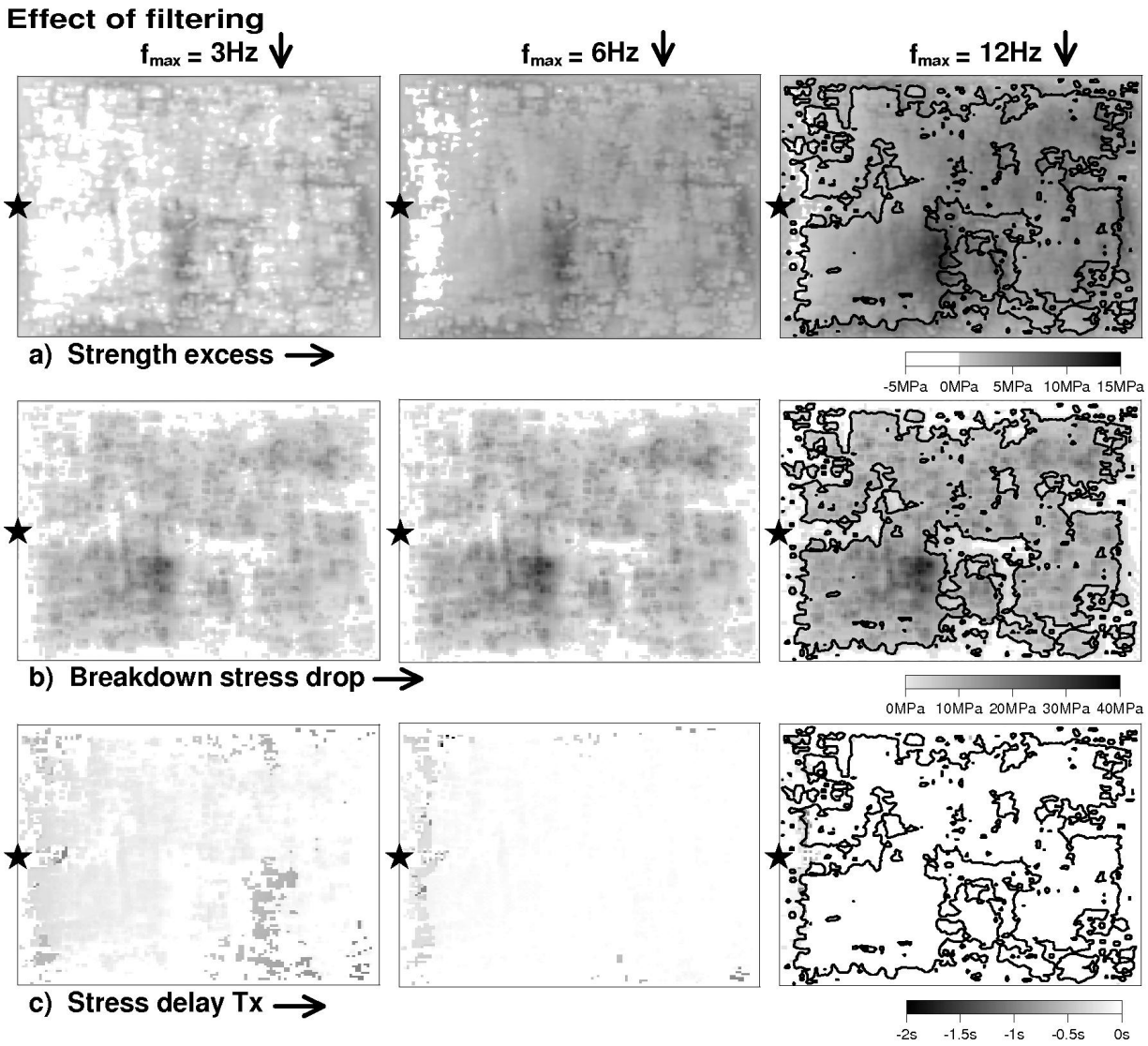

Figure 3.5: The effect of filtering on a) strength excess, b) breakdown stress drop and c) stress delay T_x distributions for Hisada's slip velocity function. Each column of the panel refers to a different cutoff frequency ($f_{max} = 3Hz$, $f_{max} = 6Hz$, $f_{max} = 12Hz$). The black contours in the right column indicate the boundary between positive and negative static stress drops. The nucleation point is indicated by an asterisk.

Fig. 3.5. The white color in the strength excess distribution indicates regions of negative or zero values (values below or equal to the initial stress), which is not physically consistent - these regions ruptured after a zero stress change or even after stress release. We recognize the strong effect of frequency filtering: the peak associated with the rupture front arrival is smeared by filtering (see Fig. 3.3). Since our filter is acausal, the stress drop may precede the rupture front. The problem disappears with increasing cutoff frequency. However, small regions of the negative strength excess remain close to the nucleation point. This is not surprising, as we start the rupture from a point, and not from a small but finite area, the latter being necessary in forward dynamic simulations (e.g., Andrews, 1976a). Bouchon (1997) found that the strength excess inversely correlates with the local rupture velocity. Since we assume a constant rupture velocity, the strength excess is partly correlated just with the static stress change. The breakdown stress drop is clearly correlated with the static stress drop and grows with increasing cutoff frequency. The white color in the break down stress drop distribution indicates regions where the stress just rises in time after rupture front arrival (see Fig. 3.4c). Stress delay T_x is non-zero in the vicinity of the nucleation point, as well as non-positive strength excess regions. Other regions of non-zero T_x disappear with increasing cutoff frequency, except the small areas near the border of the fault.

An example of stress time histories over the fault for Hisada's SVF is shown in Fig. 3.6. The difference between the dynamic and the static stress drop distributions (DS-SS), the stress recovery, is displayed in the background. An interesting result is that the slip pulse propagates without strong recovery of stress along most of the fault, unlike the model of Heaton (1990). Former was also found in the dynamic stress field studies of real earthquakes (Day *et al.*, 1998). However, a closer look at Fig. 3.3 suggests that the amount of stress recovery would depend on the pulse width. Particularly in case of Dirac's SVF, pulse width $L_0 \to 0$, and one can see strong stress recovery. Reminding the reader that $L_0 = v_r\,\tau_{max}$, we carried out the calculation for nine combinations of $\tau_{max} \in \{0.5, 1, 2\}$ s and $v_r \in \{2.3, 2.6, 2.9\}$ km/s with Hisada's SVF, $f_{max} = 12$ Hz and the nucleation point at the left border of the fault. The difference (DS-SS) over the fault is plotted for all the

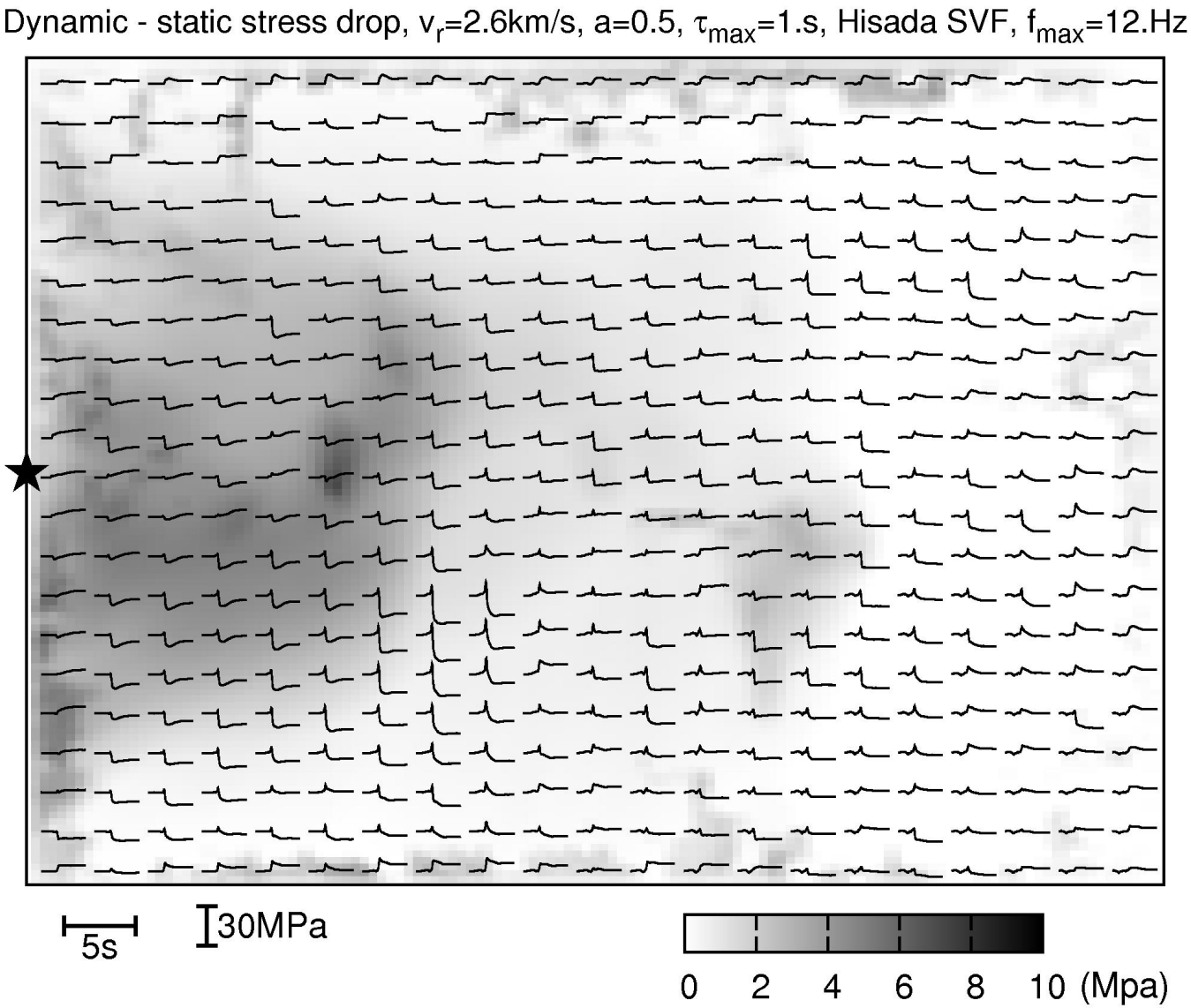

Figure 3.6: An example of stress time histories over the fault for Hisada's slip velocity function and cutoff frequency $f_{max} = 12Hz$. We show just the $3.12s$ window of every sixth time history in both directions. The difference between the dynamic and the static stress drop distributions (stress recovery) is displayed in the background. The nucleation point is indicated by an asterisk.

nine models in Fig. 3.7. We found that the change in the pulse width only causes a change in the absolute values of (DS-SS). The average values of the stress recovery (DS-SS) are plotted against pulse width L_0 in Fig. 3.8, showing that (DS-SS) is inversely proportional to L_0. This is consistent with the analytic relations of Broberg (1978) and Freund (1979), valid for 2D in-plane and anti-plane steady state pulses respectively, which generally imply inverse proportionality of L_0 and DS (the constant of the proportionality depends slightly on the rupture velocity). All calculations resulted in the largest absolute values of (DS-SS) near the nucleation point (see Fig. 3.6). Even in case of narrow pulse $L_0 \simeq 1$ km, the stress recovery (DS-SS) is low (<2 MPa) farther away than $L/2$ from nucleation point.

The concept of the slip pulse was introduced to the k-squared model by Bernard *et al.* (1996) just by assumption. Slip pulses are usually observed in kinematic models of past earthquakes (Heaton, 1990), however, their origin is not clear. Two possible mechanisms were presented to explain the existence of slip pulses (for a detailed discussion refer to Ben-Zion, 2001). One explanation is a large dynamic variation of the frictional force along the fault, which can be caused, e.g, by a strong velocity dependence of the friction coefficient (e.g., Heaton, 1990) or by the variation of the normal stress along the fault separating two materials with different properties - the so-called wrinkle pulse (e.g., Andrews & Ben-Zion, 1997). Another explanation is that the slip pulse is just the result of fault heterogeneities, which was demonstrated not only in theoretical forward dynamic models (e.g., Das & Kostrov, 1988), but also in models of particular earthquakes (Beroza & Mikumo, 1996; Day *et al.*, 1998). The latter explanation is consistent with the k-squared model with broader pulses ($L_0 > L/5$), as we do not observe stress recovery after dynamic weakening. The slip pulse could then be substantiated by the natural spatial heterogeneity of the k-squared model. The limit $L_0 > L/5$ confirms the value proposed by Bernard *et al.* (1996) for a crack like behavior of 'broad-pulse' slip model. In case of narrow pulses ($L_0 < L/5$) stress recovery is significant close to the nucleation point and, therefore, the slip pulse cannot be explained merely by fault heterogeneity.

In earthquake dynamics, the source process is controlled by the instantaneous stress state surrounding the fault and the constitutive equations describing the relationships

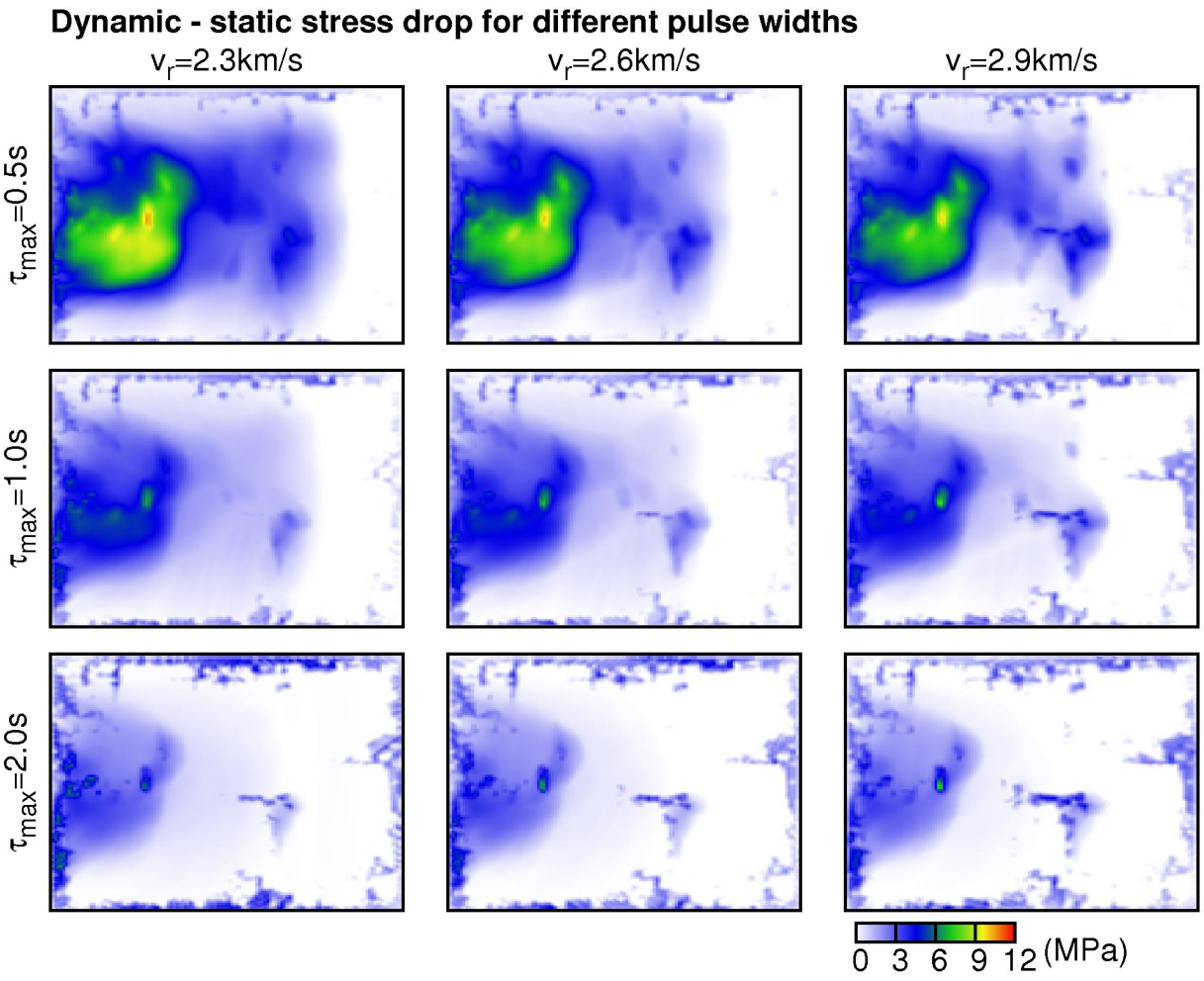

Figure 3.7: The difference between static and dynamic stress values over the fault. The simulations were run for Hisada's slip velocity function, nucleation point at the left border of the fault and nine combinations of $\tau_{max} \in \{0.5, 1., 2.\}$ s and $v_r \in \{2.3, 2.6, 2.9\}$ km/s. We remind that $L_0 = v_r \tau_{max}$.

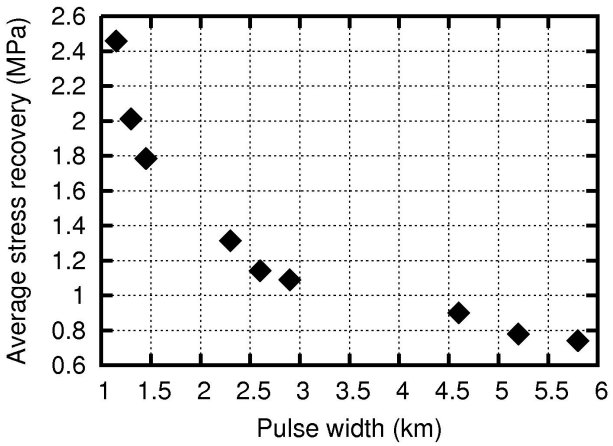

Figure 3.8: The mean value of the difference between static and dynamic stress drops over the fault in dependence on pulse width L_0. The average values were obtained from the distributions depicted in Fig 3.7.

among the kinematic, mechanical, thermal or even chemical field variables along the fault. One of the simplest and most widely used constitutive equations is the slip weakening (SW) law introduced to earthquake source studies by Ida (1972). It relates shear traction along the fault only to the fault slip. An example of the linear slip weakening friction law is depicted in Fig. 3.9. In particular, a slip is zero until shear stress reaches (from the initial stress level τ_0) a critical value - the yield stress (τ_y). Once the yield stress is reached, the slip starts to grow while the shear stress decreases. After the slip exceeds the critical displacement D_c, the shear stress no longer decreases and remains constant at the so-called dynamic stress level (τ_d) till the end of the rupture process. Hatched region denotes the work per area done against friction in producing the crack (fracture energy density, shortly fracture energy) and cross-hatched region denotes the energy per area transformed to heat (Andrews, 1976a). The boundary between the fracture energy and heat may be more complicated and may not follow the dynamic stress level τ_d, which may be refined in the future (see discussion by Tinti *et al.*, 2005b). Although other constitutive laws exist, e.g., the rate and state dependent friction law derived from laboratory rock friction measurements (Dieterich, 1979; Ruina, 1983; Marone, 1998) and explaining even pre- and post-seismic phenomena, the SW law has been used successfully to interpret

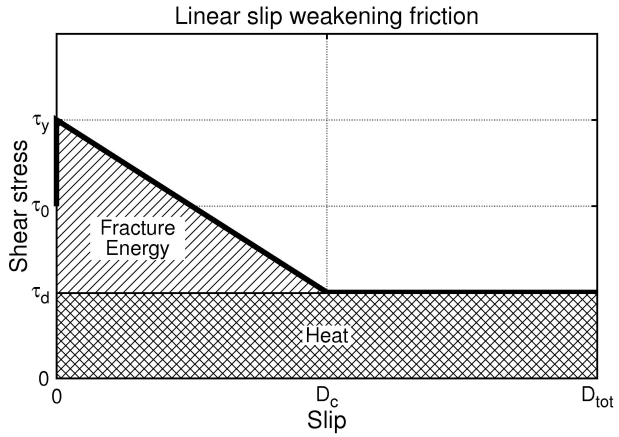

Figure 3.9: An example of the slip weakening friction law. Thick solid line represents the shear stress dependence on the slip at a point on the fault. τ_0, τ_y and τ_d denote the initial, yield and dynamic stress levels respectively. D_c is the critical slip weakening distance and D_{tot} is the final slip. Hatched area denotes the fracture energy and cross-hatched denotes the energy per area transformed to heat.

ground motions with dynamic models (e.g., Beroza & Mikumo, 1996; Olsen *et al.*, 1997; Guatteri & Spudich, 2000; Peyrat & Olsen, 2004). Moreover, the SW behavior was found to be a feature of the rate and state dependent friction law itself (Cocco *et al.*, 2004 and references therein) and also in the dynamic stress field of the kinematic models derived by the inversion of earthquake waveforms (Ide & Takeo, 1997). Since SW is an important feature of the dynamic stress change during earthquake rupture, we analyzed the stress slip curves for the k-squared model. We fitted stress slip curves using the linear SW relation (the stress falls linearly with the slip), arriving at the optimal value of D_c. Particularly, we fixed both the strength excess and dynamic stress drop and performed a direct search in the interval $\langle 0, D_{tot} \rangle$ for optimal D_c (in the sense of the L2 norm), D_{tot} is the final slip. An example of such optimal solution over the fault is in Fig. 3.10 and in more detail for eight selected points in Fig. 3.11. SW dominates in regions of positive static stress drop, where the variance reduction of the optimal solution exceeds 90%. Regions of negative static stress drop and positive breakdown stress drop exhibit slip weakening or a combination of slip weakening and slip hardening. The SW fit is generally worse (variance reduction up to 50%) in these regions. The SW fit has no meaning in regions of zero breakdown stress drop.

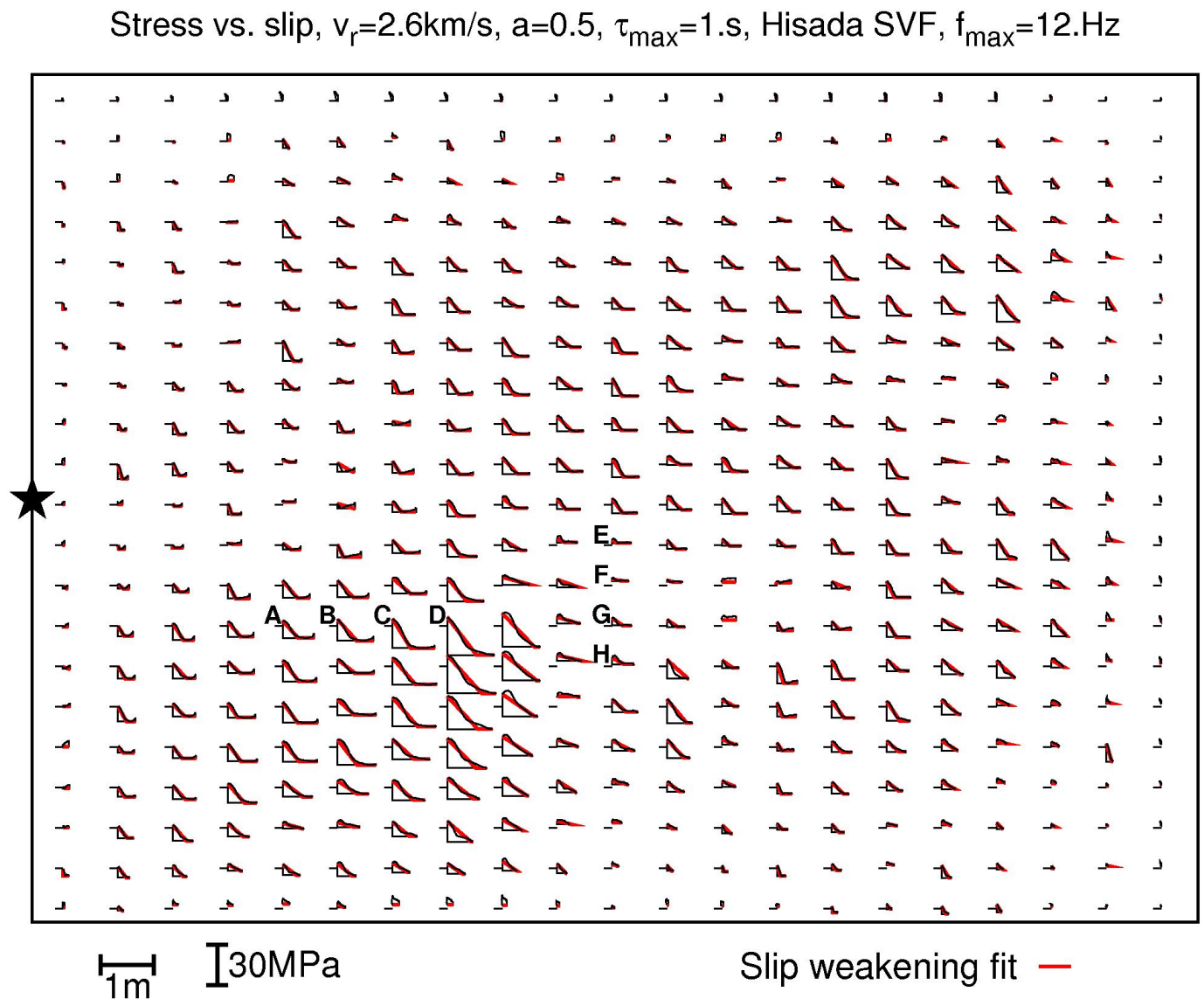

Figure 3.10: Stress-slip diagrams for Hisada's slip velocity function (black) with corresponding linear slip weakening fit (red). We show every sixth stress-slip diagram in both directions. The initial stress level is marked by a short dash. The nucleation point is indicated by an asterisk. The stress-slip curves denoted by A - H are shown in Fig. 3.11.

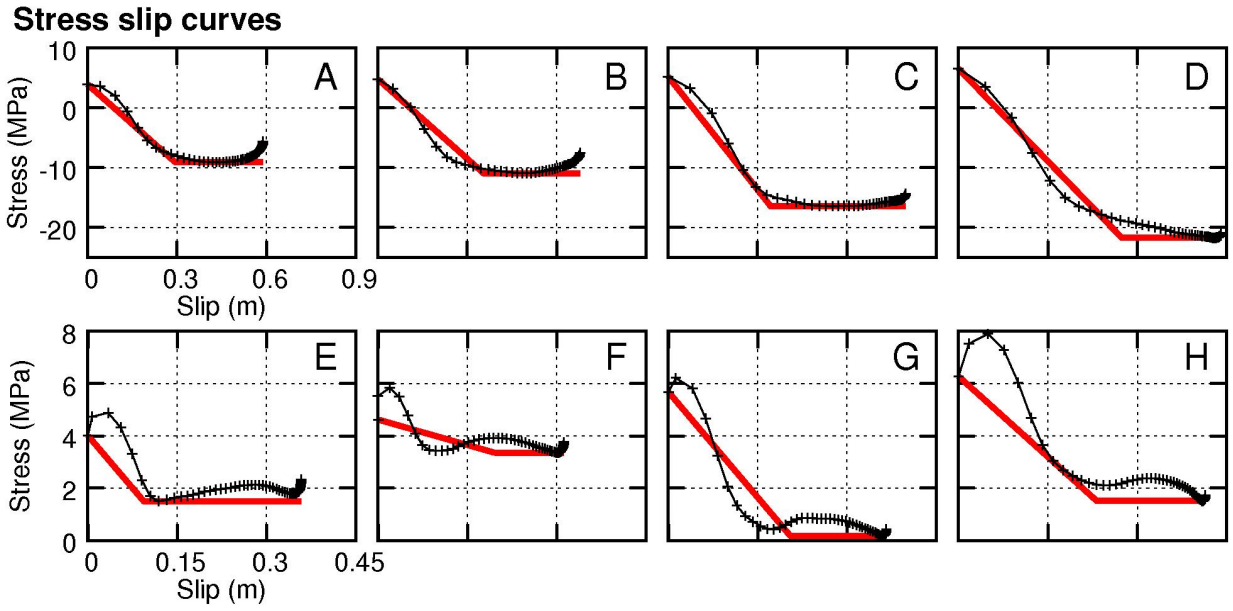

Figure 3.11: An example of stress-slip curves (black) and corresponding linear slip weakening fit (red) at eight points along the fault denoted in Fig. 3.10 by A - H respectively. A worse fit in the negative static but positive breakdown stress drop areas is presented in the bottom row (E-H).

The optimal values of D_c/D_{tot} for three values of f_{max} are plotted in Fig. 3.12. We show D_c/D_{tot} just for areas of positive static stress drop, as there is a high reduction variance of the slip weakening fit (over 90%) for the three values of f_{max} and thus the results are comparable. One can see that the values of D_c/D_{tot} depend on the cut-off frequency - the lower f_{max}, the closer D_c to D_{tot}. Generally, D_c follows D_{tot}, but D_c/D_{tot} slowly varies along the fault from 20% to 40%, to 60% to 100% for f_{max}=12 Hz, 6 Hz, 3 Hz, respectively. Total slip D_{tot} versus D_c for all points within positive stress drop areas is plotted in Fig. 3.13 to be comparable with the published results for real earthquakes. The effect of filtering is clear, a lower f_{max} pushes the values of D_c closer to D_{tot}. Note the points $D_c = D_{tot}$. The scaling becomes less apparent for $f_{max} = 12\ Hz$, but generally still holds. Both the green and red lines denote maxima of the D_c/D_{tot} frequency-magnitude distributions shown later in Fig. 3.18. The scaling of D_c with the final slip was found by Mikumo *et al.* (2003), Zhang *et al.* (2003) and Tinti *et al.* (2005b) for several earthquakes. However, Spudich & Guatteri (2004) pointed out that this could be caused by the limited bandwidth of the

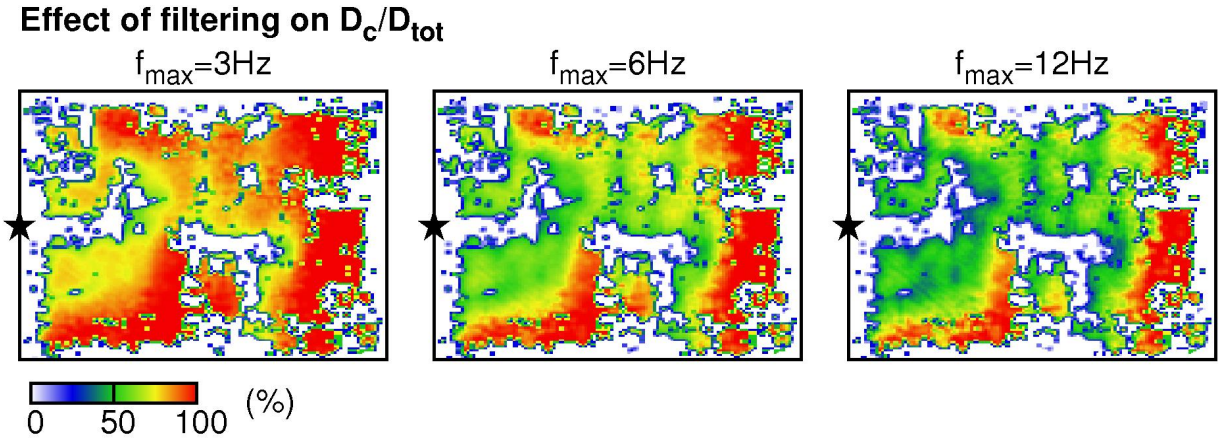

Figure 3.12: The effect of filtering on D_c/D_{tot} (ratio of critical and total slip) distributions for Hisada's slip velocity function. Three cutoff frequencies are considered ($f_{max} = 3Hz$, $f_{max} = 6Hz$, $f_{max} = 12Hz$). The nucleation point is indicated by an asterisk.

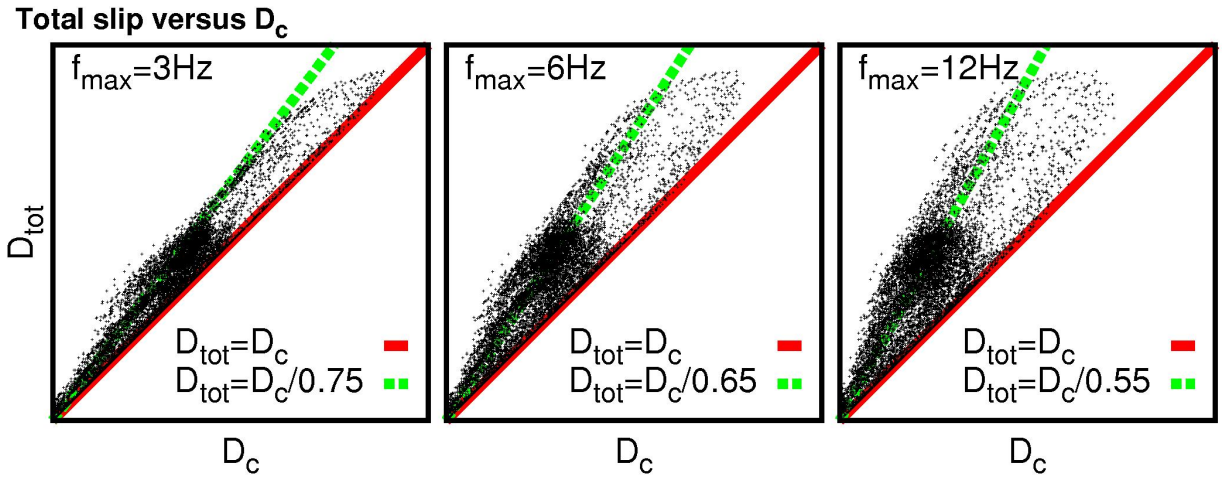

Figure 3.13: Total slip D_{tot} versus critical slip D_c at points within positive stress drop areas and for three filter cutoff frequencies ($f_{max} = 3Hz$, $f_{max} = 6Hz$, $f_{max} = 12Hz$). The red solid line indicates 1:1 ratio. The green dashed line indicates a maximum of the D_c/D_{tot} frequency-magnitude distribution (see later Fig. 3.18).

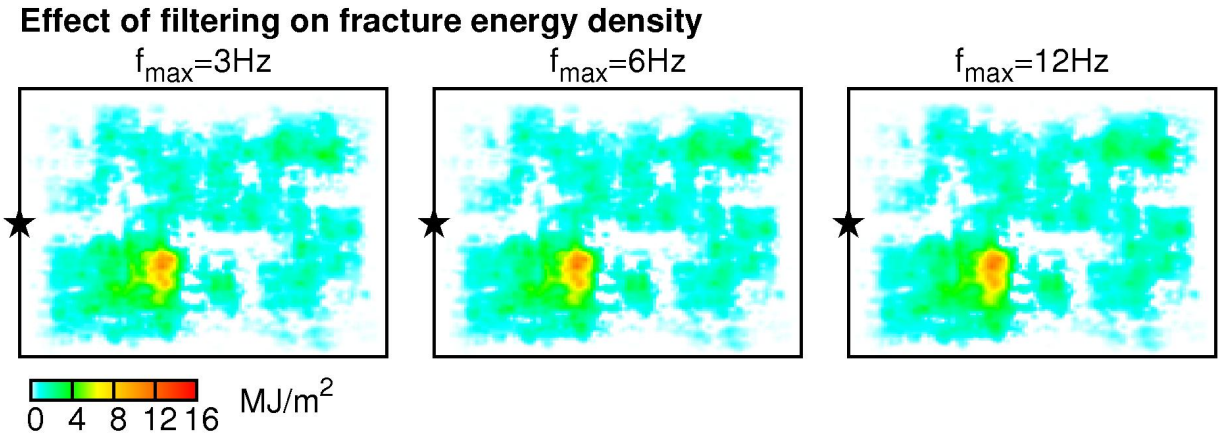

Figure 3.14: The effect of filtering on the fracture energy density distributions calculated from the breakdown stress drop and D_c distributions presented in Fig. 3.5 and Fig. 3.12 respectively. Three cutoff frequencies are considered ($f_{max} = 3Hz$, $f_{max} = 6Hz$, $f_{max} = 12Hz$). The nucleation point is indicated by an asterisk.

kinematic inversions. Our results are similar to that of Zhang's results for $f_{max} = 6$ and 12 Hz and Tinti's results for $f_{max} = 3$ Hz. On the other hand Mikumo presented lower values of D_c/D_{tot} from the interval (0.27-0.52) for Tottori earthquake. Though, it has been already pointed by Mikumo *et al.* themselves, that their D_c estimation method fails near strong barriers - exactly at the regions where we find $D_c/D_{tot} \simeq 1$. Actually, the D_c estimates for earthquakes are quite peculiar (Guatteri & Spudich, 2000) and it seems that recent kinematic source inversions were unable to resolve D_c correctly due to the limited bandwidth of the data (Spudich & Guatteri, 2004; Piatanesi *et al.*, 2004). Therefore it is difficult to compare the D_c from observational studies with the D_c we obtained for the theoretical k-squared model in this study.

If we have both the breakdown stress drop τ_b and D_c estimates, it is straightforward to evaluate also the fracture energy density G_c assuming the slip weakening friction of Andrews (1976a), so that

$$G_c = \frac{1}{2}\tau_b D_c. \tag{3.4}$$

Fracture energy density distributions are shown in Fig. 3.14 for the three values of f_{max}. One can see that the fracture energy is quite unaffected by the frequency filtering and is correlated with the static slip distribution. The absolute values are of the same order

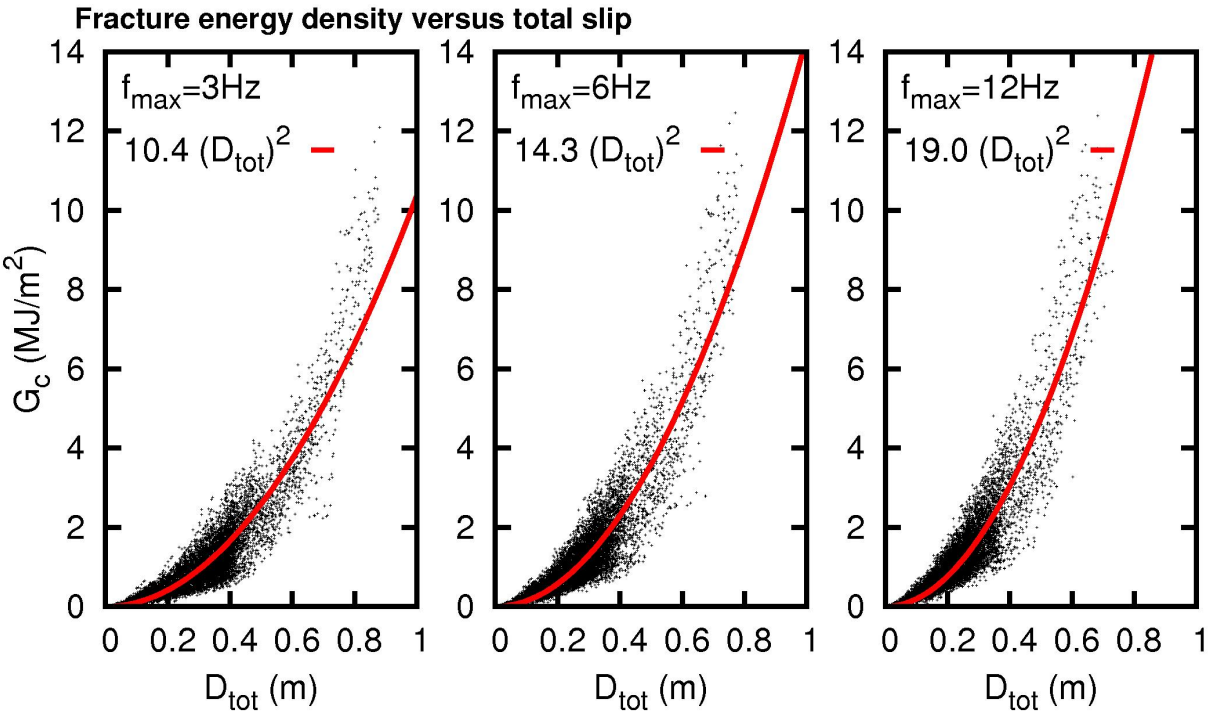

Figure 3.15: Fracture energy density G_c versus total slip D_{tot} for the all points along the fault and for three filter cutoff frequencies ($f_{max} = 3Hz$, $f_{max} = 6Hz$, $f_{max} = 12Hz$). The red solid line indicates the fit by a quadratic function.

of these found by Tinti *et al.* (2005b). We also made plots of the fracture energy values against total slip for all points over the fault (Fig. 3.15). Fracture energy density was found to scale with a second power of the local slip, which is in agreement with both the results of Tinti *et al.* (2005b) for real earthquakes and results of Rice *et al.* (2005) for 2D steady state slip weakening pulse model. As it was pointed by Tinti *et al.* (2005b), such scaling is not in agreement with the one originally proposed by Andrews (1976a). Andrews presented the fracture energy dependent on the length of the crack from the nucleation point. The k-squared model with the k-dependent rise time thus seems to be self-consistent from this point of view - it includes slip pulse and the fracture energy follows scaling independently predicted by Rice *et al.* (2005) for the dynamic source pulse model.

The fracture energy seems to be a stable parameter, insensitive to the frequency filtering, thus the estimations for the real earthquakes might be promising from this point of view. On the other, there is a clear trade-off between strength excess and D_c distrib-

utions. These findings are in agreement with Guatteri & Spudich (2000), Peyrat *et al.*, 2001, Peyrat & Olsen (2004).

3.5 A parametric study

As the k-squared model with k-dependent rise time has a relatively high number of free model parameters (length and width of the fault, asperity slip contrast, slip roughness - represented by K_c, stochastic slip distribution, number and positions of asperities, position of nucleation point, rupture velocity, maximum rise time, coefficient a, and SVF type), it represents a large set of source models. We have performed a parametric study which covers some sections of this model space to explore its projection into the space of dynamic parameters, and to possibly find some restrictions on the k-squared model originating from source dynamics. The scope of the parametric study is limited. We have focused on the combination of low-wavenumber deterministic and high-wavenumber stochastic slip model of $M_w = 5.9$ earthquake. The low-wavenumber model (fault and total asperities area, asperity slip contrast, number of asperities - in this case just one deterministic asperity) is based on the empirical scaling relations of Somerville *et al.* (1999). We have varied the rupture velocity, maximum rise time, nucleation point position, SVF type, stochastic slip distribution and asperity position. Each of these were studied separately, fixing the other parameters at the reference values. The model, which was analyzed in the previous sections (Hisada's SVF, $v_r = 2.6$ km/s, a=0.5, $\tau_{max} = 1$ s, $f_{max} = 12$ Hz) served as a reference model. The results of the parametric study are presented in Fig. 3.16, Fig. 3.17 and Fig. 3.18. D_c/D_{tot} is plotted just for areas of positive static stress drop, as the reduction variance of the slip weakening fit is 90±5% for all models in these areas, except for the case of $v_r = 3.18$ km/s (65%). Thus D_c/D_{tot} should be comparable in the different models. Further, it was difficult to represent D_c/D_{tot} by a single value (e.g, by the average value), since its frequency-magnitude distribution has 2 local maxima (at $D_c/D_{tot} = 1$ and $D_c/D_{tot} \simeq 0.5$), hence we plot frequency-magnitude distribution for all models in Fig. 3.18. The frequency magnitude distributions of strength excess, breakdown stress drop and frac-

ture energy density are also plotted in Fig. 3.18 to present the differences between the studied models in more comprehensive way.

3.5.1 Rupture velocity

The information on the earthquake rupture velocity generally comes both from the seismological observations and theoretical dynamic source models concerning spontaneous rupture propagation. Particularly, the maximum possible rupture velocity has been discussed broadly since first earthquake dynamic models appeared in late 60'. Several authors proposed different limits for rupture speed - Rayleigh speed (v^R) limit for in-plane fracture mode and shear wave speed (v_S) for anti-plane fracture mode for perfectly brittle bodies[2]. This has been supported by many observations of average rupture speeds of $0.7 - 0.9v_S$. However, Andrews (1976b) showed both theoretically and numerically that for the non-ideally brittle bodies and in-plane fracture mode (particularly for the slip weakening friction law) rupture speed v_r can exceed v_S a can even reach P-wave velocity v_P. The transition from v^R to supershear speeds is not smooth, the rupture front makes a sudden jump ahead (e.g., Andrews 1976b, Dunham *et al.*, 2003). Nevertheless, supershear rupture velocity remained mysterious as it was not validated by observations for a long time. The first observations of supershear rupture speed in laboratory were reported by Rosakis *et al.* (1999). Moreover, Bouchon *et al.* (2001) and Bouchon & Vallée (2003) found supershear rupture speed for the two 1999 Turkey earthquakes and 2001 M8.1 Kunlunshan, Tibet earthquake respectively.

As the transition from the Rayleigh to supershear speeds is complicated, we decided to study at first sub-Rayleigh velocities. Particularly, we set v_r to values of 2.3 km/s(=$0.66V_s$), 2.9 km/s(=$0.84V_s$) and 3.18 km/s(=$0.92V_s$) (Fig. 3.16b-d). The last one is the Rayleigh velocity v^R in the medium surrounding the fault. The strength excess (SE) distribution is very sensitive to rupture velocity v_r. Specifically, the SE values decrease almost linearly with v_r (the average positive SE values decrease linearly from 5 MPa for $v_r = 2.3$ km/s to 1.8 MPa for $v_r = 3.18$ km/s). The spatial pattern of the SE distribution follows the SE

[2]materials which can support infinite stress at the crack tip

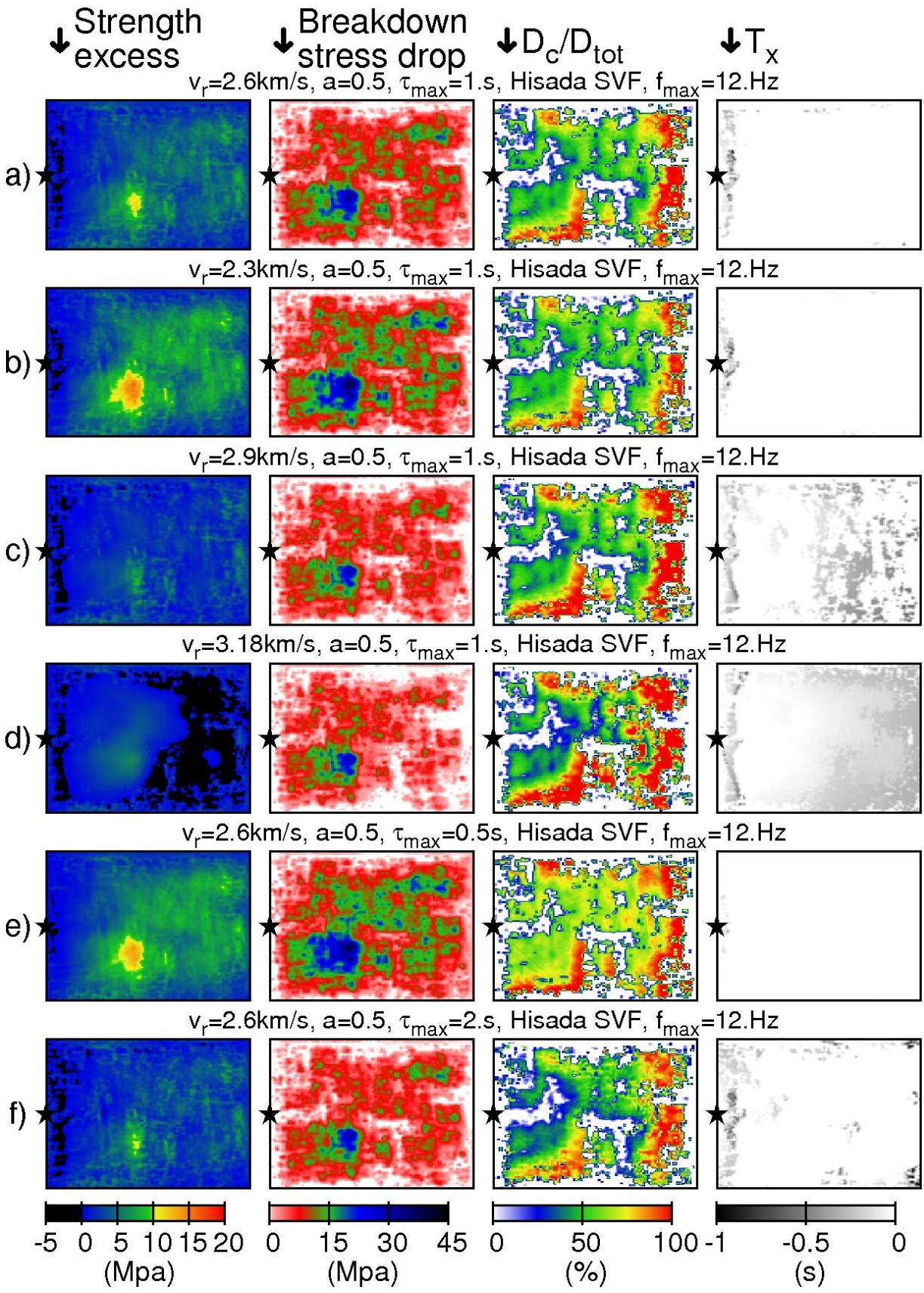
Strength excess
Breakdown stress drop
D_c/D_{tot}
T_x
v_r=2.6km/s, a=0.5, τ_{max}=1.s, Hisada SVF, f_{max}=12.Hz
a)
v_r=2.3km/s, a=0.5, τ_{max}=1.s, Hisada SVF, f_{max}=12.Hz
b)
v_r=2.9km/s, a=0.5, τ_{max}=1.s, Hisada SVF, f_{max}=12.Hz
c)
v_r=3.18km/s, a=0.5, τ_{max}=1.s, Hisada SVF, f_{max}=12.Hz
d)
v_r=2.6km/s, a=0.5, τ_{max}=0.5s, Hisada SVF, f_{max}=12.Hz
e)
v_r=2.6km/s, a=0.5, τ_{max}=2.s, Hisada SVF, f_{max}=12.Hz
f)
-5 0 5 10 15 20
(Mpa)
0 15 30 45
(Mpa)
0 50 100
(%)
-1 -0.5 0
(s)

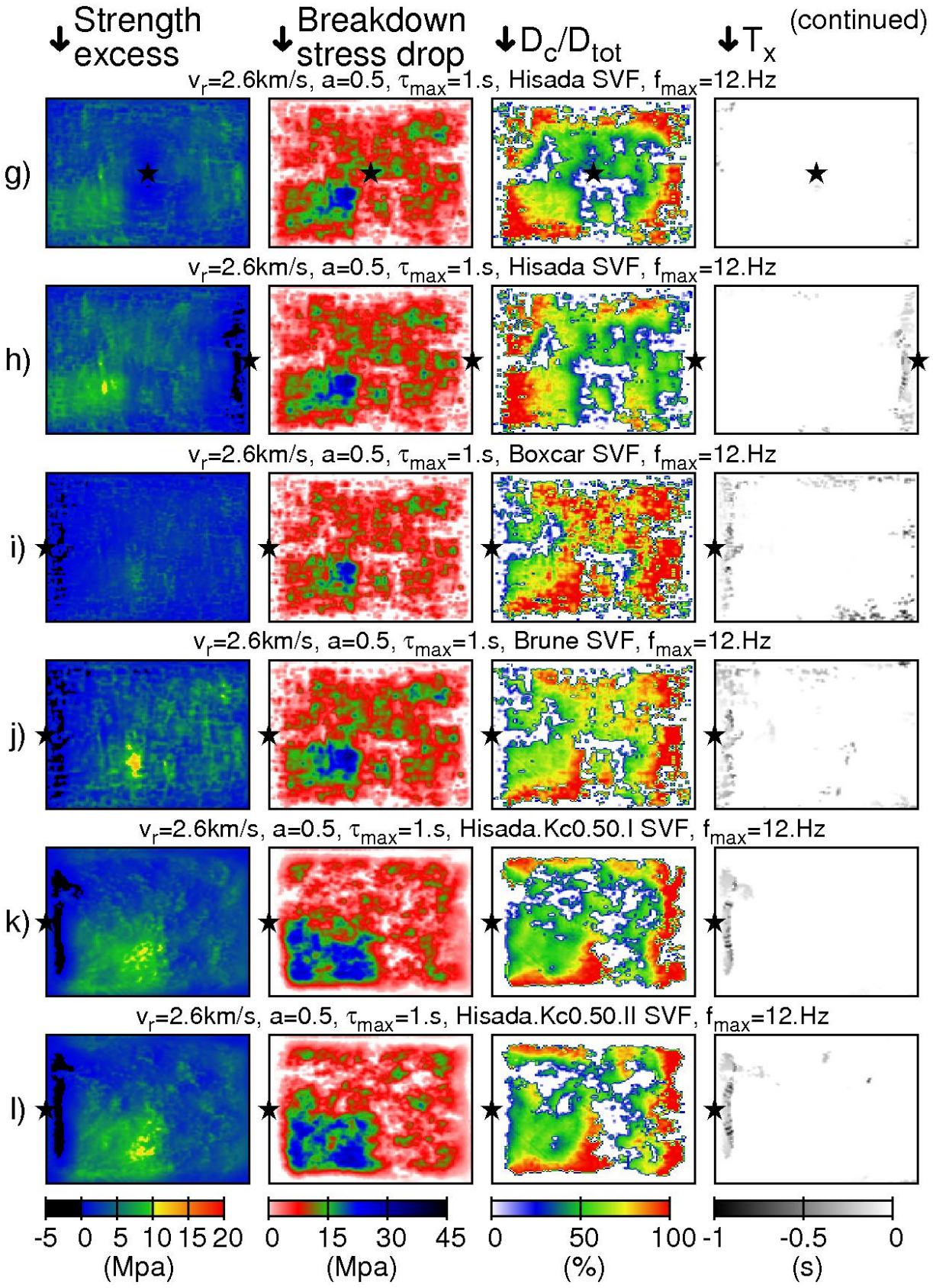
↓Strength excess
↓Breakdown stress drop
↓D_c/D_{tot}
↓T_x
(continued)
g) v_r=2.6km/s, a=0.5, τ_{max}=1.s, Hisada SVF, f_{max}=12.Hz
h) v_r=2.6km/s, a=0.5, τ_{max}=1.s, Hisada SVF, f_{max}=12.Hz
i) v_r=2.6km/s, a=0.5, τ_{max}=1.s, Boxcar SVF, f_{max}=12.Hz
j) v_r=2.6km/s, a=0.5, τ_{max}=1.s, Brune SVF, f_{max}=12.Hz
k) v_r=2.6km/s, a=0.5, τ_{max}=1.s, Hisada.Kc0.50.I SVF, f_{max}=12.Hz
l) v_r=2.6km/s, a=0.5, τ_{max}=1.s, Hisada.Kc0.50.II SVF, f_{max}=12.Hz
-5 0 5 10 15 20
(Mpa)
0 15 30 45
(Mpa)
0 50 100
(%)
-1 -0.5 0
(s)

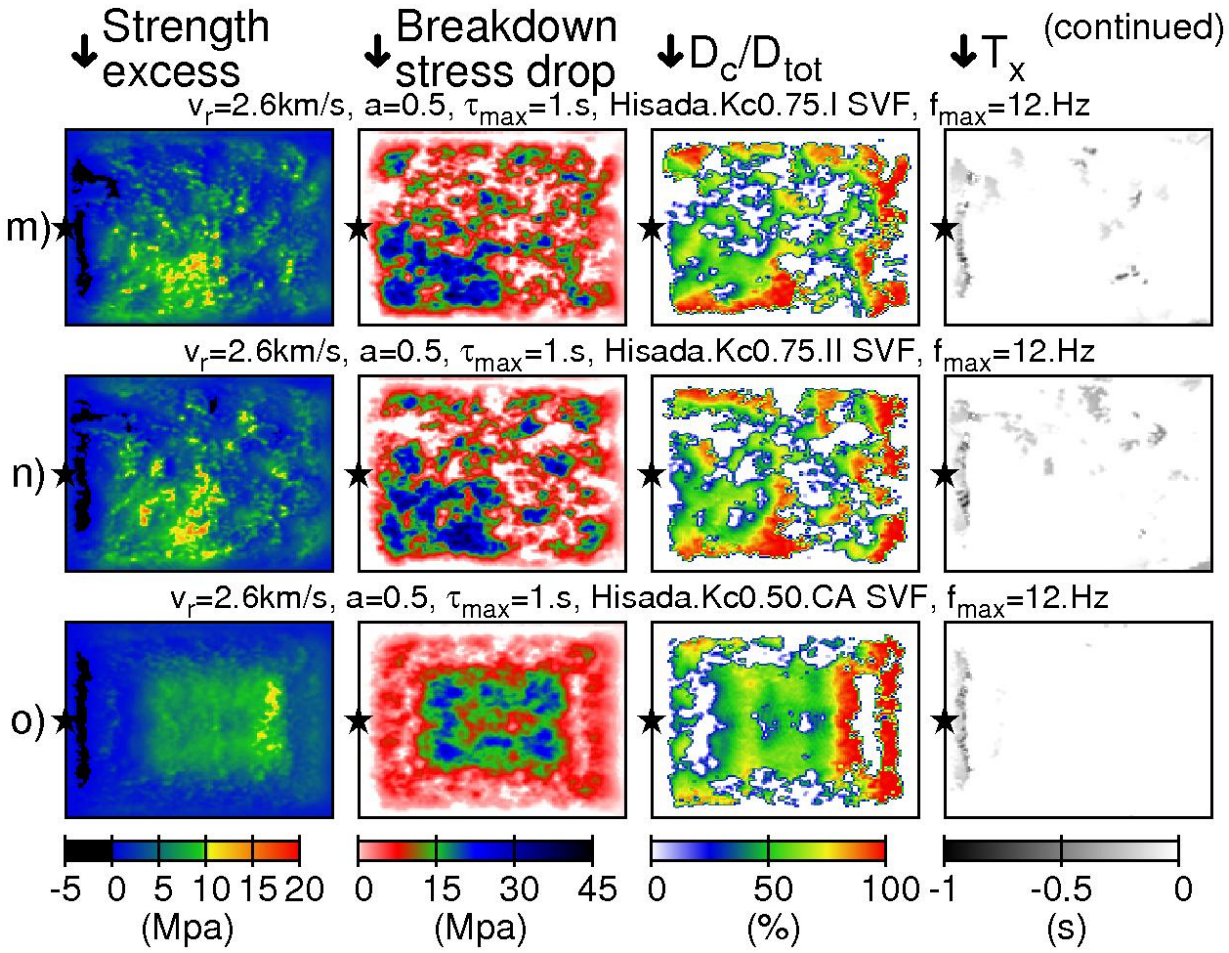

Figure 3.16: Strength excess, breakdown stress drop, D_c/D_{tot} (ratio of critical and total slip) distributions and stress delay T_x for 14 different sets of k-squared model input parameters. a) our reference model (Hisada's slip velocity function, nucleation point at left border of the fault, rupture velocity 2.6 km/s); b)-d) three different values of the rupture velocity (2.3km/s, 2.9km/s, 3.18km/s); e)-f) two different values of maximum rise time; g)-h) two different positions of the nucleation point (center, right border of the fault); i)-j) two different types of slip velocity functions (Brune, boxcar); k) a different k-squared slip distribution - v. slip distribution from Fig. 3.1A; l) a different stochastic realization of K_c=0.5 slip distribution - vi. slip distribution from Fig. 3.1A; m) a different k-squared slip distribution - iii. distribution from Fig. 3.1A; n) a different stochastic realization of K_c=0.75 slip distribution - iv. distribution from Fig. 3.1A; o) K_c=0.5 slip distribution with a different position of the asperity - viii. slip distribution from Fig. 3.1A.

reference solution (Fig. 3.16a). The negative SE values covering less than 5% of the fault area close to the nucleation point are present for all the tested v_r. When v_r reaches the Rayleigh velocity, negative SE values appear even outside the rupture nucleation region and cover about 30% of the fault. We found that the dynamic stress drop (DS) did not change with v_r, hence the breakdown stress drop (BS) follows the SE distribution, as BS=DS+SE (the average BS values decrease linearly from 8.9 MPa for $v_r = 2.3$ km/s to 5.4 MPa for $v_r = 3.18$ km/s). D_c/D_{tot} distribution does not change much with v_r. The T_x distribution depends on v_r. Non-zero T_x covers less than 5% of the fault area close to the nucleation point for $v_r = 2.3$ km/s, 2.6 km/s. T_x becomes non-zero outside the rupture nucleation region with v_r approaching the Rayleigh velocity (non-zero T_x at 21% and 67% of the fault area, for $v_r = 2.9$ km/s and $v_r = 3.18$ km/s respectively). Average fracture energy density values decrease almost linearly with v_r (from 1.5 MJ/m^2 for $v_r = 2.3$ km/s to 0.9 MJ/m^2 for $v_r = 3.18$ km/s).

3.5.2 Maximum rise time

The rise time - time for the slip to reach the static value at a point - is the parameter which probably scales with the earthquake size, e.g., Somerville *et al.* (1999) presented the seismic moment dependence. However, such scalings may not be reliable because the rise times are not usually well constrained in the kinematic source inversions. Some authors propose the slip velocity to be bounded at about 4 m/s (Kanamori, 1994; and references therein). We tested two values of the maximum rise time - 0.5 s and 2 s, so the values of the slip velocity do not exceed 4 m/s. The results are depicted in Fig. 3.16e-f. SE increased with shorter rise time (5 MPa average SE for $\tau_{max} = 0.5$ s) and, vice versa, SE decreased with longer rise time (2.9 MPa average SE for $\tau_{max} = 2$ s)). The change in BS is not hidden just in SE as in the case of variable v_r. We obtained 9.3 MPa and 6.1 MPa average BS for shorter and longer τ_{max}, respectively. Also there is a clear dependence of D_c/D_{tot} on τ_{max}: the longer τ_{max}, the smaller D_c/D_{tot}. Also, the non-zero T_x area (10% of the fault area) is larger for longer τ_{max}. Average fracture energy density values decrease with τ_{max} (from 1.9 MJ/m^2 for $\tau_{max} = 0.5$ s to 1.0 MJ/m^2 for $\tau_{max} = 2$ s).

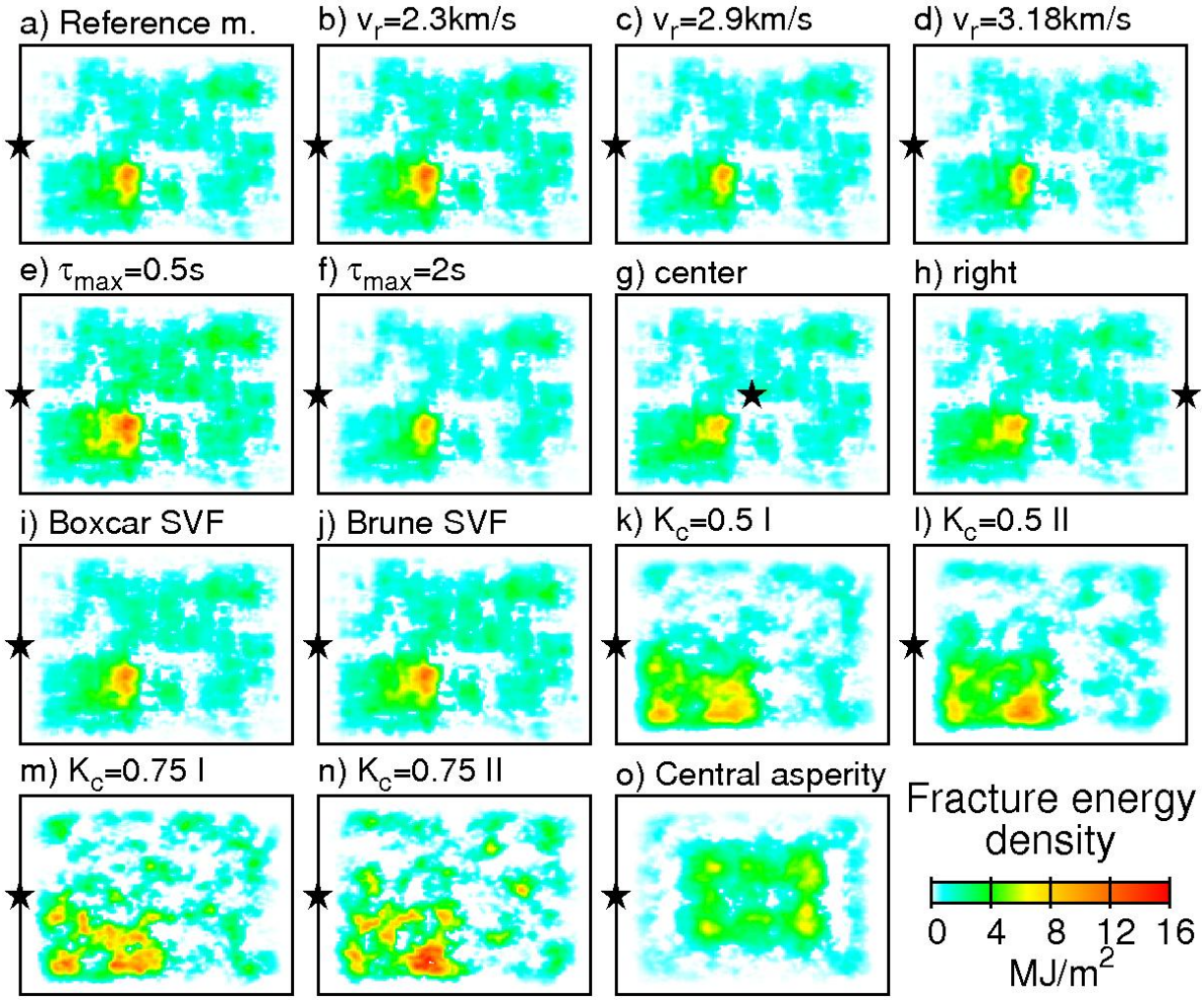

Figure 3.17: Fracture energy density estimation for the 14 models presented in Fig. 3.16.

3.5.3 Nucleation point position

We performed the calculations also for another two positions of the nucleation point (in the center and on the right border of the fault), which are, together with the reference solution, three basic representative models from the rupture directivity point of view. The change in the position of the nucleation point (Fig. 3.16g-h) leads to clear changes in the spatial patterns of the SE, BD, D_c/D_{tot} and T_x distributions. However, the average values of both SE and BS are very close to the reference solution (average SE=3.8 MPa, 3.6 MPa, 3.8 MPa and average BS=7.4 MPa, 7 MPa, 7.5 MPa, for a rupture starting from the left

a)

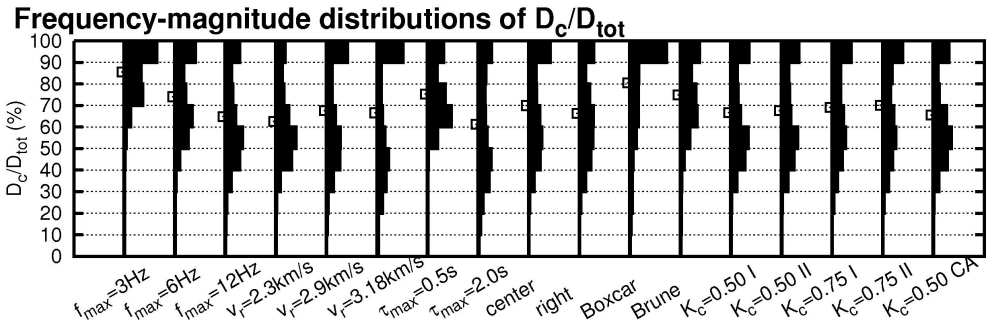

b)

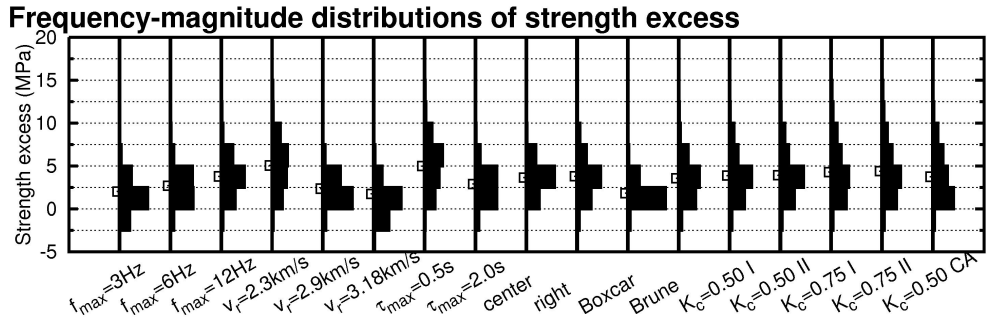

c)

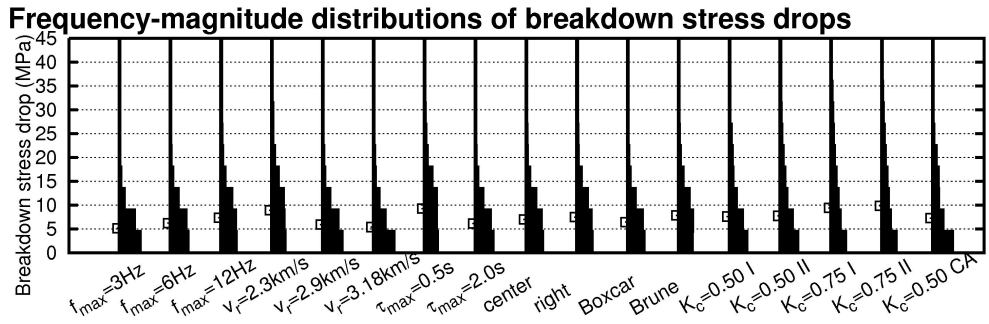

d)

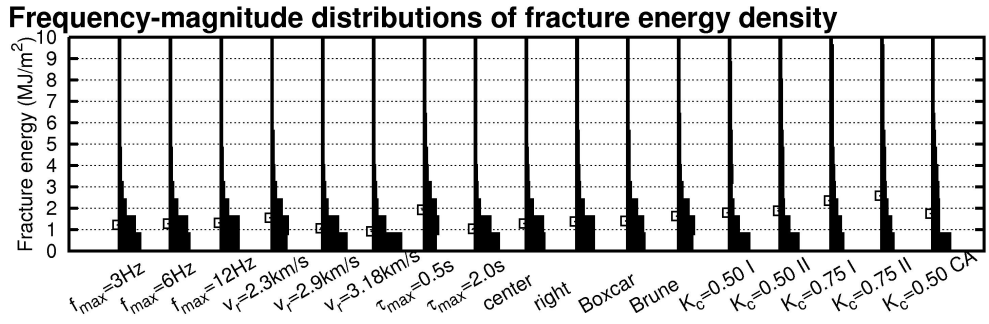

Figure 3.18: Frequency-magnitude distributions of a) D_c/D_{tot}, b) strength excess, c) breakdown stress drop and d) fracture energy density at all points along the fault for three filter cutoff frequencies ($f_{max} = 3Hz$, $f_{max} = 6Hz$, $f_{max} = 12Hz$) and for 14 models of the parametric study in the order presented in Fig. 3.16. $f_{max} = 12Hz$ is the reference solution in the parametric study. The empty square bullets indicate arithmetic mean values.

border, center and right border of the fault, respectively). T_x is zero almost for the whole fault (less than 1% of the fault area) in case of the rupture nucleating from the center of the fault and non-zero along less than 5% of the fault for the other two nucleation points. Also the change in the fracture energy density was less than 5%.

3.5.4 Slip velocity function shape

Further, we tested boxcar and Brune's slip velocity functions (Fig. 3.16i-j), which were previously used in strong motion modelling studies concerning k-squared model with the k-dependent rise time (e.g., Gallovič & Brokešová, 2004b). The SE (1.8 MPa average), BS (6.4 MPa average) and T_x distributions for the boxcar SVF resemble the results for $\tau_{max} = 2$ s (see Fig. 3.16f), which can be explained by a shorter "efficient" duration of Hisada's SVF (e.g., Fig. 6 in Gallovic & Brokesova, 2004a). The distributions of SE (3.6 MPa average) and BS (7.8 MPa average) in the case of Brune's SVF are close to the results for Hisada's SVF. Non-zero T_x covers less than 10% of the fault and appears even outside the rupture nucleation region. The D_c/D_{tot} values tend to 1 over most of the fault in the case of the boxcar SVF. The D_c/D_{tot} values are also higher for Brune's SVF than for Hisada's SVF. Average fracture energy density values were 1.4 MJ/m^2 for the boxcar SVF and 1.6 MJ/m^2 for Brune's SVF.

3.5.5 Static slip distribution

Finally, we performed the analysis for other static slip distributions (Fig. 3.16k-o), particularly for the both $K_c = 0.5$ and $K_c = 0.75$ slip distributions from Fig. 3.1A, two different stochastic distributions of these two and a different position of the asperity. The average SE (3.9, 3.9 MPa) and BS (7.6, 7.7 MPa) values are very close to the reference solution (3.8 MPa and 7.4 MPa, respectively) for the two stochastic realizations of $K_c = 0.5$ slip distribution. However, the spatial patterns of the SE and BS distributions differ in details from the reference solution. The differences are mainly due to the differences in the static stress change distributions (see Fig. 3.1B). The D_c/D_{tot} and T_x (non-zero along less than 5% of the fault) distributions are close to the reference solution. Average fracture energy

density values (1.8 MJ/m^2, 1.9 MJ/m^2) are higher than the reference solution. The average SE (4.3, 4.4 MPa) and BS (9.4, 9.8 MPa) values are higher for the two stochastic realizations of $K_c = 0.75$ slip distribution. Non-zero T_x covers less than 10% of the fault and appears even outside the rupture nucleation region. The frequency-magnitude distribution of D_c/D_{tot} is similar to the reference solution, however, as the areas of negative stress drop are larger and static stress change is more complicated (Fig. 3.1b) the D_c/D_{tot} spatial distribution is also more complicated. Zero BS area also increases considerably with $K_c = 0.75$. Average fracture energy density values (2.3 MJ/m^2, 2.6 MJ/m^2) are higher than the reference solution. The average SE (3.8 MPa) and BS (7.3 MPa) values are very close to the reference solution for the different position of the asperity. The spatial patterns of the SE and BS distributions differ from the reference solution, it follows the static stress change distribution. The D_c/D_{tot} and T_x (non-zero along less than 5% of the fault) distributions are also close to the reference solution. Average fracture energy density value (1.7 MJ/m^2) is similar to the reference solution.

We emphasize that the results do not depend on a single stochastic realization, except for the changing of the pattern of small scale features, and surprisingly, for the values of fracture energy, which seem to be sensitive to the peak slip values (10% change in average fracture energy density for $K_c = 0.75$ slip distributions). Such result might be quite troublesome, as in the literature, fracture energy is supposed to be a robust parameter, well constrained for a number of earthquakes. However, it can be understood. Fracture energy density values scale with the power two of local slip value (Fig. 3.15). Hence, average fracture energy density might be quite strongly affected by local very high fracture energy values coming from even small high slip patches. The spatial patterns of the results depend mostly on the position of the asperity. Even in the case of rougher fault ($K_c = 0.75$), shifting more power to higher wavenumbers, the influence of asperity is still present - the band of negative stress drops enclosing the asperity. The D_c/D_{tot} frequency-magnitude distributions also change very little with the different slip distributions.

3.6 Discussion of the results for the k-squared model

The purpose of this chapter was to investigate both the static and dynamic stress change due to a theoretical kinematic source model: the k-squared source model with asperities. We found that the stress field of the k-squared slip distribution and the slip velocity function with k-dependent rise time is free of singularities[3]. Let us compare the results with the findings of Madariaga (1978), who studied Haskell's fault model. Contrary to Haskell's model with an infinite average static stress drop, the k-squared model has a finite average static stress drop since the slip vanishes smoothly at the border of the fault, so that the static stress change is bounded. Further, the k-squared model with k-dependent rise time generates stress time histories which are also bounded as the slip velocity functions have finite rise times. On the other hand, stress time histories generated by Haskell's model with instantaneous slip contain singularities associated with S-wave and rupture front arrivals. Thus, the k-squared model with k-dependent rise time is not in such clear contradiction to earthquake source dynamics as Haskell's model.

A detailed analysis was carried out to compare the stress state along the fault with the constitutive relations used in earthquake source dynamics. Attention was paid to the stress recovery associated with the slip pulse, the slip pulse being an ingredient of the k-squared model with k-dependent rise time. We found the stress recovery to be close to the nucleation point for narrow pulses ($L_0 < L/5$). We point out that the amount of stress recovery depends on the rupture velocity and rise time, i.e., on the pulse width. Further, we determined the strength excess, breakdown stress drop and dynamic stress drop distributions. We found that it was also possible to fit stress slip curves to a simple linear slip weakening law, obtaining D_c with high variance reduction ($\sim 90\%$) in the positive static stress drop areas. Stress delay T_x, a parameter introduced in this work, agrees with the yielding criteria of the simple slip weakening friction law (characterized only by yield stress, dynamic stress and critical slip weakening distance D_c).

[3]Strictly speaking, there is a possible stress singularity *just* at the nucleation point, whose existence depends on details of the space-time slip distribution close to a rupture initiation (both in space and time).

The stress time histories due to the k-squared model are very similar to the stress time histories due to the kinematic models of real earthquakes (see Figures 4 and 5 in Day *et al.*, 1998). The values of the strength excess and dynamic stress drop are in tenths of MPa as for real earthquakes as found, e.g., by Bouchon (1997), Piatanesi *et al.* (2004). The average value of D_c/D_{tot} in the positive stress drop area is 0.65 ± 0.05 (except for the cases of Brune's SVF, boxcar SVF and $\tau_{max} = 0.5$ s) which is similar to the value 0.63 found by Zhang *et al.* (2003) for the 1999 Chi-Chi earthquake. The D_c/D_{tot} frequency-magnitude distributions present two maxima. One maximum lays around 50% and the other at 100%. $D_c \simeq D_{tot}$ is found at the edges of the both asperity and fault.

The parametric study helped us to reject or adopt some values of the free parameters of the k-squared model, taking into account the simple slip weakening friction law. Particularly, rupture velocities close to the Rayleigh velocity v^R lead to a worse linear slip weakening fit (65% variance reduction for $v_r = v^R$) and large areas of both negative strength excess and non-zero T_x. Thus we conclude that rupture velocities $0.9\,v^R$ to v^R are not suitable for the k-squared model with k-dependent rise time. Super shear rupture velocities were not studied in this thesis. The constant rupture velocity in the k-squared model seems to be the most problematic constraint. The phenomenon of constant rupture velocity is not present even in simple forward dynamic problems of spontaneous rupture propagation. However, a constant rupture velocity can be modeled by heterogeneous frictional parameters (e.g., by the strength excess and breakdown stress drop distributions obtained in our study). Nevertheless, a constant rupture velocity is very unlikely, and the k-squared model should be refined in this sense to become more realistic.

Non-zero T_x vanishes with short maximum rise time ($\tau_{max} = 0.5$ s), however, stress recovery after a pulse passage increases and D_c becomes closer to D_{tot}. On the other hand, longer rise time ($\tau_{max} = 2$ s) leads to lower D_c, negligible stress recovery, but to larger areas of non-zero T_x. Thus we conclude that the maximum rise time $\tau_{max} = 1$ s is optimal for our fault dimensions and elastic parameters. It is necessary to extend the parametric study to generalize this conclusion. Mai *et al.* (2005) found more probable ruptures nucleating from regions close to asperities and not from zero slip areas. Our results partially agree

with these findings. The nucleation point in the center of the fault (non-zero slip, asperity border) leads to smallest non-zero T_x area, however, areas of non-zero T_x cover less than 5% of the fault for the two other positions of nucleation points (fault border - zero slip). Thus, we do not prefer any position of the studied nucleation points. The area of non-zero T_x is smallest for Hisada's slip velocity function. Also D_c is shortest for Hisada's SVF. Hence, employing Hisada's SVF is more consistent with applications of the slip weakening law in earthquake source dynamics than boxcar, Brune's and Dirac's SVF. We attribute it to its similarity with the Kostrov function, which is an analytical solution of the forward dynamic problem. We conclude that nine k-squared models with dynamic parameters plotted in Fig. 3.16(a, b, g, h, k-o) can be explained by a dynamic model with the slip weakening friction law. However, this should be proved with forward dynamic simulations in the future. The parametric study should be also extended in the future to cover various fault sizes, multiple asperities and different rake values.

We also analyzed the effect of filtering on the dynamic stress field of a kinematic source model in both the space and time domains. Low-pass frequency filtering decreases the values of the strength excess and increases the values of both D_c and stress delay T_x, while the low-pass wavenumber filtering decreases the values of the fracture energy. We point out the effect of spatial filtering influences the results considerably but has not yet been studied sufficiently. The limited spatial resolution of kinematic source inversions could smear numerous negative stress drop heterogeneities within the fault. These could play an important role in forward dynamical simulations, since they act as barriers for the rupture.

Chapter 4

Conclusions and Outlook

The main outcome of this work is the new approach for evaluation of synthetic kinematic models from the viewpoint of the earthquake dynamics. It resulted in a (thoroughly proved) finding that the k-squared slip model with k-dependent rise time (shortly k-squared model) is basically not in contradiction to earthquake source dynamics. The k-squared model was studied in terms of the slip weakening friction law - strength excess, dynamic stress drop, breakdown stress drop, critical slip weakening distance D_c, fracture energy. Another outreach of the work is the impact on the strong motion prediction. Indeed, a class of k-squared models which are most consistent with the slip weakening friction law (Hisada's slip velocity function) was found. On the other hand, the models which violate the slip weakening friction law considerably (rupture velocity close to Rayleigh speed) were found too. Thus the analysis provided constraints on the k-squared models to be used in practice.

Further, the work contributes to general methodology of fault constitutive relations estimations. A new parameter, the stress delay T_x, was introduced to map the fault points where the peak stress precedes the rupture onset. A simple but original D_c estimation method directly from the stress-slip curves was also presented. The effect of spatial filtering was shown on various dynamic source parameters. The bimodal character of D_c/D_{tot} frequency-magnitude distribution was found and discussed, but it remains for future study, whether the same holds for kinematic models of real earthquakes.

The discrete wavenumber code (parallelized with *OpenMP* directives) for dynamic stress calculations, developed in this thesis, can be utilized for a broader set of problems. It has

been already applied in the work of Fischer & Horálek (2005) who studied dynamic stress triggering of earthquakes during Western Bohemia seismic swarms. It could be also used for tuning other, more general, numerical methods. The method of the calculation could be easily extended to more general geometries, as the fundamentals of discrete wavenumber method are presented in detail in the appendix of this thesis. For example, the dynamic stress calculation could be in the future extended to account also for the presence of free surface (homogeneous half-space).

Appendix A

Discrete Wavenumber Method

In this appendix, we explain the discrete wave number (DW) method in detail. Specifically, DW method for evaluation of the stress change due to a dislocation on a planar fault. Although, a number of papers exist on the general theme of DW (e.g., review paper by Bouchon, 2003; and references therein), these contain only fragments of the derivations. We point out, that results in this part are not original (except slight generalizations, mentioned in the text), but provide a complete derivation. Let us define Fourier transforms of functions of position $f(x,y,z)$ and time $g(t)$ as

$$\hat{f}(k_x,k_y,k_z) = \int_{-\infty}^{\infty}\int_{-\infty}^{\infty}\int_{-\infty}^{\infty} f(x,y,z)\exp(ik_x x + ik_y y + ik_z z)\,dx\,dy\,dz, \tag{A.1}$$

$$g(\omega) = \int_{-\infty}^{\infty} g(t)\exp(-i\omega t)\,dt \tag{A.2}$$

respectively and correspondent inverse Fourier transforms

$$f(x,y,z) = \frac{1}{8\pi^3}\int_{-\infty}^{\infty}\int_{-\infty}^{\infty}\int_{-\infty}^{\infty} \hat{f}(k_x,k_y,k_z)\exp(-ik_x x - ik_y y - ik_z z)\,dk_x\,dk_y\,dk_z, \tag{A.3}$$

$$g(t) = \frac{1}{2\pi}\int_{-\infty}^{\infty} g(\omega)\exp(i\omega t)\,d\omega \tag{A.4}$$

where k_x, k_y, k_z denote wavenumbers, ω denotes angular frequency. Consider a displacement field $\boldsymbol{u} = \boldsymbol{u}(x,y,z,t)$ satisfying the equation of motion and Hooke's law in a homogeneous, unbounded, isotropic, elastic medium

$$\rho\ddot{\boldsymbol{u}} = \boldsymbol{f} + \nabla\cdot\boldsymbol{\tau} \tag{A.5}$$

$$\boldsymbol{\tau} = \lambda\nabla\cdot\boldsymbol{u}\,\mathbf{I} + \mu\left[\nabla\boldsymbol{u} + (\nabla\boldsymbol{u})^{\mathrm{T}}\right] \tag{A.6}$$

where ρ is the density, $\boldsymbol{f} = \boldsymbol{f}(x, y, z, t)$ is the body force, $\boldsymbol{\tau}$ is stress tensor, $\mathbf{I}$ is the identity matrix, μ and λ are the Lamé coefficients. If the body force a and initial values of $\dot{\boldsymbol{u}}$ and $\boldsymbol{u}$ are expressed in terms of Helmholtz potentials $A, \boldsymbol{B}, C, \boldsymbol{D}, E, \boldsymbol{F}$ so that

$$\boldsymbol{f} = \nabla A + \nabla \times \boldsymbol{B}, \quad \nabla \cdot \boldsymbol{B} = 0, \tag{A.7}$$

$$\dot{\boldsymbol{u}} = \nabla C + \nabla \times \boldsymbol{D}, \quad \nabla \cdot \boldsymbol{D} = 0, \tag{A.8}$$

$$\boldsymbol{u} = \nabla E + \nabla \times \boldsymbol{F}, \quad \nabla \cdot \boldsymbol{F} = 0, \tag{A.9}$$

then Lamé's theorem (Aki & Richards, 1980) gives

$$\boldsymbol{u} = \nabla \phi + \nabla \times \boldsymbol{\psi} \tag{A.10}$$

$$0 = \nabla \cdot \boldsymbol{\psi} \tag{A.11}$$

$$\ddot{\phi} = \frac{A}{\rho} + v_P^2 \Delta \phi, \quad v_P = \sqrt{\frac{\lambda + 2\mu}{\rho}} \tag{A.12}$$

$$\ddot{\boldsymbol{\psi}} = \frac{\boldsymbol{B}}{\rho} + v_S^2 \Delta \boldsymbol{\psi}, \quad v_S = \sqrt{\frac{\mu}{\rho}} \tag{A.13}$$

where v_P is the P-wave velocity, v_S is the S-wave velocity, ϕ and $\boldsymbol{\psi}$ are the Lamé potentials. Thus the equation of motion (three partial differential equations) broke to a wave equation (A.12) plus three wave equations (A.13) coupled with an equation (A.11). The Helmholtz potentials $A, \boldsymbol{B}$ for the body force $\boldsymbol{f}$ can be found solving the vector Poisson equation for an auxiliary function $\boldsymbol{W}$ (Aki & Richards, 1980)

$$\Delta \boldsymbol{W} = \boldsymbol{f} \tag{A.14}$$

then

$$A = \nabla \cdot \boldsymbol{W}, \tag{A.15}$$

$$\boldsymbol{B} = -\nabla \times \boldsymbol{W}. \tag{A.16}$$

A.1 A solution for a point force

Firstly, let us find the Lamé potentials for a unit point force at origin. Later, we will derive potentials for a dislocation source from the point force solution. The answer to the point

force problem is well known Stoke's solution, however, we want it as a superposition of plane waves. Such solution was found by Bouchon (1979). Here, we present a different way of derivation. The first step is to find spectra of the body force potentials $\hat{A}, \hat{\boldsymbol{B}}$ for a point source

$$\boldsymbol{f} = \exp(-i\omega t)\delta(x, y, z)\,\boldsymbol{e}^z \tag{A.17}$$

where $\delta(x, y, z)$ is the Dirac delta function, $\boldsymbol{e}^z$ is a direction of z-axis. Putting (A.17) into (A.14) and applying the Fourier transform (A.1) yields

$$\hat{W}_x = \hat{W}_y = 0, \quad \hat{W}_z(k_x, k_y, k_z, t) = \frac{\exp(-i\omega t)}{-|\boldsymbol{k}|^2}. \tag{A.18}$$

Then from (A.15) and (A.16)

$$\hat{A} = \frac{ik_z \exp(-i\omega t)}{|\boldsymbol{k}|^2}, \tag{A.19}$$

$$\hat{B}_x = \frac{ik_y \exp(-i\omega t)}{|\boldsymbol{k}|^2}, \quad \hat{B}_y = \frac{ik_x \exp(-i\omega t)}{-|\boldsymbol{k}|^2}, \quad \hat{B}_z = 0. \tag{A.20}$$

Applying the Fourier transforms (A.1) and (A.2) to (A.12) together with substitution from (A.19) we obtain harmonic solution

$$\hat{\phi}^z(k_x, k_y, k_z, \omega)\exp(i\omega t) = \frac{ik_z \exp(i\omega t)}{\rho|\boldsymbol{k}|^2\left(v_P^2|\boldsymbol{k}|^2 - \omega^2\right)}. \tag{A.21}$$

So the scalar Lamé potential for a unit point force applied at origin in the directions $\boldsymbol{e}^z$ is

$$\phi^z(x, y, z, t) = \frac{\exp(i\omega t)}{8\pi^3}\int_{-\infty}^{\infty}\int_{-\infty}^{\infty}\int_{-\infty}^{\infty}\frac{ik_z \exp(-ik_x x - ik_y y - ik_z z)}{\rho v_P^2|\boldsymbol{k}|^2\left(|\boldsymbol{k}|^2 - \frac{\omega^2}{v_P^2}\right)}\,dk_x\,dk_y\,dk_z. \tag{A.22}$$

ϕ^z is expressed in form of superpositions of planes waves. However, these plane waves have arbitrary velocities. It is necessary to perform an integration over a wavenumber to get the superposition of the plane waves which propagate in the medium with a given velocity v_P. We choose to integrate over k_z without loss of generality. We apply residue theory to evaluate the integral

$$I(\omega, k_x, k_y, z) = \int_{-\infty}^{\infty}\frac{k_z \exp(-ik_z z)}{\left(k_x^2 + k_y^2 + k_z^2\right)\left(k_x^2 + k_y^2 + k_z^2 - \frac{\omega^2}{v_P^2}\right)}\,dk_z. \tag{A.23}$$

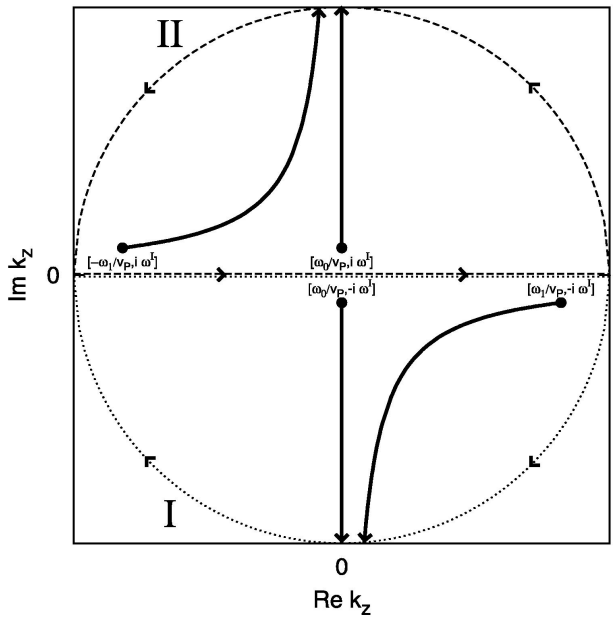

Figure A.1: Poles location and integration paths in the complex k_z-plane for two frequencies (ω_0,ω_1) and a small value of the artificial attenuation transcribed to an imaginary part ω^I of frequency. Short dashed curve (I) denote integration path in lower half-plane around -ν pole and long dashed curve (II) denote integration path in upper half-plane around ν pole.

Let us extend k_z to complex values and assume $k_x \neq 0 \wedge k_y \neq 0$, then the integrand in (A.23) has poles at $k_z = \pm\nu$, where

$$\nu = \sqrt{\frac{\omega^2}{v_P^2} - k_x^2 - k_y^2}, \quad \mathrm{Im}\,\nu < 0. \tag{A.24}$$

Consider integration paths depicted in Fig. A.1. The poles interfere with the integration paths for $k_x^2 + k_y^2 < \omega^2/v_P^2$. Hence, a small artificial attenuation is introduced by making $1/v_P$ complex and the poles are shifted into fourth and second quadrant for ν and $-\nu$ respectively, see Fig. A.1. Then for $z > 0$ we choose integration path (I), and (A.23) yields

$$I\left(\omega, k_x \neq 0 \wedge k_y \neq 0, z > 0\right) = -2\pi i Res_- = -\pi i \frac{v_P^2 \exp\left(-i\nu z\right)}{\omega^2} \tag{A.25}$$

where Res_- is the residue in lower k_z half-plane, thus for a pole $k_z = \nu$. Similarly, for $z < 0$ we choose integration path (II), and (A.23) yields

$$I\left(\omega, k_x \neq 0 \wedge k_y \neq 0, z < 0\right) = 2\pi i Res_+ = \pi i \frac{v_P^2 \exp\left(i\nu z\right)}{\omega^2} \tag{A.26}$$

where Res_+ is the residue in upper k_z half-plane, thus for a pole $k_z = -\nu$. Combining results (A.25) and (A.26), we obtain

$$I\left(\omega, k_x \neq 0 \wedge k_y \neq 0, z\right) = -\mathrm{sgn}\left(z\right)\pi i \frac{v_P^2 \exp\left(-i\nu\left|z\right|\right)}{\omega^2}. \tag{A.27}$$

Now, let us assume $k_x = k_y = 0$, so

$$I\left(\omega, k_x = 0, k_y = 0, z\right) = \int_{-\infty}^{\infty} \frac{\exp\left(-ik_z z\right)}{k_z\left(k_z^2 - \frac{\omega^2}{v_P^2}\right)}\, dk_z \tag{A.28}$$

which can be rewritten as

$$I\left(\omega, k_x = 0, k_y = 0, z\right) = \frac{v_P^2}{\omega^2}\int_{-\infty}^{\infty} \frac{k_z \exp\left(-ik_z z\right)}{k_z^2 - \nu^2}\, dk_z - \frac{v_P^2}{\omega^2}\int_{-\infty}^{\infty} \frac{\exp\left(-ik_z z\right)}{k_z}\, dk_z. \tag{A.29}$$

The first integral can be evaluated in the same way as for the previous case ($k_x \neq 0 \wedge k_y \neq 0$) and we read the Fourier transform of $\mathrm{sgn}(z)$ function in the integrand of the second integral, so that

$$I\left(\omega, k_x = 0, k_y = 0, z\right) = -\mathrm{sgn}\left(z\right)\pi i \frac{v_P^2 \exp\left(-i\nu\left|z\right|\right)}{\omega^2} + \mathrm{sgn}\left(z\right)\pi i \frac{v_P^2}{\omega^2}. \tag{A.30}$$

The first term in (A.30) is identical to (A.27). The second term appears only if $k_x = k_y = 0$ and as it is bounded. An equation

$$\int_{-\infty}^{\infty}\int_{-\infty}^{\infty} I\left(\omega, k_x, k_y, z\right)\, dk_x\, dk_y = -\int_{-\infty}^{\infty}\int_{-\infty}^{\infty} \mathrm{sgn}\left(z\right)\pi i \frac{v_P^2 \exp\left(-i\nu\left|z\right|\right)}{\omega^2}\, dk_x\, dk_y \tag{A.31}$$

holds in sense of L_2 norm and (A.22) becomes

$$\phi^z\left(x, y, z, t\right) = \frac{\mathrm{sgn}\left(z\right)}{8\pi^2\rho\omega^2}\int_{-\infty}^{\infty}\int_{-\infty}^{\infty} \exp\left(i\omega t - ik_x x - ik_y y - i\nu\left|z\right|\right) dk_x\, dk_y. \tag{A.32}$$

Note the $\phi^z\left(x, y, z, t\right)$ is now expressed as a superposition of plane waves with v_P phase velocity, in other words, these plane waves satisfy wave equation (A.12) for $A = 0$. Hereafter, we omit the time factor $\exp\left(i\omega t\right)$ for a brevity. Analogically, we could obtain similar expansions for $\psi_x^z, \psi_y^z, \psi_z^z$ and also for point forces pointing in $\boldsymbol{e}^x$ and $\boldsymbol{e}^y$ directions. Thus the Lamé potentials resulting from a unit point force applied at origin in the directions

$\boldsymbol{e}^x$,$\boldsymbol{e}^y$,$\boldsymbol{e}^z$ respectively are given by the expressions

$$\phi^x(x,y,z,\omega) = \frac{1}{8\pi^2\omega^2\rho}\int_{-\infty}^{\infty}\int_{-\infty}^{\infty}\frac{k_x}{\nu}\exp\left(-ik_x x - ik_y y - i\nu|z|\right)dk_x dk_y \tag{A.33}$$

$$\psi_x^x(x,y,z,\omega) = 0 \tag{A.34}$$

$$\psi_y^x(x,y,z,\omega) = \frac{-sgn(z)}{8\pi^2\omega^2\rho}\int_{-\infty}^{\infty}\int_{-\infty}^{\infty}\exp\left(-ik_x x - ik_y y - i\gamma|z|\right)dk_x dk_y \tag{A.35}$$

$$\psi_z^x(x,y,z,\omega) = \frac{1}{8\pi^2\omega^2\rho}\int_{-\infty}^{\infty}\int_{-\infty}^{\infty}\frac{k_y}{\gamma}\exp\left(-ik_x x - ik_y y - i\gamma|z|\right)dk_x dk_y \tag{A.36}$$

$$\phi^y(x,y,z,\omega) = \frac{1}{8\pi^2\omega^2\rho}\int_{-\infty}^{\infty}\int_{-\infty}^{\infty}\frac{k_y}{\nu}\exp\left(-ik_x x - ik_y y - i\nu|z|\right)dk_x dk_y \tag{A.37}$$

$$\psi_x^y(x,y,z,\omega) = \frac{sgn(z)}{8\pi^2\omega^2\rho}\int_{-\infty}^{\infty}\int_{-\infty}^{\infty}\exp\left(-ik_x x - ik_y y - i\gamma|z|\right)dk_x dk_y \tag{A.38}$$

$$\psi_y^y(x,y,z,\omega) = 0 \tag{A.39}$$

$$\psi_z^y(x,y,z,\omega) = \frac{-1}{8\pi^2\omega^2\rho}\int_{-\infty}^{\infty}\int_{-\infty}^{\infty}\frac{k_x}{\gamma}\exp\left(-ik_x x - ik_y y - i\gamma|z|\right)dk_x dk_y \tag{A.40}$$

$$\phi^z(x,y,z,\omega) = \frac{sgn(z)}{8\pi^2\omega^2\rho}\int_{-\infty}^{\infty}\int_{-\infty}^{\infty}\exp\left(-ik_x x - ik_y y - i\nu|z|\right)dk_x dk_y \tag{A.41}$$

$$\psi_x^z(x,y,z,\omega) = \frac{-1}{8\pi^2\omega^2\rho}\int_{-\infty}^{\infty}\int_{-\infty}^{\infty}\frac{k_y}{\gamma}\exp\left(-ik_x x - ik_y y - i\gamma|z|\right)dk_x dk_y \tag{A.42}$$

$$\psi_y^z(x,y,z,\omega) = \frac{1}{8\pi^2\omega^2\rho}\int_{-\infty}^{\infty}\int_{-\infty}^{\infty}\frac{k_x}{\gamma}\exp\left(-ik_x x - ik_y y - i\gamma|z|\right)dk_x dk_y \tag{A.43}$$

$$\psi_z^z(x,y,z,\omega) = 0 \tag{A.44}$$

where

$$\gamma = \sqrt{\frac{\omega^2}{v_S^2} - k_x^2 - k_y^2}, \quad \mathrm{Im}\,\gamma < 0. \tag{A.45}$$

Discretized expressions (A.33-A.44) were presented in Bouchon (1979).

A.2 A solution for a plane dislocation

Let us move to the dislocation source. Aki & Richards (1980) gives a representation of the displacement field by displacement discontinuity along the surface and elastodynamic

Green's tensor (a displacement point force response). Such representation theorem can be also formulated for the Lamé potentials, so that for a dislocation $\Delta\boldsymbol{u}(x', y', \omega)$ acting on a fault plane $\Sigma : z' = 0$ we get

$$\phi(x, y, z, \omega) = \int_{\Sigma} m_{\alpha\beta}(x', y', \omega) \frac{\partial \phi^{\alpha}(x - x', y - y', z - z', \omega)}{\partial \beta'} d\Sigma' \tag{A.46}$$

$$\psi_x(x, y, z, \omega) = \int_{\Sigma} m_{\alpha\beta}(x', y', \omega) \frac{\partial \psi_x^{\alpha}(x - x', y - y', z - z', \omega)}{\partial \beta'} d\Sigma' \tag{A.47}$$

$$\psi_y(x, y, z, \omega) = \int_{\Sigma} m_{\alpha\beta}(x', y', \omega) \frac{\partial \psi_y^{\alpha}(x - x', y - y', z - z', \omega)}{\partial \beta'} d\Sigma' \tag{A.48}$$

$$\psi_z(x, y, z, \omega) = \int_{\Sigma} m_{\alpha\beta}(x', y', \omega) \frac{\partial \psi_z^{\alpha}(x - x', y - y', z - z', \omega)}{\partial \beta'} d\Sigma' \tag{A.49}$$

with the so-called moment tensor density spectra

$$m_{\alpha\beta}(x', y', \omega) = \lambda \Delta u_z \delta_{\alpha\beta} + \mu \left(\Delta u_{\alpha} \delta_{\beta 3} + \Delta u_{\beta} \delta_{\alpha 3}\right), \tag{A.50}$$

where we sum over α and β, which take one of symbols x, y, z. Combining relations (A.33-A.44) with relations (A.46-A.50) yields

$$\begin{aligned}\phi(x, y, z, \omega) =& \frac{i}{8\pi^2\omega^2\rho} \int_{\Sigma} \int_{-\infty}^{\infty} \int_{-\infty}^{\infty} \Big\{ \mu \left[2 \operatorname{sgn}(z) k_x \Delta u_x + 2 \operatorname{sgn}(z) k_y \Delta u_y + 2\nu \Delta u_z\right] + \\ & \lambda \frac{\omega^2}{\alpha^2 \nu} \Delta u_z \Big\} \exp\left[-ik_x (x - x') - ik_y (y - y') - i\nu |z|\right] dk_x dk_y d\Sigma' \end{aligned} \tag{A.51}$$

$$\begin{aligned}\psi_x(x, y, z, \omega) =& \frac{i}{8\pi^2\omega^2\rho} \int_{\Sigma} \int_{-\infty}^{\infty} \int_{-\infty}^{\infty} \mu \left[- \frac{k_x k_y}{\gamma} \Delta u_x + \left(\gamma - \frac{k_y^2}{\gamma}\right) \Delta u_y - 2 \operatorname{sgn}(z) k_y \Delta u_z \right] \\ & \exp\left[-ik_x (x - x') - ik_y (y - y') - i\gamma |z|\right] dk_x dk_y d\Sigma' \end{aligned} \tag{A.52}$$

$$\begin{aligned}\psi_y(x, y, z, \omega) =& \frac{i}{8\pi^2\omega^2\rho} \int_{\Sigma} \int_{-\infty}^{\infty} \int_{-\infty}^{\infty} \mu \left[\left(\frac{k_x^2}{\gamma} - \gamma\right) \Delta u_x + \frac{k_x k_y}{\gamma} \Delta u_y + 2 \operatorname{sgn}(z) k_x \Delta u_z \right] \\ & \exp\left[-ik_x (x - x') - ik_y (y - y') - i\gamma |z|\right] dk_x dk_y d\Sigma' \end{aligned} \tag{A.53}$$

$$\begin{aligned}\psi_z(x, y, z, \omega) =& \frac{i}{8\pi^2\omega^2\rho} \int_{\Sigma} \int_{-\infty}^{\infty} \int_{-\infty}^{\infty} \mu \left[\operatorname{sgn}(z) k_y \Delta u_x - \operatorname{sgn}(z) k_x \Delta u_y\right] \\ & \exp\left[-ik_x (x - x') - ik_y (y - y') - i\gamma |z|\right] dk_x dk_y d\Sigma'. \end{aligned} \tag{A.54}$$

We denote the integrands as $\tilde{\phi}$, $\tilde{\psi}_x$, $\tilde{\psi}_y$, $\tilde{\psi}_z$ respectively, then applying (A.10) results in expressions for displacement

$$\tilde{u}_x\left(k_x,k_y,x,y,z,\omega\right) = -ik_x\tilde{\phi} - ik_y\tilde{\psi}_z + i\,\mathrm{sgn}\left(z\right)\gamma\tilde{\psi}_y \tag{A.55}$$

$$\tilde{u}_y\left(k_x,k_y,x,y,z,\omega\right) = -ik_y\tilde{\phi} - i\,\mathrm{sgn}\left(z\right)\gamma\tilde{\psi}_x + ik_x\tilde{\psi}_z \tag{A.56}$$

$$\tilde{u}_y\left(k_x,k_y,x,y,z,\omega\right) = -i\,\mathrm{sgn}\left(z\right)\nu\tilde{\phi} - ik_y\tilde{\psi}_y + ik_x\tilde{\psi}_x, \tag{A.57}$$

and further applying (A.6) results in expressions for stress

$$\tilde{\tau}_{xx}\left(k_x,k_y,x,y,z,\omega\right) = \lambda\frac{\omega^2}{\alpha^2}\tilde{\phi} + 2\mu\left[-k_x^2\tilde{\phi} + k_x\gamma\,\mathrm{sgn}\left(z\right)\tilde{\psi}_y - k_xk_y\tilde{\psi}_z\right] \tag{A.58}$$

$$\tilde{\tau}_{xy}\left(k_x,k_y,x,y,z,\omega\right) = \mu\left[-2k_xk_y\tilde{\phi} - k_x\gamma\,\mathrm{sgn}\left(z\right)\tilde{\psi}_x + k_y\gamma\,\mathrm{sgn}\left(z\right)\tilde{\psi}_y + \left(k_x^2 - k_y^2\right)\tilde{\psi}_z\right] \tag{A.59}$$

$$\tilde{\tau}_{xz}\left(k_x,k_y,x,y,z,\omega\right) = \mu\left[-2k_x\nu\,\mathrm{sgn}\left(z\right)\tilde{\phi} + k_xk_y\tilde{\psi}_x + \left(\gamma^2 - k_x^2\right)\tilde{\psi}_y - k_y\gamma\,\mathrm{sgn}\left(z\right)\tilde{\psi}_z\right] \tag{A.60}$$

$$\tilde{\tau}_{yy}\left(k_x,k_y,x,y,z,\omega\right) = \lambda\frac{\omega^2}{\alpha^2}\tilde{\phi} + 2\mu\left[-k_y^2\tilde{\phi} - k_y\gamma\,\mathrm{sgn}\left(z\right)\tilde{\psi}_x + k_xk_y\tilde{\psi}_z\right] \tag{A.61}$$

$$\tilde{\tau}_{yz}\left(k_x,k_y,x,y,z,\omega\right) = \mu\left[-2k_y\nu\,\mathrm{sgn}\left(z\right)\tilde{\phi} + \left(k_y^2 - \gamma^2\right)\tilde{\psi}_x - k_xk_y\tilde{\psi}_y + k_x\gamma\,\mathrm{sgn}\left(z\right)\tilde{\psi}_z\right] \tag{A.62}$$

$$\tilde{\tau}_{zz}\left(k_x,k_y,x,y,z,\omega\right) = \lambda\frac{\omega^2}{\alpha^2}\tilde{\phi} + 2\mu\left[-\nu^2\tilde{\phi} + k_y\gamma\,\mathrm{sgn}\left(z\right)\tilde{\psi}_x - k_x\gamma\,\mathrm{sgn}\left(z\right)\tilde{\psi}_y\right]. \tag{A.63}$$

By substituting for the integrands $\tilde{\phi}$, $\tilde{\psi}_x$, $\tilde{\psi}_y$, $\tilde{\psi}_z$ from (A.51-A.54) and omitting the factor $\exp\left[-ik_x\left(x-x'\right) - ik_y\left(y-y'\right)\right]$ we obtain $\tilde{\tau}^x_{\alpha\beta}$, $\tilde{\tau}^y_{\alpha\beta}$, $\tilde{\tau}^z_{\alpha\beta}$ for unit dislocation in the directions $\boldsymbol{e}^x$, $\boldsymbol{e}^y$, $\boldsymbol{e}^z$ respectively:

$$\begin{aligned}\tilde{\tau}^x_{xx}\left(k_x,k_y,z,\omega\right) =& 2\mu^2\mathrm{sgn}\left(z\right)\left[-2k_x^3\exp\left(-i\nu\left|z\right|\right) + \left(k_x^3 - k_xk_y^2 - k_x\gamma^2\right)\exp\left(-i\gamma\left|z\right|\right)\right] + \\ & 2\lambda\mu\,\mathrm{sgn}\left(z\right)k_x\frac{\omega^2}{\alpha^2}\exp\left(-i\nu\left|z\right|\right)\end{aligned} \tag{A.64}$$

$$\begin{aligned}\tilde{\tau}^y_{xx}\left(k_x,k_y,z,\omega\right) =& 4\mu^2\mathrm{sgn}\left(z\right)\left[-k_x^2k_y\exp\left(-i\nu\left|z\right|\right) + k_x^2k_y\exp\left(-i\gamma\left|z\right|\right)\right] + \\ & 2\lambda\mu\,\mathrm{sgn}\left(z\right)k_y\frac{\omega^2}{\alpha^2}\exp\left(-i\nu\left|z\right|\right)\end{aligned} \tag{A.65}$$

$$\begin{aligned}\tilde{\tau}^z_{xx}\left(k_x,k_y,z,\omega\right) =& 4\mu^2\left[-k_x^2\nu\exp\left(-i\nu\left|z\right|\right) + k_x^2\gamma\exp\left(-i\gamma\left|z\right|\right)\right] + \\ & \left(-2\lambda\mu k_x^2\frac{\omega^2}{\alpha^2\nu} + 2\lambda\mu\nu\frac{\omega^2}{\alpha^2} + \lambda^2\frac{\omega^4}{\alpha^4\nu}\right)\exp\left(-i\nu\left|z\right|\right)\end{aligned} \tag{A.66}$$

$$\tilde{\tau}^x_{xy}(k_x,k_y,z,\omega) = \mu^2 \mathrm{sgn}(z)\left[-4k_x^2k_y\exp(-i\nu|z|) + \left(-k_y^3+3k_x^2k_y-k_y\gamma^2\right)\exp(-i\gamma|z|)\right] \tag{A.67}$$

$$\tilde{\tau}^y_{xy}(k_x,k_y,z,\omega) = \mu^2 \mathrm{sgn}(z)\left[-4k_xk_y^2\exp(-i\nu|z|) + \left(-k_x^3+3k_xk_y^2-k_x\gamma^2\right)\exp(-i\gamma|z|)\right] \tag{A.68}$$

$$\begin{aligned}\tilde{\tau}^z_{xy}(k_x,k_y,z,\omega) =& 4\mu^2\left[-k_xk_y\nu\exp(-i\nu|z|) + k_xk_y\gamma\exp(-i\gamma|z|)\right] - \\ & 2\lambda\mu k_xk_y\frac{\omega^2}{\alpha^2\nu}\exp(-i\nu|z|)\end{aligned} \tag{A.69}$$

$$\tilde{\tau}^x_{xz}(k_x,k_y,z,\omega) = -\frac{\mu^2}{\gamma}\left\{4k_x^2\nu\gamma\exp(-i\nu|z|) + \left[k_y^2\gamma^2+k_x^2k_y^2+\left(\gamma^2-k_x^2\right)^2\right]\exp(-i\gamma|z|)\right\} \tag{A.70}$$

$$\tilde{\tau}^y_{xz}(k_x,k_y,z,\omega) = \frac{\mu^2k_xk_y}{\gamma}\left[-4\nu\gamma\exp(-i\nu|z|) + \left(3\gamma^2-k_x^2-k_y^2\right)\exp(-i\gamma|z|)\right] \tag{A.71}$$

$$\begin{aligned}\tilde{\tau}^z_{xz}(k_x,k_y,z,\omega) =& -2\mu^2\mathrm{sgn}(z)\left[2k_x\nu^2\exp(-i\nu|z|) + \left(k_x^3+k_xk_y^2-\gamma^2k_x\right)\exp(-i\gamma|z|)\right] - \\ & 2\lambda\mu\,\mathrm{sgn}(z)\,k_x\frac{\omega^2}{\alpha^2}\exp(-i\nu|z|)\end{aligned} \tag{A.72}$$

$$\begin{aligned}\tilde{\tau}^x_{yy}(k_x,k_y,z,\omega) =& 4\mu^2\mathrm{sgn}(z)\left[-k_xk_y^2\exp(-i\nu|z|) + k_xk_y^2\exp(-i\gamma|z|)\right] + \\ & 2\lambda\mu\,\mathrm{sgn}(z)\,k_x\frac{\omega^2}{\alpha^2}\exp(-i\nu|z|)\end{aligned} \tag{A.73}$$

$$\begin{aligned}\tilde{\tau}^y_{yy}(k_x,k_y,z,\omega) =& 2\mu^2\mathrm{sgn}(z)\left[-2k_y^3\exp(-i\nu|z|) + \left(k_y^3-k_x^2k_y-k_y\gamma^2\right)\exp(-i\gamma|z|)\right] + \\ & 2\lambda\mu\,\mathrm{sgn}(z)\,k_y\frac{\omega^2}{\alpha^2}\exp(-i\nu|z|)\end{aligned} \tag{A.74}$$

$$\begin{aligned}\tilde{\tau}^z_{yy}(k_x,k_y,z,\omega) =& 4\mu^2\left[-k_y^2\nu\exp(-i\nu|z|) + k_y^2\gamma\exp(-i\gamma|z|)\right] + \\ & \left(-2\lambda\mu k_y^2\frac{\omega^2}{\alpha^2\nu} + 2\lambda\mu\nu\frac{\omega^2}{\alpha^2} + \lambda^2\frac{\omega^4}{\alpha^4\nu}\right)\exp(-i\nu|z|)\end{aligned} \tag{A.75}$$

$$\tilde{\tau}^x_{yz}(k_x,k_y,z,\omega) = \frac{\mu^2k_xk_y}{\gamma}\left[-4\nu\gamma\exp(-i\nu|z|) + \left(3\gamma^2-k_x^2-k_y^2\right)\exp(-i\gamma|z|)\right] \tag{A.76}$$

$$\tilde{\tau}^y_{yz}(k_x,k_y,z,\omega) = -\frac{\mu^2}{\gamma}\left\{4k_y^2\nu\gamma\exp(-i\nu|z|) + \left[k_x^2\gamma^2+k_x^2k_y^2+\left(\gamma^2-k_y^2\right)^2\right]\exp(-i\gamma|z|)\right\} \tag{A.77}$$

$$\begin{aligned}\tilde{\tau}^z_{yz}(k_x,k_y,z,\omega) =& -2\mu^2\mathrm{sgn}(z)\left[2k_y\nu^2\exp(-i\nu|z|) + \left(k_y^3+k_x^2k_y-k_y\gamma^2\right)\exp(-i\gamma|z|)\right] - \\ & 2\lambda\mu\,\mathrm{sgn}(z)\,k_y\frac{\omega^2}{\alpha^2}\exp(-i\nu|z|)\end{aligned} \tag{A.78}$$

$$\tilde{\tau}^x_{zz}(k_x,k_y,z,\omega) = -2\mu^2 \mathrm{sgn}(z)\left[2k_x\nu^2\exp(-i\nu|z|) + \left(k_x^3 + k_xk_y^2 - k_x\gamma^2\right)\exp(-i\gamma|z|)\right] + 2\lambda\mu\,\mathrm{sgn}(z)\,k_x\frac{\omega^2}{\alpha^2}\exp(-i\nu|z|) \tag{A.79}$$

$$\tilde{\tau}^y_{zz}(k_x,k_y,z,\omega) = -2\mu^2 \mathrm{sgn}(z)\left[2k_y\nu^2\exp(-i\nu|z|) + \left(k_y^3 + k_x^2k_y - k_y\gamma^2\right)\exp(-i\gamma|z|)\right] + 2\lambda\mu\,\mathrm{sgn}(z)\,k_y\frac{\omega^2}{\alpha^2}\exp(-i\nu|z|) \tag{A.80}$$

$$\tilde{\tau}^z_{zz}(k_x,k_y,z,\omega) = -4\mu^2\left[\nu^3\exp(-i\nu|z|) + \left(k_x^2\gamma + k_y^2\gamma\right)\exp(-i\gamma|z|)\right] + \lambda^2\frac{\omega^4}{\alpha^4\nu}\exp(-i\nu|z|), \tag{A.81}$$

so the stress change due to the dislocation $\Delta\boldsymbol{u}(x',y',\omega)$ acting on a fault plane $\Sigma : z' = 0$ is

$$\tau_{\alpha\beta}(x,y,z,\omega) = \frac{i}{8\pi^2\omega^2\rho}\int_\Sigma\int_{-\infty}^{\infty}\int_{-\infty}^{\infty}\left(\tilde{\tau}^x_{\alpha\beta}\Delta u_x + \tilde{\tau}^y_{\alpha\beta}\Delta u_y + \tilde{\tau}^z_{\alpha\beta}\Delta u_z\right) \exp\left[-ik_x(x-x') - ik_y(y-y')\right]dk_xdk_yd\Sigma'. \tag{A.82}$$

Formulas (A.64-A.81) are originally presented in this work.

A.3 Discretization of the spectra

Let us assume that the fault area is bounded. The response $\tau_{\alpha\beta}$ of a periodic fault repetition in the plane $z = 0$ with period L_x in the x-direction and with period L_y in the y-direction can be written as

$$\tau_{\alpha\beta}(x,y,z,\omega) = \frac{i}{8\pi^2\omega^2\rho}\sum_{n_x=-\infty}^{\infty}\sum_{n_y=-\infty}^{\infty}\int_\Sigma\int_{-\infty}^{\infty}\int_{-\infty}^{\infty}\left(\tilde{\tau}^x_{\alpha\beta}\Delta u_x + \tilde{\tau}^y_{\alpha\beta}\Delta u_y + \tilde{\tau}^z_{\alpha\beta}\Delta u_z\right) \exp\left[-ik_x(x-x'-n_xL_x) - ik_y(y-y'-n_yL_y)\right]dk_xdk_yd\Sigma'. \tag{A.83}$$

We interchange the sums and the integrals, and since

$$\sum_{n_x=-\infty}^{\infty}\exp(ik_xn_xL_x) = \frac{2\pi}{L_x}\sum_{m=-\infty}^{\infty}\delta\left(k_x - \frac{2\pi m}{L_x}\right) \tag{A.84}$$

$$\sum_{n_y=-\infty}^{\infty}\exp(ik_yn_yL_y) = \frac{2\pi}{L_y}\sum_{n=-\infty}^{\infty}\delta\left(k_y - \frac{2\pi n}{L_y}\right) \tag{A.85}$$

where δ is the Dirac delta function, we obtain

$$\tau_{\alpha\beta}(x,y,z,\omega) = \frac{i}{2L_xL_y\omega^2\rho}\int_\Sigma \sum_{m=-\infty}^{\infty}\sum_{n=-\infty}^{\infty}\left(\tilde{\tau}^x_{\alpha\beta}\Delta u_x + \tilde{\tau}^y_{\alpha\beta}\Delta u_y + \tilde{\tau}^z_{\alpha\beta}\Delta u_z\right) \exp\left[-i\frac{2\pi m}{L_x}(x-x') - i\frac{2\pi n}{L_y}(y-y')\right] d\Sigma'. \quad (A.86)$$

Thus the integrals over wavenumbers k_x and k_y with infinite limits change to sum with discrete wavenumbers

$$k_{xm} = \frac{2\pi m}{L_x} \quad (A.87)$$

$$k_{yn} = \frac{2\pi n}{L_y}, \quad (A.88)$$

running from $-\infty$ to ∞. Time domain solution can be obtained by inverse Fourier transform (A.4), so

$$\tau_{\alpha\beta}(x,y,z,t) = \int_{-\infty}^{\infty}\frac{i}{4\pi L_xL_y\omega^2\rho}\int_\Sigma \sum_{m=-\infty}^{\infty}\sum_{n=-\infty}^{\infty}\left(\tilde{\tau}^x_{\alpha\beta}\Delta u_x + \tilde{\tau}^y_{\alpha\beta}\Delta u_y + \tilde{\tau}^z_{\alpha\beta}\Delta u_z\right) \exp\left[i\omega t - ik_{xm}(x-x') - ik_{yn}(y-y')\right] d\Sigma' d\omega. \quad (A.89)$$

This is a time response of an infinite number of identical faults, equally distributed in the plane $z = 0$ surrounded by an infinite medium. It is easy to isolate just the response of a single fault for horizontal coordinates x, y within L_x, L_y spatial periods respectively. We have to just assume that time evolution of the dislocation takes finite period, e.g, $(0,\ t')$, and also $0 < t < t''$, where t'' is the time of the first disturbance arrival from the neighboring faults. Following inequalities hold for rectangular faults:

$$\min\left(\frac{\sqrt{\left(L_x-\frac{L}{2}\right)^2+z^2}}{v_P}, \frac{\sqrt{\left(L_y-\frac{W}{2}\right)^2+z^2}}{v_P}\right) \quad \geq \quad t'' \quad \geq \quad \min\left(\frac{\sqrt{(L_x-L)^2+z^2}}{v_P}, \frac{\sqrt{(L_y-W)^2+z^2}}{v_P}\right). \quad (A.90)$$

An exact value of t'' depends on a one or several nucleation points positions (if the ruptures does not start from single point). The inverse Fourier transform is usually evaluated also by

the discrete Fourier transform. Similarly to introduction of spatial periodicity, we consider dislocation process repeats again and again on each fault with frequency $1/T$, hence (A.89) becomes

$$\tau_{\alpha\beta}(x,y,z,t) = \sum_{j=-\infty}^{\infty} \frac{i}{2TL_xL_y\omega_j^2\rho} \int_\Sigma \sum_{m=-\infty}^{\infty}\sum_{n=-\infty}^{\infty} \left(\tilde{\tau}^x_{\alpha\beta}\Delta u_x + \tilde{\tau}^y_{\alpha\beta}\Delta u_y + \tilde{\tau}^z_{\alpha\beta}\Delta u_z\right) \exp\left[i\omega_j t - ik_{xm}(x-x') - ik_{yn}(y-y')\right] d\Sigma'. \quad \text{(A.91)}$$

where

$$\omega_j = \frac{2\pi j}{T}. \quad \text{(A.92)}$$

However, it is not straightforward to isolate the response of a single fault, as we deal with the response of an infinite number of the faults and the response of the neighboring faults is aliased into the time interval of the interest. Aki & Larner (1970) solved this problem by performing the Fourier expansion in the complex frequency $\tilde{\omega}$ domain:

$$g(\tilde{\omega}_j) = \frac{1}{T}\int_0^T g(t)\exp\left(-i\omega_j^R t + \omega^I t\right) dt \quad \text{(A.93)}$$

$$g(t) = \exp\left(-\omega^I t\right) \sum_{j=-\infty}^{\infty} g(\tilde{\omega}_j)\exp\left(i\omega_j^R t\right) \quad \text{(A.94)}$$

where $\tilde{\omega}_j = \omega_j^R + i\,\omega^I$, $\omega^I < 0$ is the constant imaginary part of the complex frequency and is chosen such that

$$\exp\left(\omega^I T\right) \ll 1. \quad \text{(A.95)}$$

Thus the response generated in the time interval $[-T, 0]$ is attenuated by $\exp\left(\omega^I T\right)$, the response generated in the time interval $[-2T, -T]$ is attenuated by $\exp\left(2\omega^I T\right)$, and so on. The responses generated in the time interval $[0, T]$ are not affected by ω^I at all. Hence we have to assume just times $0 < t < t''$, where t'' is the time of the first disturbance arrival from the neighboring faults. The results should not depend on particular value of ω^I, Bouchon (2003) recommends ω^I from interval $[-\pi/T, -2\pi/T]$, which should suppress the responses from previous time periods sufficiently. If the spatial periods L_x, L_y are long, we do not have to care much about the choice of ω^I, as the geometrical spreading damps the time responses from neighboring faults.

A.4 Space-time discretization

We generally apply the method for the dislocation given numerically at discrete set of points both in the space and time. Thus we have to calculate both the integral over the fault in (A.92) and the discrete Fourier spectrum of Δu_ζ with (A.93) numerically. We evaluate the integral over the fault (A.92) applying extended trapezoidal rule, so the integration changes just to the summation (assuming that dislocation vanishes at the border of the fault) with element size of $\Delta x' \Delta y' = (LW)/(N_L N_W)$, where L is a length and W is a width of the fault. The discrete Fourier spectrum of the dislocation integral is calculated by discrete Fourier series introducing periodicity in the frequency domain with the period N_T/T, where N_T is number of time samples with step $\Delta t = T/N_T$. Thus the summation over j in (A.92) becomes finite. It is also reasonable to assume periodicity in the wavenumber domain with the periods $(2N_M+1)/L_x$, $(2N_N+1)/L_y$ respectively. This results in the spatial discretization with $\Delta x = L_x/(2N_M+1)$, $\Delta y = L_y/(2N_N+1)$ steps, respectively. Thus both the summations over m and n in (A.92) become finite. Then

$$\tau_{\alpha\beta}\left(x_p, y_q, z, t_s\right) = \sum_{j=0}^{N_T-1} \frac{i}{2N_T L_x L_y \tilde{\omega}_j^2 \rho} \sum_{k=0}^{N_L-1} \sum_{l=0}^{N_W-1} \sum_{m=-N_M}^{N_M} \sum_{n=-N_N}^{N_N} \left(\tilde{\tau}_{\alpha\beta}^x \Delta u_x + \tilde{\tau}_{\alpha\beta}^y \Delta u_y + \tilde{\tau}_{\alpha\beta}^z \Delta u_z\right) \exp\left[i\tilde{\omega}_j t_s - ik_{xm}\left(x_p - x'_k\right) - ik_{yn}\left(y_q - y'_l\right)\right] \Delta x' \Delta y', \tag{A.96}$$

where

$$\Delta u_x\left(x'_k, y'_l, \tilde{\omega}_j\right) = \sum_{s=0}^{N_T-1} \Delta u_x\left(x'_k, y'_l, t_s\right) \exp\left(i\tilde{\omega}^I t_s\right) \exp\left(-i\tilde{\omega}_j^R t_s\right), \tag{A.97}$$

$$x'_k = k\Delta x', \quad y'_l = l\Delta y', \quad x_p = p\Delta x, \quad y_q = q\Delta y, \quad t_s = s\Delta t. \tag{A.98}$$

The truncation of the sum limits does not affect the results, if the periodic continuation of the spectra ($k_x, k_y, \tilde{\omega}$-domain) is done in the proper way, by careful utilization of the sampling theorem. Particularly, the spectrum

$$\tilde{\tau}_{\alpha\beta}(k_x, k_y, \tilde{\omega}_j, z) = \sum_{k=0}^{N_L-1} \sum_{l=0}^{N_W-1} \frac{i}{\tilde{\omega}_j^2} \left(\tilde{\tau}_{\alpha\beta}^x \Delta u_x + \tilde{\tau}_{\alpha\beta}^y \Delta u_y + \tilde{\tau}_{\alpha\beta}^z \Delta u_z\right) \exp\left(-ik_{xn} x'_k - ik_{ym} y'_l\right) \tag{A.99}$$

has to vanish for increasing frequencies and wavenumbers. This requires appropriate smoothness of the dislocation, what can be seen from (A.82). Extending the integration over the fault to the whole plane $z = 0$ yields

$$\tau_{\alpha\beta}\left(x, y, z, \omega\right) = \frac{i}{8\pi^2\omega^2\rho}\int_{-\infty}^{\infty}\int_{-\infty}^{\infty}\left(\tilde{\tau}^x_{\alpha\beta}\widetilde{\Delta u}_x + \tilde{\tau}^y_{\alpha\beta}\widetilde{\Delta u}_y + \tilde{\tau}^z_{\alpha\beta}\widetilde{\Delta u}_z\right) \exp\left(-ik_x x - ik_y y\right) dk_x dk_y. \tag{A.100}$$

where $\widetilde{\Delta u}_\zeta = \widetilde{\Delta u}_\zeta(k_x, k_y, \omega)$ is the Fourier spectrum of the dislocation Δu_ζ, as the dislocation is zero outside the fault area Σ. If we assume $\Delta x' = \Delta x$, $\Delta y' = \Delta y$ and $\Delta u_\zeta(x_k, y_l, \tilde{\omega}_j) = 0$ for $N_L \leq k \leq 2M_M + 1$, $N_W \leq l \leq 2M_N + 1$, then (A.99) results in

$$\tilde{\tau}_{\alpha\beta}(k_x, k_y, \tilde{\omega}_j, z) = \frac{i\Delta x\Delta y}{\tilde{\omega}_j^2}\left(\tilde{\tau}^x_{\alpha\beta}\widetilde{\Delta u}_x + \tilde{\tau}^y_{\alpha\beta}\widetilde{\Delta u}_y + \tilde{\tau}^z_{\alpha\beta}\widetilde{\Delta u}_z\right). \tag{A.101}$$

Closer look at relations (A.64-A.81) suggests that $\tilde{\tau}^\zeta_{\alpha\beta}$ are not functions from L2 space with respect to k_x, k_y (see later Fig. A.2). Consequently, $\widetilde{\Delta u}_\zeta$ has to decrease rapidly enough to suppress $\tilde{\tau}^\zeta_{\alpha\beta}$. In other words, Δu_ζ has to be smooth enough. Now let us return to the spatial discretization, both N_M and N_N have to be chosen such that $\tilde{\tau}_{\alpha\beta}(k_{xm}, k_{yn}, \tilde{\omega}_j, z)$ is effectively zero for $m \geq N_M$, $n \geq N_N$.

A.5 An implementation for the stress change along the fault due to the shear dislocation

A stress change along the fault due to the shear dislocation (slip) is a case of our special interest. The details of implementation come from private communication with Prof. Bouchon. Particularly, we want to evaluate traction, force per unit area acting on the fault, at every point of the fault. We consider slip with only non-zero component Δu_x along the fault. The normal traction change τ_{zz} is zero in this case, as the traction has to be continuous across the fault and expression (A.79) for $\tilde{\tau}^x_{zz}$ is an odd function of z. The shear

traction change $\boldsymbol{T}^t = (\tau_{xz}, \tau_{yz})$ can be evaluated in following way

$$\tau_{xz}\left(x_p, y_q, z=0, t_s\right) = \exp\left(-\omega^I t_s\right) \sum_{j=0}^{N_T-1} \sum_{k=0}^{N_L-1} \sum_{l=0}^{N_W-1} \frac{i\mu^2 \Delta u_x\left(x'_k, y'_l, \tilde{\omega}_j\right)}{2N_T\left(2N_M+1\right)\left(2N_N+1\right)\rho\tilde{\omega}_j^2} \sum_{m=-N_M}^{N_M} \sum_{n=-N_N}^{N_N} A_{jmn} \exp\left[i\tilde{\omega}_j t_s - ik_{xm}\left(x_p - x'_k\right) - ik_{yn}\left(y_q - y'_l\right)\right], \tag{A.102}$$

$$\tau_{yz}\left(x, y, z=0, t_s\right) = \exp\left(-\omega^I t_s\right) \sum_{j=1}^{N_T-1} \sum_{k=0}^{N_L-1} \sum_{l=0}^{N_W-1} \frac{i\mu^2 \Delta u_x\left(x'_k, y'_l, \tilde{\omega}_j\right)}{2N_T\left(2N_M+1\right)\left(2N_N+1\right)\rho\tilde{\omega}_j^2} \sum_{m=-N_M}^{N_M} \sum_{n=-N_N}^{N_N} B_{jmn} \exp\left[i\tilde{\omega}_j t_s - ik_{xm}\left(x_p - x'_k\right) - ik_{yn}\left(y_q - y'_l\right)\right], \tag{A.103}$$

with

$$\begin{aligned} A_{jmn} &:= \tilde{\tau}_{xz}^x\left(k_{xm}, k_{yn}, z=0, \tilde{\omega}_j\right) = \\ &= -\frac{1}{\gamma_{jmn}}\left[4k_{xm}^2\nu_{jmn}\gamma_{jmn} + k_{xm}^2k_{yn}^2 + k_{yn}^2\gamma_{jmn}^2 + \left(\gamma_{jmn}^2 - k_{yn}^2\right)^2\right], \end{aligned} \tag{A.104}$$

$$\begin{aligned} B_{jmn} &:= \tilde{\tau}_{yz}^x\left(k_{xm}, k_{yn}, z=0, \tilde{\omega}_j\right) = \\ &= \frac{k_{xm}k_{yn}}{\gamma_{jmn}}\left[-4\nu_{jmn}\gamma_{jmn} + 3\gamma_{jmn}^2 - k_{xm}^2 - k_{yn}^2\right], \end{aligned} \tag{A.105}$$

$$\nu_{jmn} = \sqrt{\frac{\tilde{\omega}_j^2}{v_P^2} - k_{xm}^2 - k_{yn}^2}, \quad \operatorname{Im}\nu_{jmn} < 0, \tag{A.106}$$

$$\gamma_{jmn} = \sqrt{\frac{\tilde{\omega}_j^2}{v_S^2} - k_{xm}^2 - k_{yn}^2}, \quad \operatorname{Im}\gamma_{jmn} < 0, \tag{A.107}$$

$$k_{xm} = \frac{2\pi m}{L_x}, \quad k_{yn} = \frac{2\pi n}{L_y}, \tag{A.108}$$

$$\Delta x' = \Delta x = L_x/(2N_M+1), \quad \Delta y' = \Delta y = L_y/(2N_N+1) \tag{A.109}$$

$$x_p = p\Delta x, \quad p = 0 \ldots N_L - 1 \tag{A.110}$$

$$y_q = q\Delta x, \quad q = 0 \ldots N_W - 1 \tag{A.111}$$

$$x'_k = k\Delta x, \quad k = 0 \ldots N_L - 1 \tag{A.112}$$

$$y'_l = l\Delta x, \quad l = 0 \ldots N_W - 1 \tag{A.113}$$

These expressions were first presented by Bouchon (1997). An example of both $|A_{jmn}|$ and $|B_{jmn}|$ is plotted in Fig. A.2. Hereafter, we hold $z = 0$ and we do not write it to the

arguments for a brevity. Both the expressions (A.102) and (A.103) form convolution in spatial domain. This convolution can be evaluated either in the spectral or spatial domain. Both length L and width W of the fault have to be smaller than spatial periods L_x and L_y respectively, to provide sufficient t''. Thus, N_L is several times smaller than $2N_M+1$ and N_W is several times smaller than $2N_N+1$, so that evaluation of the slip spectrum by the fast Fourier transform (FFT) would require substantial zero padding. Moreover, subsequent inverse Fourier transform over discrete wavenumbers, carried out by FFT, would lead to many useless operations, getting the results for points out of our interest (the points out of the fault, where the aliased response of multiple faults is assumed). Thus we implement the convolution directly in the spatial domain. Assuming $N_M{=}N_N$ and taking into the account properties $A_{jmn} = A_{j(-m)n} = A_{jm(-n)}$ and $B_{jmn} = -B_{j(-m)n} = -B_{jm(-n)}$, it is possible to reduce summations over wavenumbers, so (A.102) and (A.103) become in the frequency domain

$$\begin{aligned}\tau_{xz}\left(x_p, y_q, \tilde{\omega}_j\right) = &\sum_{k=0}^{N_L-1}\sum_{l=0}^{N_W-1}\frac{i\mu^2\Delta u\left(x'_k, y'_l, \tilde{\omega}_j\right)}{2T\left(2N_M+1\right)^2\rho\tilde{\omega}_j^2}\sum_{m=1}^{N_M}\sum_{n=1}^{N_M}\\ &\left[2A_{jmn}\cos\frac{2\pi m\left(p-k\right)}{2M+1}\cos\frac{2\pi n\left(q-l\right)}{2M+1}+\right.\\ &\left.A_{jm0}\cos\frac{2\pi m\left(p-k\right)}{2M+1}+A_{j0n}\cos\frac{2\pi n\left(q-l\right)}{2M+1}+A_{j00}\right], \qquad \text{(A.114)}\\ \tau_{yz}\left(x_p, y_q, \tilde{\omega}_j\right) = &\sum_{k=0}^{N_L-1}\sum_{l=0}^{N_W-1}\frac{i\mu^2\Delta u\left(x'_k, y'_l, \tilde{\omega}_j\right)}{2T\left(2N_M+1\right)^2\rho\tilde{\omega}_j^2}\sum_{m=1}^{N_M}\sum_{n=1}^{N_M}\\ &-2B_{jmn}\sin\frac{2\pi m\left(p-k\right)}{2M+1}\sin\frac{2\pi n\left(q-l\right)}{2M+1}. \qquad \text{(A.115)}\end{aligned}$$

These expressions can be rewritten in the following way,

$$\tau_{xz}\left(x_p, y_q, \tilde{\omega}_j\right) = \sum_{k=0}^{N_L-1}\sum_{l=0}^{N_W-1}\frac{i\mu^2\Delta u\left(x'_k, y'_l, \tilde{\omega}_j\right)}{2T\left(2N_M+1\right)^2\rho\tilde{\omega}_j^2}C_{j(p-k)(q-l)}, \qquad \text{(A.116)}$$

$$\tau_{yz}\left(x_p, y_q, \tilde{\omega}_j\right) = \sum_{k=0}^{N_L-1}\sum_{l=0}^{N_W-1}\frac{i\mu^2\Delta u\left(x'_k, y'_l, \tilde{\omega}_j\right)}{2T\left(2N_M+1\right)^2\rho\tilde{\omega}_j^2}D_{j(p-k)(q-l)} \qquad \text{(A.117)}$$

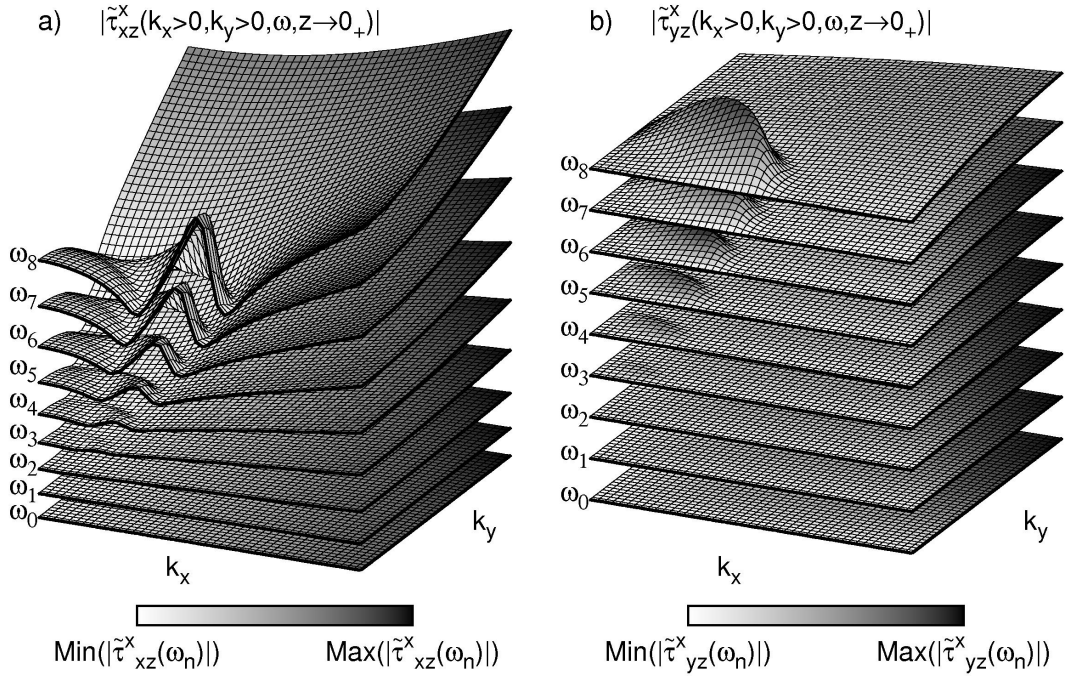

Figure A.2: An example of a) $|A_{jmn}| = |\tilde{\tau}^x_{xz}(k_{xm}, k_{yn}, z = 0, \tilde{\omega}_j)|$ and b) $|B_{jmn}| = \left|\tilde{\tau}^x_{yz}(k_{xm}, k_{yn}, z = 0, \tilde{\omega}_j)\right|$ for 8 frequencies. The amplitude spectra grow with increasing k_x and k_y.

with

$$C_{juv} = \sum_{m=1}^{N_M}\sum_{n=1}^{N_M}\Bigg(2A_{jmn}\cos\frac{2\pi mu}{2M+1}\cos\frac{2\pi nv}{2M+1} + A_{jm0}\cos\frac{2\pi mu}{2M+1} + A_{j0n}\cos\frac{2\pi nv}{2M+1} + A_{j00}\Bigg), \tag{A.118}$$

$$D_{juv} = \sum_{m=1}^{N_M}\sum_{n=1}^{N_M} -2B_{jmn}\sin\frac{2\pi mu}{2M+1}\sin\frac{2\pi nv}{2M+1} \tag{A.119}$$

where

$$u = -N_L + 1 \ldots N_L - 1, \tag{A.120}$$

$$v = -N_W + 1 \ldots N_W - 1. \tag{A.121}$$

Hence expressions (A.102) and (A.103) can be evaluated as

$$\tau_{xz}\left(x_p, y_q, \tilde{\omega}_j\right) = \sum_{k=0}^{N_L-1} \sum_{l=0}^{N_W-1} \frac{i\mu^2 \Delta u\left(x'_k, y'_l, \tilde{\omega}_j\right)}{2T\left(2M+1\right)^2 \rho \tilde{\omega}_j^2} C_{j|p-k||q-l|}, \tag{A.122}$$

$$\tau_{yz}\left(x_p, y_q, \tilde{\omega}_j\right) = \sum_{k=0}^{N_L-1} \sum_{l=0}^{N_W-1} \frac{i\mu^2 \Delta u\left(x'_k, y'_l, \tilde{\omega}_j\right)}{2T\left(2M+1\right)^2 \rho \tilde{\omega}_j^2} \operatorname{sgn}\left(p-k\right) \operatorname{sgn}\left(q-l\right) D_{j|p-k||q-l|}, \tag{A.123}$$

$$\tau_{xz}\left(x_p, y_q, t_s\right) = \exp\left(-\omega^I t_s\right) \sum_{j=0}^{N_T-1} \tau_{xz}\left(x_p, y_q, \tilde{\omega}_j\right) \exp\left(i\tilde{\omega}_j t_s\right), \tag{A.124}$$

$$\tau_{yz}\left(x_p, y_q, t_s\right) = \exp\left(-\omega^I t_s\right) \sum_{j=0}^{N_T-1} \tau_{yz}\left(x_p, y_q, \tilde{\omega}_j\right) \exp\left(i\tilde{\omega}_j t_s\right). \tag{A.125}$$

Since both slip and stress time histories have non-zero static parts, we cannot simply apply FFT, as it would lead to alias effect in the time domain. Thus it is convenient to work with slip velocity functions, getting stress rates, which are to be integrated in the time domain to stress time histories. Hence we can perform frequency filtering easily and apply FFT algorithm for the inverse Fourier transform. The algorithm is then very simple[1]: i) We calculate (A.97) the Fourier transform of the slip velocity function applying 1D FFT. ii) We fix the frequency and calculate (A.104-A.108) respectively for all m, n. iii) We perform summation over wavenumbers (A.118-A.119) for all $u = 0 \ldots N_L - 1$, $v = 0 \ldots N_W - 1$. iv) We evaluate the convolution with the slip velocity distribution at given frequency (A.122-A.123). Further, we repeat steps ii)-iv) for different frequencies. At the end we perform inverse Fourier transforms (A.124-A.125) for each point along the fault and integrate resulting stress rates to stress time histories adopting extended trapezoidal rule. Loop over frequencies is parallelized using *OpenMP* directives. In fact, the parallelization is very effective in this case, as the calculation for one frequency is completely independent from others.

[1]The all referred expressions are written for stress and slip functions. Equivalently, these expressions are also valid substituting first and latter for stress and slip rates, respectively.

References

Aki, K. (1967). Scaling laws of seismic spectrum, *J. Geophys. Res. 72*, 1217–1231.

Aki, K. & K. Larner (1970). Surface motion of a layered medium having an irregular interface due to incident plane SH waves, *J. Geophys. Res. 75*, 933-954.

Aki, K., & P. G. Richards (1980). *Quantitative Seismology: Theory and Methods*, W.H. Freeman and Company, New York.

Andrews, D. J. (1974). Evaluation of static stress on a fault plane from a Green's function, *Bull. Seism. Soc. Am. 61*, 1629–1633.

Andrews, D. J. (1976a). Rupture propagation with finite stress in antiplane strain, *J. Geophys. Res. 81*, 3575-3582.

Andrews, D. J. (1976b). Rupture velocity of plane strain shear cracks, *J. Geophys. Res. 81*, 5679–5687.

Andrews, D. J. (1980). A stochastic fault model, 1, Static case, *J. Geophys. Res. 85*, 3867–3877.

Andrews, D. J. (1981). A stochastic fault model, 2, Time-dependent case, *J. Geophys. Res. 86*, 10821–10834.

Andrews, D. J. & Y. Ben-Zion (1997). Wrinkle-like slip pulse on a fault between different materials, *J. Geophys. Res. 102*, 553-571.

Ben-Menahem, A. (1961). Radiation of seismic surface-waves from finite moving sources, *Bull. Seism. Soc. Am. 51*, 401–435.

Ben-Zion, Y. (2001). Dynamic ruptures in recent models of earthquake faults, *J. Mech. Phys. Solids 49*, 2209–2244.

Berge-Thierry, C., P. Bernard & A. Herrero (2001). Simulating strong ground motion with the "k-2" kinematic source model: An application to the seismic hazard in the Erzincan basin, Turkey, . *J. Seismology 5*, 85-101.

Bernard, P., A. Herrero & C. Berge (1996). Modeling directivity of heterogeneous earthquake ruptures, *Bull. Seism. Soc. Am. 86*, 1149-1160.

Beroza, G. & T. Mikumo (1996). Short slip duration in dynamic rupture in the presence of heterogeneous fault properties, *J. Geophys. Res. 101*, 22449–22460.

Bizzarri, A. & M. Cocco (2005). 3D dynamic simulations of spontaneous rupture propagation governed by different constitutive laws with rake rotation allowed, *Annals of Geophysics 48*, 279–299.

Boatwright, J. (1982). A dynamic model for far-field accelerations, *Bull. Seism. Soc. Am. 72*, 1049–1068.

Bonnet, M. & H. D. Bui (1993). Regularization of the displacement and traction BIE for 3D elastodynamics using indirect methods.*Advances in Boundary Element Techniques* (ed. J. H. Kane, G. Maier, N. Tosaka and S. N. Atluri), Springer-Verlag, New York.

Bouchon, M. & K. Aki (1977). Discrete wave-number representation of seismic source wave fields, *Bull. Seism. Soc. Am. 67*, 259–277.

Bouchon, M. (1979). Discrete wavenumber representation of elastic wave fields in three-space dimensions, *J. Geophys. Res. 84*, 3609-3614.

Bouchon, M. (1981). A simple method to calculate Greens functions in elastic layered media, *Bull. seism. Soc. Am. 71*, 959-971.

Bouchon, M. (1997). The state of stress on some faults of the San Andreas system as inferred from near-field strong motion data, *J. Geoph. Res. 102*, 11731–11744.

Bouchon, M. (2003). A review of the discrete wavenumber method, *Pure Appl. Geophys. 160*, 445-465.

Bouchon, M. & M. Vallée (2003). Observation of long supershear rupture during the magnitude 8.1 Kunlunshan earthquake, *Science 301*, 824-826.

Bouchon, M., M. P. Bouin, H. Karabulut, M. N. Toksz, M. Dietrich, & A. J. Rosakis (2001). How fast is rupture during an earthquake? New insights from the 1999 Turkey earthquakes, *Geophys. Res. Lett. 28*, 2723-2726.

Broberg, K. (1978). On transient sliding motion, *Geophys. J. R. Astr. Soc. 52*, 397-432.

Burridge, R. & J. R. Willis (1969). The self-similar problem of the expanding elliptical crack in an anisotropic solid, *Proc. Camb. Phil. Soc. 66*, 443–468.

Chen, X. F. & K. Aki (1996). An effective approach to determine the dynamic source parameters, *Pure Appl. Geophys. 146*, 689-696.

Cocco, M., A. Bizzarri & E. Tinti (2004). Physical interpretation of the breakdown process using a rate- and state-dependent friction law, *Tectonophysics 378*, 241-262.

Dalguer, L. A., K. Irikura, W. Zhang & J. D. Riera (2002). Distribution of dynamic and static stress changes during 2000 Tottori (Japan) earthquake: brief interpretation of the earthquake sequences; foreshocks, mainshock and aftershocks, *Geophys. Res. Lett. Vol. 29*, 1758, doi:10.1029/2001GL014333.

Das, S. (2003). Spontaneous complex earthquake rupture propagation, *Pure Appl. Geophys. 160*, 579–602.

Das, S. & B. V. Kostrov (1988). An investigation of the complexity of the earthquake source time function using dynamic faulting models, *J. Geophys. Res. 93*, 8035-8050.

Day, S. M., G. Yu & D. J. Wald (1998). Dynamic stress changes during earthquake rupture, *Bull. Seism. Soc. Am. 88*, 512–522.

Dieterich, J. H. (1979). Modeling of rock friction: 1. Experimental results and constitutive equations, *J. Geophys. Res. 84*, 2161-2168.

Dunham E. M., P. Favreau & J. M. Carlson (2003). A supershear transition mechanism for cracks, *Science 299*, 1557–1559.

Emolo, A. & A. Zollo (2001). Accelerometric radiation simulation for the September 26, 1997 Umbria-Marche (central Italy) main shocks, *Annali di Geofisica 44*, 605-617.

Fischer, T., & J. Horálek (2005). Slip-generated patterns of swarm microearthquakes from West Bohemia/Vogtland (central Europe): Evidence of their triggering mechanism?, *J. Geophys. Res. 110*, B05S21, doi:10.1029/2004JB003363.

Frankel, A. (1991). High-frequency spectral fall-off of earthquakes, fractal dimension of complex rupture, *b* value, and the scaling of strength on faults, *J. Geophys. Res. 81*, 6291–6302.

Freund, L. B. (1979). The mechanics of dynamic shear crack propagation, *J. Geophys. Res. 84*, 2199-2209.

Fukuyama, E. & R. Madariaga (1998). Rupture dynamics of a planar fault in a 3D elastic medium: rate- and slip-weakening friction, *Bull. Seism. Soc. Am. 88*, 1–17.

Gallovič, F. & J. Brokešová (2004a). On strong ground motion synthesis with k^{-2} slip distributions, *J. Seismology 8*, 211–224.

Gallovič, F. & J. Brokešová (2004b). The k^{-2} rupture model parametric study: example of the 1999 Athens earthquake, *Studia Geoph. et Geod. 48*, 589-613.

Gallovič, F. & J. Brokešová (2007). Hybrid k-squared source model for strong ground motion simulations: an introduction, *Phys. Earth Planet. Interiors. 160*, 34–50, doi:10.1016/j.pepi.2006.09.002.

Geubelle, P. H. & J. R. Rice (1995). A spectral method for three-dimensional elastodynamic fracture problems, *J. Mech. Phys. Solids 43*, 1791–1824.

Griffith, A. A. (1921). The phenomenon of rupture and flow in solids, *Phil. Trans. R. Soc. Lond., Ser. A. 221*, 163-198.

Guatteri, M. & P. Spudich (1998). Coseismic temporal changes of slip direction: The effect of absolute stress on dynamic rupture, *Bull. Seismol. Soc. Am., 88*, 777–789.

Guatteri, M. & P. Spudich (2000). What can strong-motion data tell us about slip-weakening fault-friction laws?, *Bull. Seismol. Soc. Am. 90*, 98-116.

Guatteri, M., P. M. Mai & G. C. Beroza (2004). A pseudo-dynamic approximation to dynamic rupture models for strong ground motion prediction, *Bull. Seism. Soc. Am. 94*, 2051–2063.

Guatteri, M., P. M. Mai, G. C. Beroza & J. Boatwright (2003). Strong ground-motion prediction from stochastic-dynamic source models, *Bull. Seism. Soc. Am. 93*, 301-313.

Hanks, T. C. (1979). b values and $\omega^{-\gamma}$ seismic source models: Implications for tectonic stress variations along active crustal fault zones and the estimation of high-frequency strong ground motion, *J. Geophys. Res. 84*, 2235–2242.

Hartzell, S. H., & T. H. Heaton (1983). Inversion of strong ground motion and teleseismic waveform data for the fault rupture history of the 1979 Imperial Valley, California earthquake, *Bull. Seism. Soc. Am. 73*, 1553-1583.

Hartzell, S., S. Harmsen, A. Frankel, & S. Larsen (1999). Calculation of broadband time histories of ground motion: comparison of methods and validation using strong-ground motion from the 1994 Northridge earthquake, *Bull. Seism. Soc. Am. 89*, 1484-1504.

Haskell, N. A. (1964). Total energy and energy spectral density of elastic wave radiation from propagating faults, *Bull. Seism. Soc. Am. 54*, 1811–1841.

Haskell, N. A. (1966). Total energy and energy spectral density of elastic wave radiation from propagating faults. Part II. A statistical source model, *Bull. Seism. Soc. Am. 56*, 125–140.

Haskell, N. A. (1969). Elastic displacements in the near-field of a propagating fault, *Bull Seism. Soc. Am. 59*, 865–908.

Heaton, T. H. (1990). Evidence for and implications of self-healing pulses of slip in earthquake rupture. *Phys. Earth Planet. Inter. 64*, 1-20.

Herrero, A. & P. Bernard (1994). A kinematic self-similar rupture process for earthquakes, *Bull. Seism. Soc. Am. 84*, 1216-1228.

Hisada, Y. (2000). A theoretical-square model considering the spatial variation in slip and rupture velocity, *Bull. Seism. Soc. Am. 90*, 387-400.

Hisada, Y. (2001). A theoretical omega-square model considering the spatial variation in slip and rupture velocity. Part 2: case for a two-dimensional source model, *Bull. Seism. Soc. Am. 91*, 651-666.

Ida, Y. (1972). Cohesive forces across the tip of a longitudinal-shear crack and Griffiths specific surface energy, *J. Geoph. Res. 77*, 3796–3805.

Ide, S. & M. Takeo (1997). Determination of constitutive relations of fault slip based on seismic waves analysis, *J. Geoph. Res. 102*, 27379–27391.

Kanamori, H. & G. S. Stewart (1978). Seismological aspects of the Guatemala earthquake of February 4, 1976, *J. Geophys. Res. 83*, 3427–3434.

Kanamori, H., (1994). Mechanics of earthquakes, *Annu. Rev. Earth Planet. Sci. 22*, 207–237.

Kennet, B. L. N. & N. J. Kerry (1979). Seismic Waves in a Stratified Half-space, *Geophys. J. Roy. Astr. Soc. 57*, 557-583.

Keilis-Borok, V. I. (1959). On estimation of the displacement in an earthquake source and of source dimensions, *Ann. Geofis. 12*, 205–214.

Kostrov, B. V. (1964). Selfsimilar problems of propagation of shear cracks, *J. Appl. Math. Mech. 28*, 1077–1087.

Kostrov, B. V. (1966). Unsteady propagation of longitudinal shear cracks, *J. Appl. Math. Mech. 28*, 1241-1248.

Kostrov, B. V. & S. Das (1988). *Principles of Earthquake Source Mechanics*, Cambridge University Press, New York.

Lamb, H. (1904). On the propagation of tremors at the surface of an elastic solid, *Phil. Trans. Roy. Soc. London, Ser A, 203*, 1–42.

Lavalle, D. & R. J. Archuleta (2003). Stochastic modeling of slip spatial complexities for the 1979 Imperial Valley, California, earthquake, *Geophys. Res. Lett. Vol. 30*, L08311, doi:10.1029/2004GL022202.

Liu, P., R. J. Archuleta & S. H. Hartzell (2006). Prediction of broadband ground-motion time histories: Hybrid low/high-frequency method, *Bull. Seism. Soc. Am. 96*, 2118–2130, doi: 10.1785/0120060036.

Madariaga, R. (1976). Dynamics of an expanding circular fault, *Bull. Seismol. Soc. Am., 66*, 639-666.

Madariaga, R. (1978). The dynamic field of Haskell's rectangular dislocation fault model, *Bull. Seism. Soc. Am. 68*, 869-887.

Madariaga, R. (1979). On the relation between seismic moment and stress drop in the presence of stress and strength heterogeneity, *J. Geophys. Res. 88*, 2243–2246.

Madariaga, R. & K. B. Olsen (2002). Earthquake dynamics, in *International Handbook of Earthquake & Engineering Seismology* (ed. W. Lee, H. Kanamori, P. Jennings and C. Kisslinger), Academic Press, London.

Mai, P. M. & G. C. Beroza (2002). A spatial random field model to characterize complexity in earthquake slip, *J. Geoph. Res. 107*, 2308, doi:10.1029/2001JB000588.

Mai, P. M., P. Spudich & J. Boatwright (2005). Hypocenter locations in finite-source rupture models, *Bull. Seism. Soc. Am. 95*, 965-980.

Marone, C. J. (1998). Laboratory-derived friction laws and their application to seismic faulting, *Annu. Rev. Earth Planet. Sci. 26*, 643-696.

Mikumo, T. (1994). Dynamic fault rupture processes of moderate-size earthquakes inferred from the results of kinematic waveform inversion, *Ann. Geofis. 37*, 1377–1389.

Mikumo, T., K. B. Olsen, E. Fukuyama & Y. Yagi (2003). Stress-breakdown time and slip-weakening distance inferred from slip-velocity functions on earthquake faults, *Bull. Seism. Soc. Am. 93*, 264-282.

Miyake H., T. Iwata & K. Irikura (2003). Source characterization for broadband ground-motion simulation: Kinematic heterogeneous source model and strong motion generation area, *Bull. Seism. Soc. Am. 93*, 2531–2545.

Nielsen, S. & R. Madariaga (2003). On the self-healing fracture mode, *Bull. Seism. Soc. Am. 93*, 2375-2388.

Oglesby, D. D. & S. M. Day (2002). Stochastic fault stress: implications for fault dynamics and ground motion, *Bull. Seism. Soc. Am. 92*, 3006-3021.

Olsen, K. B., & R. Madariaga & R. J. Archuleta (1997). Three-dimensional dynamic simulation of the 1992 Landers earthquake, *Science 278*, 834-838.

Olson, A. H., & R. Apsel (1982) Finite fault and inversion theory with applications to the 1979 Imperial Valley earthquake, *Bull. Seism. Soc. Am. 72*, 1969-2001.

Peyrat, S., K. Olsen, & R. Madariaga (2001). Dynamic modeling of the 1992 Landers earthquake, *J. Geoph. Res. 106* 26467-26482.

Peyrat, S. & K. B. Olsen (2004). Nonlinear dynamic inversion of the 2000 Western Tottori, Japan, earthquake, *Geophys. Res. Lett. 31*, L05604, doi:10.1029/2003GL019058.

Piatanesi, A., E. Tinti, M. Cocco & E. Fukuyama (2004). The dependence of traction evolution on the earthquake source time function adopted in kinematic rupture models, *Geophys. Res. Lett. 31*, L04609, doi:10.1029/2003GL019225.

Quin, H. (1990). Dynamic stress drop and rupture dynamics of the October 15, 1979 Imperial Valley, California, earthquake *Tectonophysics 175*, 93–117.

Reid, H. F. (1910). The mechanics of the earthquake, in *The California Earthquake of April 18, 1906*, Report of the State Investigation Commission, Vol. 2 (Washington, D.C.: Carnegie Institute of Washington).

Rice, J. R., C. G. Sammis & R. Parsons (2005). Off-fault secondary failure induced by a dynamic slip-pulse, *Bull. Seism. Soc. Am. 95*, 109-134.

Richards, P.G. (1976). Dynamic motions near an earthquake fault: a three-dimensional solution *Bull. Seism. Soc. Am. 66*, 1–32.

Rosakis, A. J., O. Samudrala & D. Coker (1999), Cracks faster than the shear wave speed, *Science 284*, 1337-1340.

Ruina, A. L. (1983). Slip instability and state variable friction laws, *J. Geophys. Res. 88*, 10359-10370.

Scholz, C. H. (2002). *The Mechanics of Earthquakes and Faulting*, Cambridge Univ. Press, Cambridge (2nd edition).

Somerville, P., K. Irikura, R. Graves, S. Sawada, D. Wald, N. Abrahamson, Y. Iwasaki, T. Kagawa, N. Smith & A. Kowada (1999). Characterizing crustal earthquake slip models for the prediction of strong ground motion, *Seism. Res. Lett 70*, 59–80.

Somigliana, C., (1914). Sulla teoria delle distorsioni elastiche, Note I e II., *Atti Accad. Naz. Lincei. Classe Sci. Fis. Mat. e Nat. 23*, 463-472.

Somigliana, C., (1915). Sulla teoria delle distorsioni elastiche, Note I e II., *Atti Accad. Naz. Lincei. Classe Sci. Fis. Mat. e Nat. 24*, 655-666.

Spudich, P. K. P. (1980). The deHoop-Knopoff representation theorem as a linear inverse problem, *Geophys. Res. Lett. 7*, 717–720.

Spudich, P. K. P. (1992). On the inference of absolute stress levels from seismic radiation, *Tectonophysics 211*, 99–106.

Spudich, P. & M. Guatteri (2004). The effect of bandwidth limitations on the inference of earthquake slip-weakening distance from seismograms, *Bull. Seism. Soc. Am. 94*, 2028-2036.

Steacy, S., J. Gomberg, M. Cocco (2005). Introduction to special section: Stress transfer, earthquake triggering, and time-dependent seismic hazard, *J. Geophys. Res. 110*, B05S01, doi:10.1029/2005JB003692.

Steketee, J. A. (1958). Some geophysical applications of the elasticity theory of dislocations. *Can. J. Phys. 36* 1168–1197.

Tinti, E., E. Fukuyama, A. Piatanesi, & M. Cocco (2005a). A kinematic source-time function compatible with earthquake dynamics, *Bull. Seism. Soc. Am. 95*, 1211–1223, doi: 10.1785/0120040177.

Tinti, E., P. Spudich, & M. Cocco (2005b). Earthquake fracture energy inferred from kinematic rupture models on extended faults, *J. Geophys. Res. 110*, B12303, doi:10.1029/2005JB003644.

Vvedenskaya, A. V. (1956). Determination of displacement fields for earthquakes by means of the dislocation theory, *Izv. Akad. Nauk SSSR, Ser. Geofiz. 3*, 277–284.

Volterra, V. (1907). Sur léquilibre des corps élastiques multiplement connexes, *Ann. Éc. Norm. 3, 24*, 401-517.

Zeng, Y., J. G. Anderson & G. Yu (1994). A composite source model for computing realistic synthetic strong ground motions, *Geophys. Res. Lett. 21*, 725-728.

Zhang, W., T. Iwata, K. Irikura, H. Sekiguchi & M. Bouchon (2003). Heterogeneous distribution of the dynamic source parameters of the 1999 Chi-Chi, Taiwan, earthquake, *J. Geophys. Res. 108*, 2232, doi:10.1029/2002JB001889.

Zollo, A., A. Bobbio, A. Emolo, A. Herrero & G. De Natale (1997). Modeling of ground acceleration in the near source range: the case of 1976, Friuli earthquake (M=6.5), northern Italy, *J. Seismology 1*, 305-319.